

# Super-resolution Algorithms for Target Localization using Multiple FMCW MIMOs

Jiadi Zhang

Delft University of Technology



# Super-resolution Algorithms for Target Localization using Multiple FMCW MIMOs

by

Jiadi Zhang

to obtain the degree of Master of Science  
at the Delft University of Technology,  
to be defended publicly on Thursday August 29, 2019 at 10:00 AM.

Student number: 4739191  
Project duration: January 24, 2019 – August 29, 2019  
Thesis committee: Prof. dr. Alexander Yarovoy, TU Delft, supervisor  
Dr. ir. Bert-Jan Kooij, TU Delft  
Dr. ir. Paco Lopez Dekker, TU Delft  
Dr. Jianping Wang, TU Delft, daily supervisor

An electronic version of this thesis is available at <http://repository.tudelft.nl/>.





# Abstract

In this thesis, the joint DOA-range estimation of stationary targets is investigated using multiple FMCW MIMOs with super-resolution capability. To address the low azimuth resolution problem of single MIMO, a novel topology of array is used, which consists of multiple MIMOs arranged along the azimuth to increase azimuth resolution by extending the effective aperture size. According to such topology, signal models are formulated using FMCW waveform. To accurately model the scenarios, targets are considered as near-field objects for the system, but they are treated as far-field targets for each MIMO.

After formulating signal models, two algorithms are investigated and tested to localize targets in the observing domain. The generalized 2D-MUSIC algorithm is applicable for both multi-static and mono-static configurations of the system. The FBSS technique is used to tackle highly correlated signals. Though this algorithm provides super-high resolutions, it requires prior knowledge of the number of targets (model order). The performance would drop significantly by incorrect estimation of model order. To avoid this limitation, an augmented Lagrangian method is introduced for the first time to address the localization problem, which is named extended C-SALSA. This method casts target localization problem as a sparse representation problem, and then the problem is transferred from estimating targets' locations to the problem of sparse spectrum estimation. It utilizes variable splitting and augmented Lagrangian to handle objective functions. For both algorithms, with the accurate positions of sensors in the system, geometrical constraints of the system can be maintained by applying the same search grid to all virtual arrays, consequently, data association is avoided.

The feasibility of both proposed methods are analyzed with numerical simulations of point targets and electromagnetic simulations of an extended target. MATLAB simulation results demonstrate that the azimuth resolution is increased using multiple MIMOs with both proposed algorithms. Besides the resolution, the accuracy of the generalized 2D-MUSIC is also compared with the derived CRLB. Moreover, CRLB is used to analyze the potential accuracy for the estimation results of the mono-static configuration. In spite of the requirement of model order, the generalized 2D-MUSIC outperforms the extended C-SALCA for extended targets and is more robust for off-grid targets.



# Acknowledgements

Foremost, I would like to express my sincere gratitude to my supervisor, Prof. dr. Alexander Yarovoy, for all of his time, guidance, suggestions, and patience throughout the entirety of my study and thesis work within the group of Microwave Sensing, Signals and System. He cares about students and always encourages students. Without his support and encouragement, I would lose confidence in myself, and even the learning in the Netherlands would fail.

I also would like to give my deep gratitude to my daily supervisor, Dr. Jianping Wang, for providing invaluable support and guidance during the time of my thesis work. He led me to become an independent researcher and helped me a lot to improve my academic skills. His intuitive explanation and suggestions saved me many times from struggling with problems.

Moreover, I would like to thank many people within Group MS3, specifically, to Ing. Fred van der Zwan and Ph.D. student Shengzhi Xu for their generous help and valuable suggestions in my project.

I also want to express my thanks to my friends here in Delft, for their friendship and companionship. Of the many, I particularly like to thank Yajie Tang and my office-mates in Group MS3. Besides, a special thanks to my dear friend Hexiao Bai, who always supported me during my study life of bachelor and master.

Last but not the least, to my parents goes the utmost gratitude and thanks for without whom, I would have never made it this far.

*Jiadi Zhang  
Delft, August 2019*



# Contents

<b>List of Acronyms and Symbols</b>	<b>ix</b>
<b>1 Introduction</b>	<b>1</b>
1.1 Motivation and Aims . . . . .	1
1.2 Literature Review . . . . .	2
1.2.1 Algorithms for Single Coherent FMCW MIMO . . . . .	2
1.2.2 Algorithms for Multiple Passive Locally Coherent Arrays . . . . .	4
1.2.3 Sparsity-based Algorithms . . . . .	5
1.3 Contributions and Novelties . . . . .	5
1.4 Outline of the Thesis . . . . .	6
<b>2 System Model</b>	<b>7</b>
2.1 Geometrical Configuration . . . . .	7
2.2 Signal Model . . . . .	9
2.2.1 Chirp Signal . . . . .	10
2.2.2 Multi-static Configuration . . . . .	11
2.2.3 Mono-static Configuration . . . . .	13
2.3 Conclusions . . . . .	13
<b>3 Generalized 2D-MUSIC Algorithm</b>	<b>15</b>
3.1 Analysis of Multi-static Configuration . . . . .	15
3.2 Analysis of Mono-static Configuration . . . . .	19
3.3 Data Fusion . . . . .	21
3.3.1 Multi-static Configuration . . . . .	22
3.3.2 Mono-static Configuration . . . . .	23
3.3.3 Special Case: joint Multi-static and Mono-static Analysis . . . . .	24
3.4 Simulations . . . . .	25
3.4.1 Parameters . . . . .	25
3.4.2 MATLAB Simulations . . . . .	26
3.5 Conclusions . . . . .	32
<b>4 An Augmented Lagrangian Method</b>	<b>33</b>
4.1 Analysis of Signal Model . . . . .	33

4.2	Extended C-SALSA	34
4.3	Simulations	41
4.4	Conclusions	46
<b>5</b>	<b>Performance Analysis</b>	<b>47</b>
5.1	Parameters	47
5.2	MATLAB Simulations	48
5.2.1	Performance Analysis with CRLB	48
5.2.2	Possible Accuracy Analysis via CRLB	50
5.2.3	Comparing Resolutions of Proposed Algorithms	53
5.3	Electromagnetic Simulations	54
5.3.1	Point targets	54
5.3.2	Extended target	56
5.4	Conclusions	59
<b>6</b>	<b>Conclusions and Future Work</b>	<b>61</b>
6.1	Results and Novelties	61
6.2	Recommendations for Future Work	63
	<b>Appendices</b>	<b>65</b>
<b>A</b>	<b>Cramer-Rao Lower Bound for the Multi-static Configuration of the System</b>	<b>67</b>
<b>B</b>	<b>Chirp Spectrum</b>	<b>75</b>
<b>C</b>	<b>Generalized 2D-MUSIC Results of an Extended Target via EM Simulations</b>	<b>79</b>
C.1	Estimation Results of Multi-static Configuration	80
C.2	Estimation Results of Mono-static Configuration	82
	<b>Bibliography</b>	<b>83</b>

# List of Acronyms and Symbols

## Acronyms

1D	One-Dimensional
2D	Two-Dimensional
3D	Three-Dimensional
ADC	Analog-to-Digital
ADMM	Alternating Direction Method of Multipliers
AL	Augmented Lagrangian
AWGN	Additive White Gaussian Noise
C-SALSA	Constrained Split Augmented Lagrangian Algorithm
CRLB	Cramer-Rao Lower Bound
DFT	Discrete Fourier Transform
DOA	Direction of Arrival
DOD	Direction of Departure
DPD	Direct Position Determination
EM	ElectroMagnetic
ESPRIT	Estimation of Signal Parameters via Rotational Invariant Techniques
EVD	EigenValue Decomposition
FBSS	Forward-Backward Spatial Smoothing
FFT	Fast Fourier Transform
FMCW	Frequency Modulated Continuous Wave
GMUSIC	Generalized MUSIC

IGR	Iterative Grid Refinement
LFM	Linear Frequency Modulated
LOS	Light of Sight
MIMO	Multiple-Input Multiple-Output
ML	Maximum Likelihood
MUSIC	MUltiple SIGnal Classification
MVDR	Minimum Variance Distortionless Response
NLA	Non-uniform Linear Array
RADAR	RAdio Detection And Ranging
RMSE	Root Mean Square Error
SNR	Signal-to-Noise Ratio
SVD	Singular Value Decomposition
TOA	Time of Arrival
ULA	Uniform Linear Array
w-MUSIC	weighted MUSIC

**Symbols**

$\lambda$	Wavelength of the carrier center frequency
$\mu$	The rate of frequency change
$\phi_0$	Initial phase of transmit signal
$\sigma^2$	Noise variance
$\tau$	Time delay
$A_0$	Amplitude of transmit signal
$B$	Sweep bandwidth
$c$	Speed of light
$d$	Inter-element spacing of virtual ULA arrays

---

$d_s$	Inter-MIMO spacing
$d_{Rx}$	Inter-element spacing of receivers
$d_{Tx}$	Inter-element spacing of transmitters
$f_0$	Initial frequency
$f_c$	Carrier center frequency
$f_s$	Sampling frequency
$f_{b,max}$	Maximum beat frequency
$K$	The number of targets
$N$	The number of samples in fast-time dimension
$N_1$	The number of virtual arrays in multi-static configuration of the radar system
$N_2$	The number of virtual arrays in mono-static configuration of the radar system
$N_{Rx}$	The number of receivers of a single MIMO
$N_r$	The number of MIMOs
$N_{Tx}$	The number of transmitters of a single MIMO
$P$	The number of channels in each virtual array
$R_{max}$	Maximum detectable range
$T_s$	Sweep duration





# Introduction

## 1.1. Motivation and Aims

To better perceive and explore the unknown environment, attentions are increasingly paid to the sensing technology and the related signal processing. Since radar has advantages on localizing objects in adverse weather (such as rain and fog) and lighting conditions [1–3], it plays an important role in future applications.

The information of conventional radars is limited by the restricted degree of freedom. To extend the functionality of radars, the phased array is investigated to extract the direction of arrival (DOA) information using the phase differences between elements within an antenna array [4]. However, due to the limited number of elements, the DOA resolution of the phased array could not meet requirements of many applications, for instance, autonomous driving. Then multiple-input multiple-output (MIMO<sup>1</sup>) has been introduced and intensively studied over the last decades. The concept of virtual arrays is used in MIMO analysis and it can achieve the equivalent performance as the phased array using fewer elements [5]. Although the number of elements in the virtual array is increased, the DOA resolution of a single compact MIMO is still restricted by the physical aperture size. It is necessary to investigate new topologies of the array to obtain a better performance on DOA estimation in modern applications.

The DOA information is extracted from the phase differences among array elements,

---

<sup>1</sup>Throughout this thesis, the notion of MIMO represents a single compact coherent MIMO radar where transmitters and receivers are closely spaced.

while the range information is obtained from the time delay. Although there are many kinds of waveforms available, frequency modulated continuous wave (FMCW) are widely used because it has many advantages. It is simple and low cost with a portable size, and is safe from an absence of pulse radiation with high peak power [6]. In addition, dechirp processing is used to the received FMCW waveform, which considerably simplifies the realization of the processing circuits. The signal after dechirp, also called the beat frequency signal or the beat signal, contains range information of objects [7].

After pre-processing and sampling, the discrete signal model of the FMCW MIMO is represented as two-dimensional (2D) sinusoids [2] under the narrowband assumption, whose frequencies correspond to the DOA and range information. The general process of the joint DOA and range estimation is performed by 2D matched filters. However, for small aperture arrays, the DOA resolution of the conventional matched-filter or beamforming method is relatively low. Thus super-resolution algorithms are widely investigated for DOA estimation.

According to the review above, the main objectives of this thesis are to develop and test novel approaches to jointly estimate the DOAs and ranges of multiple targets with super-high resolutions. Moreover, these approaches should be applied to new topologies of multiple FMCW MIMOs flexibly.

## 1.2. Literature Review

To the best of our knowledge, target localization by jointly using multiple coherent MIMOs has not been reported yet. Hence, the state-of-the-art algorithms for target localization are summarized in two major categorizes: algorithms for a single coherent FMCW MIMO is reviewed in subsection 1.2.1; algorithms for passive locally coherent arrays is presented in subsection 1.2.2. Furthermore, sparsity-based algorithms are reviewed and introduced to target localization with multiple MIMOs for the first time in subsection 1.2.3.

### 1.2.1. Algorithms for Single Coherent FMCW MIMO

This subsection introduces several state-of-the-art algorithms for target localization by single coherent FMCW MIMO. The following subspace-based algorithms require the number of targets as prior knowledge to separate signal and noise subspaces. Every mentioned algorithm is analyzed whether it is suitable to be extended for analyzing the

received signals of a system consisting of multiple MIMOs.

A 2D-multiple signal classification (MUSIC) algorithm for simultaneously estimating DOA and range is proposed in [8–10]. MUSIC algorithm is based on analyzing the covariance matrix of received signals and the separation of signal and noise subspaces [11]. Moreover, [8–10] apply a 2D-forward-backward spatial smoothing (FBSS) technique [12] to cope with the coherent behavior of back-scattered signals. The disadvantage of this technique is that it reduces the maximum number of detectable targets along scanning dimension. Moreover, off-grid problem exists in this method. This algorithm can be extended for multiple MIMOs without requiring data association, which will be further discussed in Chapter 3.

In order to save computational cost, [7] and [13] proposed two different discrete Fourier transform (DFT)-MUSIC algorithms. [7] processes range profile by one-dimensional (1D)-DFT and then applies 1D-MUSIC to angle profile. By contrast, [13] first determines the time of arrivals (TOAs) by 1D-DFT, then it goes back to time domain, substitutes the estimated TOAs into the spatial spectrum function of 2D-MUSIC to estimate DOAs.

A 2D-estimation of signal parameters via rotational invariance techniques (ESPRIT)-based joint DOA and range estimator is proposed in [14], which exploits the dual shift invariant structure of the stacked smoothed matrix in time and space domains to achieve auto-paired estimation. Compared with 2D-MUSIC algorithm [8–10], this algorithm performs better with fewer receiving channels, while the performance is comparable with sufficient receiving channels [15].

A DFT-ESPRIT joint time of arrival (TOA)-DOA estimator is proposed in [16], which estimates TOAs by 1D-DFT and then obtains DOAs by 1D-ESPRIT. The computational burden is even lower than DFT-MUSIC algorithms because MUSIC employs spectral search. However, this method is difficult to operate in a challenging environment since only applying 1D-DFT to one channel cannot provide sufficient signal to noise ratio (SNR) to detect targets [7].

Although the DFT-MUSIC, 2D-ESPRIT, DFT-ESPRIT can efficiently estimate the targets' locations with respect to each individual arrays, the estimation results with multiple MIMOs have to be associated. This is sub-optimal from the perspective of estimation theory. Therefore, we will not investigate these methods in following contents.

### 1.2.2. Algorithms for Multiple Passive Locally Coherent Arrays

This subsection presents several state-of-the-art algorithms for 2D target localization using multiple passive locally coherent arrays. Assume that all emitters locate in the far-field of each array, which implies that the wavefronts relative to each array is plane wave [17]. Furthermore, assume that all emitters locate in the light of sight (LOS) region of each array.

Generalized MUSIC (GMUSIC) method proposed in [18] estimates source positions through synthesizing signal subspaces of all arrays in together. The number of targets is required as prior information. This method can resolve ambiguities in source localization compared with the decentralized MUSIC algorithm introduced in [17]. A weighted MUSIC (w-MUSIC) algorithm is proposed in [19] based on GMUSIC, which improves estimation performances by taking the difference among arrays into account. Since identical MIMOs are employed in this project, GMUSIC algorithm is suitable for being extended to analyze a system consisting of multiple MIMOs. Details will be discussed in Chapter 3.

The direct position determination (DPD) method is introduced in [20] for a single source, and in [21] for multiple sources whose number is known. This kind of algorithms utilize observations from all arrays together, and the cost function only depends on source positions. Initially, [20] proposed the DPD algorithm based on maximum likelihood (ML), after that [21] combined DPD with MUSIC to save computational cost. An improved DPD algorithm is introduced in [22], which achieves high resolution by combining minimum variance distortionless response (MVDR) with DPD algorithm. Moreover, DPD-MVDR method does not require knowledge of the number of transmitters. However, localization accuracy of previously mentioned DPD methods largely depends on synchronization accuracy among arrays [21] since they utilize the information of TOA. To relax the limitation of time synchronization, a new DPD algorithm is proposed in [23], where source positions are directly estimated by utilizing the cross-correlation matrix. Compared with previously mentioned DPD-based algorithms, this method is easier to estimate the number of targets, and the estimation accuracy is higher when time synchronization error exists among arrays. However, this method is not suitable for chirp signals.

### 1.2.3. Sparsity-based Algorithms

One of the major limitations of subspace-based algorithms is that the number of targets is required as prior knowledge to separate signal and noise subspaces. The performance of subspace-based algorithms could drop significantly if the number of targets is incorrectly estimated. Therefore, optimization-based algorithms are considered to avoid such problem. After analyzing the signal model, alternating direction method of multipliers (ADMM) [24] attracts our attentions. As far as we know, ADMM techniques have not been applied to estimate target locations with multiple MIMOs. Hence in this subsection, we will summarize the state-of-the-art algorithms of ADMM for DOA estimation and image processing.

The received data matrix of each MIMO can be cast as a sparse representation problem by introducing an overcomplete dictionary relative to all possible targets' locations, which is a constrained optimization procedure. [25] estimates DOA with a passive array by relaxing the constrained problem to an unconstrained one, which is commonly known as basis pursuit denoising and can be solved by ADMM with stopping criterion. Split augmented Lagrangian shrinkage algorithm (SALSA) [26, 27] is an ADMM technique proposed for image recovery. SALSA first relaxes the constrained problem into an unconstrained one, then further transfer it into a constrained one via ADMM trick. Constrained split augmented Lagrangian shrinkage algorithm (C-SALSA) [28] directly solves the constrained problem via ADMM for imaging inverse problems. In principle, the target localization with multiple MIMOs can be formulated as an optimization problem in the same framework as C-SALSA, though our problem has more constraints. Therefore, we will extend C-SALSA to estimate 2D targets' locations by jointly using multiple MIMOs in Chapter 4.

## 1.3. Contributions and Novelties

To the best of our knowledge, target localization by jointly using multiple coherent MIMOs has not been reported yet. To this end, a radar system consisting of multiple FMCW MIMOs has been designed to improve the azimuth resolution as much as possible. Then if the system is well-synchronized, received signals in the multi-static configuration<sup>2</sup> can be used to maximumly improve the azimuth resolution. Considering the difficulty of

---

<sup>2</sup>The notation of the multi-static configuration considers that every single compact MIMO can receive transmitted signals from all transmitters in the system.

achieving phase synchronization among multiple MIMOs, the mono-static configuration<sup>3</sup> is also discussed because its performance is independent with synchronization errors among different MIMOs.

The generalized 2D-MUSIC algorithm is proposed for 2D target localization using multiple MIMOs, whose framework is suitable for both multi-static and mono-static configurations. This subspace-based method requires the number of targets as prior knowledge to separate signal and noise subspaces. The 2D-MUSIC algorithm is applied to each compact MIMO locally, but geometrical constraints are maintained by using the same search grid for all virtual arrays. Hence, this method does not require data association.

Besides, an augmented Lagrangian method is proposed for the mono-static configuration of the system, where the localization problem is cast as a sparse representation problem. This method can find all targets' locations together with estimating the number of targets. However, it suffers from off-grid problems and requires moderate SNR.

In order to specify a benchmark for performance analysis, Cramer-Rao Lower Bound (CRLB) for the multi-static configuration is derived, shown in Appendix A. In addition, CRLB for the mono-static configuration can be obtained by simplifying the derivation of the multi-static configuration. Electromagnetic (EM) simulations are firstly done with step frequency signals, and then the received signals are mixed with chirp carrier signals to synthesize simulation results for FMCW MIMOs. The chirp spectrum is derived in Appendix B, which is used as the carrier signal in frequency domain.

## 1.4. Outline of the Thesis

The rest of this thesis is organized as follows. Chapter 2 introduces the FMCW radar system model for 2D target localization. Subsequently, signal models for both multi-static and mono-static configurations are analyzed. The generalized 2D-MUSIC algorithm is presented in Chapter 3 for both multi-static and mono-static configurations of the system. A sparsity-based augmented Lagrangian method named extended C-SALSA is given in Chapter 4 for the mono-static configuration of the system. Chapter 5 analyzes the possible accuracy of the estimation results of the mono-static configuration by CRLB. Moreover, the performance of proposed algorithms is analyzed via MATLAB and EM simulations. Some conclusions and recommendations for future work are presented in Chapter 6.

---

<sup>3</sup>The notation of the mono-static configuration means that each single compact MIMO in the system only receives its own transmitted signals.

# 2

## System Model

In this chapter, the geometry of the system is introduced and subsequently the signal model for both multi-static and mono-static configurations are analyzed using the FMCW waveform. As for a single compact MIMO, the far-field assumption is usually made for targets in the moderate distance. However, in our case, multiple MIMOs significantly increase the physical aperture size; thus the far-field assumption is not valid for the whole aperture formed by them. For accurate estimation of targets' positions, we keep the far-field assumption for each compact MIMO array while among them the near-field assumption is used. The rest of this chapter is organized as follows. In section 2.1, the geometrical relationship of the radar system is presented. The signal models are discussed in section 2.2 using the FMCW waveform, in which the chirp signal concerning a single antenna is derived in subsection 2.2.1 and in subsection 2.2.2, the signal model for multi-static configuration between MIMOs is given. The signal model for mono-static configuration based on a compact MIMO is analyzed in section 2.2.3. Conclusions are drawn in section 2.3.

### 2.1. Geometrical Configuration

Assume that there are  $N_r = 2M + 1$  identical coherent FMCW MIMOs in the system, where each MIMO contains  $N_{Tx}$  transmitters and  $N_{Rx}$  receivers. Within each compact MIMO array, the inter-element spacing of receivers is  $d_{Rx}$  and that of transmitters is  $d_{Tx} = N_{Rx}d_{Rx}$ ; thus the equivalent aperture size of the virtual array for one MIMO is

$(N_{Tx}N_{Rx} - 1)d_{Rx}$ . Besides, the distance between two adjacent MIMOs is  $d_s = \Delta \cdot d_{Rx}$ , where  $d_s \gg d_{Rx}$ .

The geometrical model of the radar system is illustrated in the upper part of Figure 2.1, where the smallest unit is a compact MIMO and the  $0^{th}$  MIMO is used as the reference unit of the radar system. Multiple MIMOs are arranged along azimuth to increase the azimuth resolution as much as possible. In the lower part of Figure 2.1, the geometry of a compact MIMO is shown.

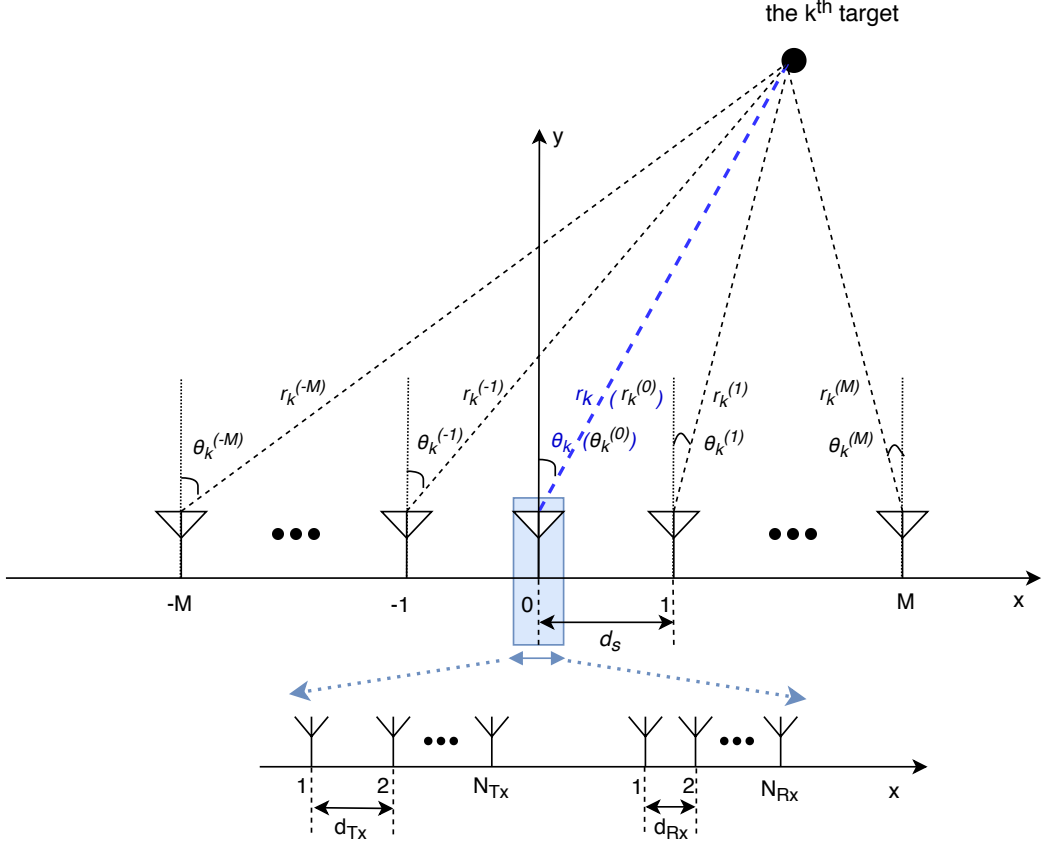


Figure 2.1: Illustration of the geometrical model of the radar system

In most case, the far-field assumption is generally made for simplicity when targets locate in the moderate distance of a compact MIMO. While in our case, since the overall aperture size of the radar system is too large to simply apply the far-field assumption, the near-field assumption is made between MIMOs to establish a more accurate model. That is to say, the wavefronts of back-scattered signals are spherical [29] from the system perspective, while they can be approximately treated as plane waves for each MIMO [30].

Assuming that  $K$  stationary point targets are located in the observing domain, they are illuminated by all MIMOs via LOS propagation. Targets' locations are parameterized

with their ranges and DOAs relative to the reference MIMO as

$$\mathbf{r} = [r_1, r_2, \dots, r_K] \quad (2.1)$$

$$\boldsymbol{\theta} = [\theta_1, \theta_2, \dots, \theta_K] \quad (2.2)$$

Then the ranges and DOAs of all targets relative to the  $m^{\text{th}}$  MIMO, can be written as

$$\mathbf{r}^{(m)} = [r_1^{(m)}, r_2^{(m)}, \dots, r_K^{(m)}] \quad (2.3)$$

$$\boldsymbol{\theta}^{(m)} = [\theta_1^{(m)}, \theta_2^{(m)}, \dots, \theta_K^{(m)}] \quad (2.4)$$

where  $m = -M, \dots, M$  and  $k = 1, \dots, K$  denote the indices of the MIMOs and indices of the targets, respectively.

According to the geometry defined above, the relative distance  $r_k^{(m)}$  between the  $k^{\text{th}}$  target and the  $m^{\text{th}}$  MIMO can be written as

$$r_k^{(m)} = \sqrt{r_k^2 + (md_s)^2 - 2r_k md_s \sin(\theta_k)} \quad (2.5)$$

and the corresponding direction of departure (DOD)  $\psi_k^{(m)}$  and DOA  $\theta_k^{(m)}$  are

$$\psi_k^{(m)} = \theta_k^{(m)} = \arcsin\left(\frac{r_k \sin(\theta_k) - md_s}{r_k^{(m)}}\right) \quad (2.6)$$

where  $\theta_k \in [-\pi/2, \pi/2]$ .

## 2.2. Signal Model

After introducing the geometry of the system, the signal model for both multi-static and mono-static configurations are analyzed using the FMCW waveform in this section. Here we assume that the transmitted signals from different transmitters are independent, and the additive noise of the receivers is also independent [31]. Besides, the relative locations of all sensors are known, and each MIMO is perfectly coherent itself. If the system is well-synchronized among MIMOs, it is possible to utilize the received signals of multi-static combinations to improve azimuth resolution. Hence, we analyze the signal model for the multi-static configuration under the assumption of phase synchronization. However, considering the difficulty of achieving phase synchronization among multiple MIMOs, signal model for the mono-static configuration is also discussed because it is unaffected by synchronization error among different MIMOs.

### 2.2.1. Chirp Signal

The transmitted signal of a FMCW MIMO is the linear frequency modulated (LFM), which is given as

$$s_{Tx}(t) = A_0 \exp \left[ j \left( 2\pi \left( f_0 - \frac{1}{2}\mu t \right) t + \phi_0 \right) \right] \quad 0 \leq t < T_s \quad (2.7)$$

where  $A_0$  is amplitude,  $f_0$  is initial frequency,  $\mu$  is the rate of frequency change,  $\mu = B/T_s$ ,  $B$  is the sweep bandwidth,  $T_s$  is sweep duration, and  $\phi_0$  is initial phase.

The back-scattered signal from a point target, at a single antenna is given by

$$\begin{aligned} x_{Rx}(t) &= \gamma e^{j\phi} \cdot s_{Tx}(t - \tau) + w(t) \\ &= \gamma e^{j\phi} \cdot A_0 \exp \left[ j \left( 2\pi \left( f_0 - \frac{1}{2}\mu(t - \tau) \right) (t - \tau) + \phi_0 \right) \right] + w(t) \end{aligned} \quad (2.8)$$

where  $\gamma e^{j\phi}$  represents reflectivity of the target,  $\tau = 2r/c$  is the roundtrip time delay caused by the distance  $r$  between the antenna and the target,  $w(t) \sim \mathcal{CN}(0, \sigma^2)$  is the complex additive white Gaussian noise (AWGN), and  $\sigma^2$  is the noise variance.

For dechirp operation, the received signal is multiplied with the complex conjugate of the transmitted signal [16]

$$\begin{aligned} x(t) &= x_{Rx}(t) \cdot s_{Tx}^*(t) \\ &= \gamma e^{j\phi} |A_0|^2 \exp \left[ j2\pi \left( \mu\tau t - f_0\tau - \frac{1}{2}\mu\tau^2 \right) \right] + w(t) \end{aligned} \quad (2.9)$$

where  $(\cdot)^*$  represents complex conjugate.

For simplicity, assume  $A_0 = 1$  in the following contents, then (2.9) can be written as

$$x(t) = \gamma e^{j\phi} \cdot \exp \left[ j2\pi \left( \mu\tau t - f_0\tau - \frac{1}{2}\mu\tau^2 \right) \right] + w(t) \quad (2.10)$$

Now, consider  $K$  stationary point targets located in the far-field of this antenna element, then the beat signal can be written as

$$x(t) = \sum_{k=1}^K \gamma_k e^{j\phi_k} \cdot \exp \left[ j2\pi \left( \mu\tau_k t - f_0\tau_k - \frac{1}{2}\mu\tau_k^2 \right) \right] + w(t) \quad (2.11)$$

where  $\tau_k = 2r_k/c$  is the roundtrip time delay caused by the distance  $r_k$  between the  $k^{th}$

target and the antenna.

Sampling the time signal in (2.11) with analog-to-digital (ADC) sampling frequency  $f_s$ , we will have the discrete received signal in a single sweep duration as

$$x[n] = \sum_{k=1}^K \gamma_k e^{j\phi_k} \cdot \exp \left[ j2\pi \left( \mu\tau_k \frac{n}{f_s} - f_0\tau_k - \frac{1}{2}\mu\tau_k^2 \right) \right] + w[n] \quad (2.12)$$

where  $n = 0, \dots, N - 1$ , and  $N = \lfloor T_s \cdot f_s \rfloor$  is the number of samples in a sweep, where  $\lfloor \cdot \rfloor$  represents the floor function.

*Note:* The value of ADC sampling rate  $f_s$  should be at least twice of maximum beat frequency  $f_{b,max}$ :

$$f_s \geq 2f_{b,max} \quad (2.13)$$

where  $f_{b,max}$  corresponds to the maximum detectable range  $R_{max}$ ,

$$f_{b,max} = \frac{2R_{max}B}{cT_s} \quad (\text{for a stationary target}) \quad (2.14)$$

Considering coherent transmitters and coherent receivers, spatial sampling is applied along both transmitter- and receiver- dimension according to the MIMO configuration. The wavefronts of scattered signals can be approximately treated as plane waves for each compact MIMO since we suppose that all targets are located in the far-field of each MIMO. Therefore, we can visualize the spatial sampling behavior via phase difference relative to the reference transmitter/receiver. For each MIMO, the  $N_{Tx}^{th}$  transmitter and the  $1^{th}$  receiver (as shown in Figure 2.1) are selected as the reference transmitter/receiver, respectively. We will analyze signal models of multi-static and mono-static configurations separately because their virtual arrays have different structures.

### 2.2.2. Multi-static Configuration

To analyze the multi-static configuration, the radar system is assumed to be well-synchronized. Suppose signals are transmitted from the  $m_1^{th}$  MIMO, then the scattered signals are received by the  $m_2^{th}$  MIMO. Since both the inter-element spacing between transmitters and receivers are equidistant, under the narrowband assumption, the re-

ceived signals in a single sweep duration can be written as

$$\begin{aligned}
 x_{m_1, m_2}[aN_{Rx} + b, n] = & \sum_{k=1}^K \gamma_k e^{j\phi_k} \cdot \exp \left[ j2\pi \left( \mu \tau_k^{(m_1, m_2)} \frac{n}{f_s} - f_0 \tau_k^{(m_1, m_2)} \right. \right. \\
 & - \frac{1}{2} \mu \left( \tau_k^{(m_1, m_2)} \right)^2 + f_0 \frac{a \cdot d_{Tx} \sin(\psi_k^{(m_1)})}{c} \\
 & \left. \left. + f_0 \frac{b \cdot d_{Rx} \sin(\theta_k^{(m_2)})}{c} \right) \right] + w_{m_1, m_2}[aN_{Rx} + b, n]
 \end{aligned} \tag{2.15}$$

where  $\{m_1, m_2\} \in \{-M, \dots, M\}$ ,  $a = -(N_{Tx} - 1), \dots, 0$ ,  $b = 0, \dots, N_{Rx} - 1$ ,  $n = 0, \dots, N - 1$ .  $\tau_k^{(m_1, m_2)} = (r_k^{(m_1)} + r_k^{(m_2)})/c$  is the time delay corresponding to the path from the  $m_1^{th}$  MIMO to the  $m_2^{th}$  MIMO through the  $k^{th}$  target.  $r_k^{(m_1)}$  and  $\psi_k^{(m_1)}$  are range and DOD of the  $k^{th}$  target to the  $m_1^{th}$  MIMO, respectively.  $r_k^{(m_2)}$  and  $\theta_k^{(m_2)}$  are range and DOA of the  $k^{th}$  target to the  $m_2^{th}$  MIMO, respectively. In total, there are  $P = N_{Tx}N_{Rx}$  channels in the virtual array.

The narrowband assumption implies that the complex envelope of a received signal does not vary significantly over the time interval that its wavefront propagates across any of the receive array [17].

In the perspective of each MIMO, we can assume that the DOD is proximately the same as the DOA for each target since all targets located in the far-field region [4]. Parameterizing the location of the  $k^{th}$  target as  $(r_k, \theta_k)$  with respect to the reference MIMO of the system, then its relative position to the  $m_1^{th}$  and  $m_2^{th}$  MIMO can be obtained via (2.5) and (2.6),

$$r_k^{(m_1)} = \sqrt{r_k^2 + (m_1 d_s)^2 - 2r_k m_1 d_s \sin(\theta_k)} \tag{2.16}$$

$$\psi_k^{(m_1)} = \theta_k^{(m_1)} = \arcsin \left( \frac{r_k \sin(\theta_k) - m_1 d_s}{r_k^{(m_1)}} \right) \tag{2.17}$$

$$r_k^{(m_2)} = \sqrt{r_k^2 + (m_2 d_s)^2 - 2r_k m_2 d_s \sin(\theta_k)} \tag{2.18}$$

$$\psi_k^{(m_2)} = \theta_k^{(m_2)} = \arcsin \left( \frac{r_k \sin(\theta_k) - m_2 d_s}{r_k^{(m_2)}} \right) \tag{2.19}$$

where the range and DOD/DOA are approximately calculated relative to the middle point between the  $N_{Tx}^{th}$  transmitter and the  $1^{th}$  receiver of each MIMO, as shown in Figure 2.1.

### 2.2.3. Mono-static Configuration

The mono-static configuration only considers that the received signals are transmitted from the same MIMO, which means  $m_1 = m_2 = m$  in (2.15). Therefore, the signal model for the mono-static configuration can be reduced from that of the multi-static configuration. Regardless of whether the system has phase synchronization error or not, we can obtain reliable targets' locations by analyzing the mono-static configuration. The virtual antenna array of each MIMO is a uniform linear array (ULA) with  $P = N_{Tx}N_{Rx}$  elements, and the spacing between two adjacent elements is  $d = d_{Rx}$  [5]. Hence the time delay varies linearly for consecutive elements in the virtual ULA [32]. Besides, we assume that  $P = 2Q + 2$ , which means at least one of  $N_{Tx}$  or  $N_{Rx}$  is even. Figure 2.2 shows the virtual ULA geometry of each MIMO, where the  $0^{th}$  antenna is the reference antenna.

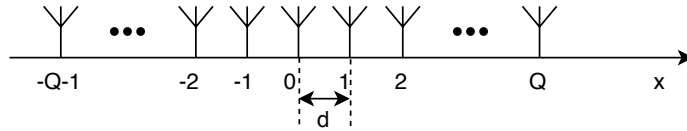


Figure 2.2: Virtual ULA geometry of each MIMO

From (2.15), the received signals of the  $m^{th}$  MIMO, in a single sweep duration, can be represented as

$$x_m[q, n] = \sum_{k=1}^K \gamma_k e^{j\phi_k} \exp \left[ j2\pi \left( \mu \tau_k^{(m)} \frac{n}{f_s} - f_0 \tau_k^{(m)} - \frac{1}{2} \mu \left( \tau_k^{(m)} \right)^2 + f_0 \frac{qd \sin(\theta_k^{(m)})}{c} \right) \right] + w_m[q, n] \quad (2.20)$$

where  $q = -Q - 1, \dots, 0, \dots, Q$ , and  $\tau_k^{(m)} = 2r_k^{(m)}/c$  represents the roundtrip time delay caused by the distance  $r_k^{(m)}$  between the  $m^{th}$  MIMO and the  $k^{th}$  target. Parameterizing the location of the  $k^{th}$  target as  $(r_k, \theta_k)$  relative to the reference MIMO, then  $(r_k^{(m)}, \theta_k^{(m)})$  can be obtained from  $(r_k, \theta_k)$  through (2.5) and (2.6).

## 2.3. Conclusions

In this chapter, the radar system model and signal models with multiple MIMOs are presented. Targets' positions are parameterized relative to the reference MIMO of the system, and then the relative positions to each MIMO can be obtained from the geo-

metrical relationship. Under the assumption that the system is well-synchronized, the signal model for the multi-static configuration is developed. After that, the signal model for the mono-static configuration is obtained by simplifying that of the multi-static configuration, which can provide robust estimation without phase synchronization among MIMOs.

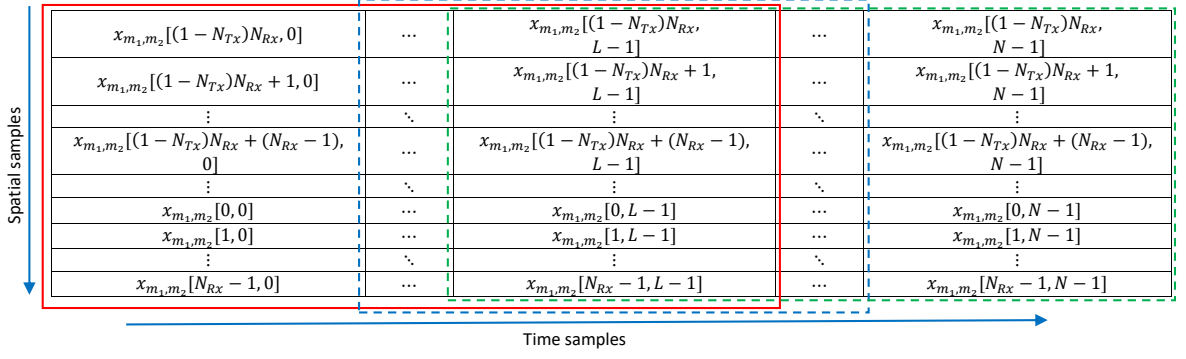
# 3

## Generalized 2D-MUSIC Algorithm

This chapter introduces the generalized 2D-MUSIC algorithm for 2D target localization, which can be applied in both multi-static and mono-static configurations of the system. This approach jointly constructs the noise subspace and steering vectors based on the geometrical relations among different small MIMO arrays. However, the number of targets is required as prior knowledge. When received signals are highly correlated or coherent, the rank of signal subspace will not equal to the number of targets. Therefore, the forward-backward spatial smoothing (FBSS) technique [12] is employed to restore the rank of the signal covariance matrix [33]. Section 3.1 analyzes the multi-static configuration based on a pair of MIMOs. The analysis of mono-static configuration based on a single MIMO is provided in Section 3.2. Then Section 3.3 discusses data fusion for these two configurations followed by a special case which combines the analysis of both multi-static and mono-static configurations into together. Section 3.4 analyzes this estimator via MATLAB simulations. Section 3.5 concludes this chapter.

### 3.1. Analysis of Multi-static Configuration

Figure 3.1 displays the measured samples of the  $m_2^{\text{th}}$  MIMO in a data matrix  $\mathbf{X}_{m_1, m_2} \in \mathbb{C}^{P \times N}$ , where signals are transmitted from the  $m_1^{\text{th}}$  MIMO. Since the virtual array of most MIMO pairs is non-uniform linear array (NLA) in the multi-static configuration, we only apply 1D-FBSS technique along the time dimension. Define a window of dimensions  $[P \times L]$ , where  $K < L < N$ , and then we have  $p = N - L + 1$  scanning positions in total.

Figure 3.1: Data matrix  $\mathbf{X}_{m_1, m_2}$  with scanning window

For each scanning position  $\tilde{p}$ , the sub-matrix  $\mathbf{D}_{m_1, m_2} \in \mathbb{C}^{P \times L}$  is

$$\mathbf{D}_{m_1, m_2}(\tilde{p}) = [\mathbf{x}_{m_1, m_2}(\tilde{p}), \mathbf{x}_{m_1, m_2}(\tilde{p} + 1), \dots, \mathbf{x}_{m_1, m_2}(\tilde{p} + L - 1)] \quad (3.1)$$

where  $\tilde{p} = 0, 1, \dots, N - L$  and

$$\mathbf{x}_{m_1, m_2}(\tilde{p}) = \begin{bmatrix} x_{m_1, m_2}((1 - N_{Tx})N_{Rx}, \tilde{p}) \\ \vdots \\ x_{m_1, m_2}(aN_{Rx} + b, \tilde{p}) \\ \vdots \\ x_{m_1, m_2}(N_{Rx} - 1, \tilde{p}) \end{bmatrix} \in \mathbb{C}^{P \times 1} \quad (3.2)$$

Each sub-matrix is stacked into a  $[PL \times 1]$  vector column by column, as

$$\begin{aligned} \mathbf{d}_{m_1, m_2}(\tilde{p}) &= \text{vec}(\mathbf{D}_{m_1, m_2}(\tilde{p})) \\ &= [\mathbf{x}_{m_1, m_2}(\tilde{p}); \mathbf{x}_{m_1, m_2}(\tilde{p} + 1); \dots; \mathbf{x}_{m_1, m_2}(\tilde{p} + L - 1)] \end{aligned} \quad (3.3)$$

and then collected into a new data matrix  $\tilde{\mathbf{D}}_{m_1, m_2}(\tilde{p}) \in \mathbb{C}^{PL \times p}$ .

The smoothed covariance matrix  $\mathbf{R}_{m_1, m_2} \in \mathbb{C}^{PL \times PL}$  can be obtained as [8]

$$\begin{aligned} \mathbf{R}_{m_1, m_2} &= \frac{1}{2p} \left[ \tilde{\mathbf{D}}_{m_1, m_2} \tilde{\mathbf{D}}_{m_1, m_2}^H + \mathbf{J} \left( \tilde{\mathbf{D}}_{m_1, m_2} \tilde{\mathbf{D}}_{m_1, m_2}^H \right)^* \mathbf{J} \right] \\ &= \mathbf{A}_s^{(m_1, m_2)} \mathbf{R}_s^{(m_1, m_2)} (\mathbf{A}_s^{(m_1, m_2)})^H + \sigma^2 \mathbf{I} \end{aligned} \quad (3.4)$$

where  $\mathbf{J} \in \mathbb{C}^{PL \times PL}$  is a reflection matrix,

$$\mathbf{J} = \begin{bmatrix} 0 & 0 & \cdots & 1 \\ \vdots & 0 & 1 & 0 \\ 0 & \ddots & 0 & \vdots \\ 1 & 0 & \cdots & 0 \end{bmatrix} \quad (3.5)$$

$\mathbf{R}_s^{(m_1, m_2)} \in \mathbb{C}^{K \times K}$  is the covariance matrix of received signals (excluding noise), and columns of  $\mathbf{A}_s^{(m_1, m_2)} \in \mathbb{C}^{PL \times K}$  contain steering vectors of all targets,

$$\mathbf{A}_s^{(m_1, m_2)} = [\mathbf{a}_{m_1, m_2}(r_1, \theta_1), \dots, \mathbf{a}_{m_1, m_2}(r_K, \theta_K)] \quad (3.6)$$

When signals are transmitted from the  $m_1^{th}$  MIMO and then the scattered signals are received by the  $m_2^{th}$  MIMO, steering vector  $\mathbf{a}_{m_1, m_2} \in \mathbb{C}^{PL \times 1}$  of the  $k^{th}$  target can be expressed as [13, 34]

$$\mathbf{a}_{m_1, m_2}(r_k, \theta_k) = \mathbf{a}_{m_1, m_2}^{(\tau)}(\tau_k^{(m_1, m_2)}) \otimes [\mathbf{a}_{m_1, m_2}^{(\psi)}(\psi_k^{(m_1)}) \otimes \mathbf{a}_{m_1, m_2}^{(\theta)}(\theta_k^{(m_2)})] \quad (3.7)$$

where  $\otimes$  represents the Kronecker product.  $(r_k, \theta_k)$  represents the location of the  $k^{th}$  target to the reference MIMO.  $\mathbf{a}_{m_1, m_2}^{(\tau)} \in \mathbb{C}^{L \times 1}$ ,  $\mathbf{a}_{m_1, m_2}^{(\psi)} \in \mathbb{C}^{N_{Tx} \times 1}$  and  $\mathbf{a}_{m_1, m_2}^{(\theta)} \in \mathbb{C}^{N_{Rx} \times 1}$  are steering vectors of the time delay, DOD, and DOA for the  $k^{th}$  target to the  $m_1^{th}$  and  $m_2^{th}$  MIMO pair, respectively.  $\tau_k^{(m_1, m_2)} = (r_k^{(m_1)} + r_k^{(m_2)})/c$  is the time delay corresponding to the path from the  $m_1^{th}$  MIMO to the  $k^{th}$  target and then to the  $m_2^{th}$  MIMO.  $r_k^{(m_1)}$  and  $\psi_k^{(m_1)}$  are the range and DOD of the  $k^{th}$  target to the  $m_1^{th}$  MIMO, respectively.  $r_k^{(m_2)}$  and  $\theta_k^{(m_2)}$  are the range and DOA of the  $k^{th}$  target to the  $m_2^{th}$  MIMO, respectively. Moreover,  $(r_k^{(m_1)}, \psi_k^{(m_1)})$  and  $(r_k^{(m_2)}, \theta_k^{(m_2)})$  can be obtained from  $(r_k, \theta_k)$  through (2.16) - (2.19).

From the signal model in (2.15), we can write the time delay, DOD, and DOA steering vectors ( $\mathbf{a}_{m_1, m_2}^{(\tau)}$ ,  $\mathbf{a}_{m_1, m_2}^{(\psi)}$  and  $\mathbf{a}_{m_1, m_2}^{(\theta)}$ ) in (3.7) as

$$\mathbf{a}_{m_1, m_2}^{(\tau)}(\tau_k^{(m_1, m_2)}) = \left[ 1, \dots, \exp\left(j2\pi\mu\tau_k^{(m_1, m_2)}\frac{L-1}{f_s}\right) \right]^T \quad (3.8)$$

$$\mathbf{a}_{m_1, m_2}^{(\psi)}(\psi_k^{(m_1)}) = \left[ \exp\left(j2\pi f_0 \frac{-(N_{Tx}-1)d_{Tx} \sin(\psi_k^{(m_1)})}{c}\right), \dots, 1 \right]^T \quad (3.9)$$

$$\mathbf{a}_{m_1, m_2}^{(\theta)}(\theta_k^{(m_2)}) = \left[ 1, \dots, \exp\left(j2\pi f_0 \frac{(N_{Rx}-1)d_{Rx} \sin(\theta_k^{(m_2)})}{c}\right) \right]^T \quad (3.10)$$

Taking eigenvalue decomposition (EVD) or singular value decomposition (SVD) to the

smoothed covariance matrix  $\mathbf{R}_{m_1, m_2}$ , we have

$$\mathbf{R}_{m_1, m_2} = \mathbf{U}_s^{(m_1, m_2)} \boldsymbol{\Sigma}_s^{(m_1, m_2)} (\mathbf{U}_s^{(m_1, m_2)})^H + \mathbf{U}_n^{(m_1, m_2)} \boldsymbol{\Sigma}_n^{(m_1, m_2)} (\mathbf{U}_n^{(m_1, m_2)})^H \quad (3.11)$$

where  $\mathbf{U}_s^{(m_1, m_2)} \in \mathbb{C}^{PL \times K}$  is the signal subspace which relates to eigenvectors of the  $K$  largest eigenvalues  $\boldsymbol{\Sigma}_s^{(m_1, m_2)} \in \mathbb{C}^{K \times K}$ , and  $\mathbf{U}_n^{(m_1, m_2)} \in \mathbb{C}^{PL \times (PL-K)}$  represents the noise subspace which contains eigenvectors of the  $(PL - K)$  smallest eigenvalues  $\boldsymbol{\Sigma}_n^{(m_1, m_2)} \in \mathbb{C}^{(PL-K) \times (PL-K)}$  [10].

The columns of  $\mathbf{A}_s^{(m_1, m_2)}$  in (3.4) span the same space as the columns of signal subspace  $\mathbf{U}_s^{(m_1, m_2)}$  in (3.11). Ideally, we have

$$\mathbf{a}_{m_1, m_2}^H(r_k, \theta_k) \mathbf{U}_n^{(m_1, m_2)} = \mathbf{0} \quad (3.12)$$

where  $k = 1, \dots, K$ .

However, due to the existence of noise,  $\mathbf{a}_{m_1, m_2}(r_k, \theta_k)$  and  $\mathbf{U}_n^{(m_1, m_2)}$  are not perfectly orthogonal. That is to say, (3.12) does not hold. Therefore, targets' locations are normally estimated through minimizing the following objective function,

$$\underset{r, \theta}{\operatorname{argmin}} \quad \mathbf{a}_{m_1, m_2}^H(r, \theta) \mathbf{U}_n^{(m_1, m_2)} (\mathbf{U}_n^{(m_1, m_2)})^H \mathbf{a}_{m_1, m_2}(r, \theta) \quad (3.13)$$

The targets' locations are parameterized with the range and bearing angle relative to the reference MIMO of the system (as shown in Figure 2.1). Therefore, we define a search grid which includes all possible targets' locations relative to the reference MIMO. Then the search grid can be transferred for each MIMO through (2.5) - (2.6). Let  $(r, \theta)$  represents a general point on the search grid. The 2D-MUSIC spatial spectrum function for a MIMO pair can be written as

$$f_{m_1, m_2}(r, \theta) = \frac{1}{\mathbf{a}_{m_1, m_2}^H(r, \theta) \mathbf{U}_n^{(m_1, m_2)} (\mathbf{U}_n^{(m_1, m_2)})^H \mathbf{a}_{m_1, m_2}(r, \theta)} \quad (3.14)$$

where  $\mathbf{a}_{m_1, m_2}(r, \theta)$  is the steering vector for a possible target location on the search grid, which is defined in (3.7).

## 3.2. Analysis of Mono-static Configuration

Since the virtual array of each MIMO is a ULA in the mono-static configuration, it is possible to apply 2D-FBSS technique along both spatial and fast-time dimensions for each ULA. To achieve a better performance, 2D-FBSS is employed in this configuration. Hence the FBSS technique for mono-static configuration is different from multi-static configuration.

Figure 3.2 displays the measured samples of the  $m^{\text{th}}$  MIMO in a data matrix  $\mathbf{X}_m \in \mathbb{C}^{P \times N}$ . We define a window of dimensions  $[l_1 \times l_2]$ , where  $K < l_1 < P$  and  $K < l_2 < N$ , and then scan the data matrix in all possible positions. We have  $p_1 = P - l_1 + 1$  scanning positions in the spatial dimension and  $p_2 = N - l_2 + 1$  scanning positions in the time dimension.

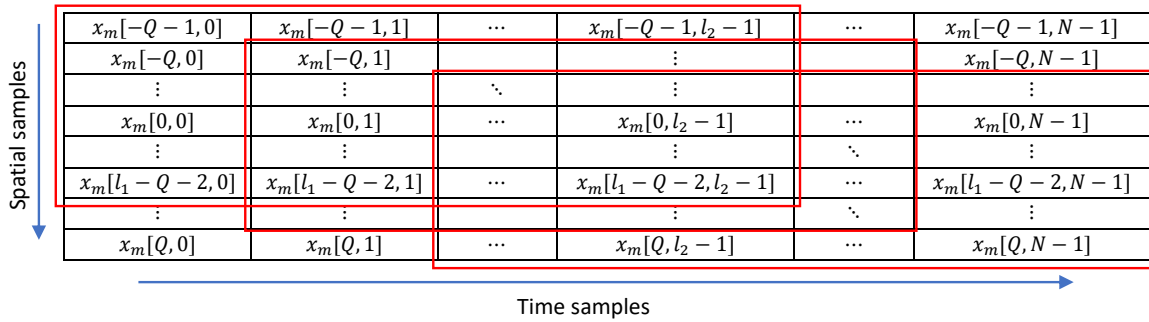


Figure 3.2: Data matrix of the  $m^{\text{th}}$  MIMO with scanning window

For each scanning position  $\tilde{\mathbf{p}} = (\tilde{p}_1, \tilde{p}_2)$ , the sub-matrix  $\mathbf{D}_m \in \mathbb{C}^{l_1 \times l_2}$  is

$$\mathbf{D}_m(\tilde{\mathbf{p}}) = [\mathbf{x}_m(\tilde{p}_2), \mathbf{x}_m(\tilde{p}_2 + 1), \dots, \mathbf{x}_m(\tilde{p}_2 + l_2 - 1)] \quad (3.15)$$

where  $\tilde{p}_1 = 0, 1, \dots, P - l_1$ ,  $\tilde{p}_2 = 0, 1, \dots, N - l_2$  and

$$\mathbf{x}_m(\tilde{p}_2) = \begin{bmatrix} x_m(\tilde{p}_1 - Q - 1, \tilde{p}_2) \\ \vdots \\ x_m(\tilde{p}_1, \tilde{p}_2) \\ \vdots \\ x_m(\tilde{p}_1 + l_1 - Q - 2, \tilde{p}_2) \end{bmatrix} \in \mathbb{C}^{l_1 \times 1} \quad (3.16)$$

Each sub-matrix is stacked into a  $[l_1 l_2 \times 1]$  vector column by column, as

$$\begin{aligned} \mathbf{d}_m(\tilde{\mathbf{p}}) &= \text{vec}(\mathbf{D}_m(\tilde{\mathbf{p}})) \\ &= [\mathbf{x}_m(\tilde{p}_2); \mathbf{x}_m(\tilde{p}_2 + 1); \dots; \mathbf{x}_m(\tilde{p}_2 + l_2 - 1)] \end{aligned} \quad (3.17)$$

and then collected into a new data matrix  $\tilde{\mathbf{D}}_m \in \mathbb{C}^{l_1 l_2 \times p_1 p_2}$ .

The smoothed covariance matrix  $\mathbf{R}_m \in \mathbb{C}^{l_1 l_2 \times l_1 l_2}$  is obtained as [8]

$$\begin{aligned} \mathbf{R}_m &= \frac{1}{2p_1 p_2} \left[ \tilde{\mathbf{D}}_m \tilde{\mathbf{D}}_m^H + \mathbf{J}(\tilde{\mathbf{D}}_m \tilde{\mathbf{D}}_m^H)^* \mathbf{J} \right] \\ &= \mathbf{A}_s^{(m)} \mathbf{R}_s^{(m)} (\mathbf{A}_s^{(m)})^H + \sigma^2 \mathbf{I} \end{aligned} \quad (3.18)$$

where  $\mathbf{J} \in \mathbb{C}^{l_1 l_2 \times l_1 l_2}$  is a reflection matrix

$$\mathbf{J} = \begin{bmatrix} 0 & 0 & \dots & 1 \\ \vdots & 0 & 1 & 0 \\ 0 & \dots & 0 & \vdots \\ 1 & 0 & \dots & 0 \end{bmatrix} \quad (3.19)$$

$\mathbf{R}_s^{(m)} \in \mathbb{C}^{K \times K}$  is the covariance matrix of received signals (excluding noise), and columns of  $\mathbf{A}_s^{(m)} \in \mathbb{C}^{l_1 l_2 \times K}$  contain steering vectors of all targets,

$$\mathbf{A}_s^{(m)} = [\mathbf{a}_m(r_1, \theta_1), \dots, \mathbf{a}_m(r_K, \theta_K)] \quad (3.20)$$

The steering vector of the  $k^{\text{th}}$  target relative to the  $m^{\text{th}}$  MIMO can be expressed as

$$\mathbf{a}_m(r_k, \theta_k) = \mathbf{a}_m^{(r)}(r_k^{(m)}) \otimes \mathbf{a}_m^{(\theta)}(\theta_k^{(m)}) \quad (3.21)$$

where  $(r_k, \theta_k)$  represents the location of the  $k^{\text{th}}$  target relative to the reference MIMO.  $\mathbf{a}_m^{(r)} \in \mathbb{C}^{l_2 \times 1}$  and  $\mathbf{a}_m^{(\theta)} \in \mathbb{C}^{l_1 \times 1}$  are steering vectors of the range  $(r_k^{(m)})$  and DOA  $(\theta_k^{(m)})$  for the  $k^{\text{th}}$  target relative to the  $m^{\text{th}}$  MIMO, respectively. Moreover,  $(r_k^{(m)}, \theta_k^{(m)})$  can be obtained from  $(r_k, \theta_k)$  through (2.5) and (2.6).

From the signal model in (2.20), we can write the range and DOA steering vectors ( $\mathbf{a}_m^{(r)}$  and  $\mathbf{a}_m^{(\theta)}$ ) in (3.21) as

$$\mathbf{a}_m^{(r)}(r_k^{(m)}) = \left[ 1, \dots, \exp \left( j 2\pi \mu \frac{2r_k^{(m)} l_2 - 1}{c} \frac{1}{f_s} \right) \right]^T \quad (3.22)$$

$$\mathbf{a}_m^{(\theta)}(\theta_k^{(m)}) = \left[ \exp \left( j2\pi f_0 \frac{(-Q-1)d \sin(\theta_k^{(m)})}{c} \right), \right. \\ \left. \dots, \exp \left( j2\pi f_0 \frac{(l_1-Q-2)d \sin(\theta_k^{(m)})}{c} \right) \right]^T \quad (3.23)$$

Applying EVD/SVD to the smoothed covariance matrix  $\mathbf{R}_m$ , one can get

$$\mathbf{R}_m = \mathbf{U}_s^{(m)} \mathbf{\Sigma}_s^{(m)} (\mathbf{U}_s^{(m)})^H + \mathbf{U}_n^{(m)} \mathbf{\Sigma}_n^{(m)} (\mathbf{U}_n^{(m)})^H \quad (3.24)$$

where  $\mathbf{U}_s^{(m)} \in \mathbb{C}^{l_1 l_2 \times K}$  is the signal subspace that contains eigenvectors of the  $K$  largest eigenvalues  $\mathbf{\Sigma}_s^{(m)} \in \mathbb{C}^{K \times K}$ , and  $\mathbf{U}_n^{(m)} \in \mathbb{C}^{l_1 l_2 \times (l_1 l_2 - K)}$  is the noise subspace which includes eigenvectors of the  $(l_1 l_2 - K)$  smallest eigenvalues  $\mathbf{\Sigma}_n^{(m)} \in \mathbb{C}^{(l_1 l_2 - K) \times (l_1 l_2 - K)}$ .

As described in Section 3.1, the columns of  $A_s^{(m)}$  in (3.18) span the same space as the columns of signal subspace  $\mathbf{U}_s^{(m)}$  in (3.24). However,  $\mathbf{A}_s^{(m)}$  and  $\mathbf{U}_n^{(m)}$  are not perfectly orthogonal to each other due to the influence of noise. Thus, targets' positions are generally estimated by minimizing the following objective function,

$$\underset{r, \theta}{\operatorname{argmin}} \quad \mathbf{a}_m^H(r, \theta) \mathbf{U}_n^{(m)} (\mathbf{U}_n^{(m)})^H \mathbf{a}_m(r, \theta) \quad (3.25)$$

The targets' positions are parameterized with range and bearing information relative to the reference MIMO. Accordingly, we define a search grid which includes all possible targets' locations with respect to the reference MIMO. Then the search grid can be transferred for each MIMO through (2.5) - (2.6). As a result, the 2D-MUSIC joint range-DOA spatial spectrum function for the  $m^{\text{th}}$  MIMO is

$$f_m(r, \theta) = \frac{1}{\mathbf{a}_m^H(r, \theta) \mathbf{U}_n^{(m)} (\mathbf{U}_n^{(m)})^H \mathbf{a}_m(r, \theta)} \quad (3.26)$$

where  $\mathbf{a}_m(r, \theta)$  is the steering vector for a possible target position to the  $m^{\text{th}}$  MIMO, which is defined in (3.21).

### 3.3. Data Fusion

Since the system contains  $N_r$  identical MIMOs, we totally have  $N_1 = N_r^2$  virtual arrays in the multi-static configuration and  $N_2 = N_r$  virtual ULAs in the mono-static configuration. For each configuration, we have to integrate estimation results of all virtual arrays to obtain the final result. The same search grid is applied to all virtual arrays to maintain geometrical constraints, which includes all potential targets' positions param-

eterized with the range and DOA  $(r, \theta)$  relative to the reference MIMO. Then the search grid can be transferred for each MIMO via (2.5) - (2.6).

Virtual arrays in the system do not share measured data samples with one another, which means every virtual array can do estimation individually. Nevertheless, our main objectives are to improve azimuth resolution and get robust estimation result by jointly using multiple MIMOs. We prefer to coherently integrate all virtual arrays during the search stage instead of fusing individual estimation results. We combine steering vector and noise subspace of all virtual arrays into together, but the steering vector of each virtual array only interacts with its own noise subspace [18]. Section 3.3.1 and 3.3.2 offer data fusion for multi-static and mono-static configurations respectively. Besides, Section 3.3.3 describes a special case: targets' locations are estimated through combining the analysis of multi-static and mono-static configurations together when they share the same bearing reference center of each MIMO.

### 3.3.1. Multi-static Configuration

The generalized 2D-MUSIC spatial spectrum function, for intergrating all virtual arrays in multi-static configuration, can be written as:

$$f_{multi}(r, \theta) = \frac{1}{\mathbf{a}_{multi}^H(r, \theta) \mathbf{U}_n^{(multi)} (\mathbf{U}_n^{(multi)})^H \mathbf{a}_{multi}(r, \theta)} \quad (3.27)$$

where  $N_1$  is the number of virtual arrays in multi-static configuration, and  $\mathbf{a}_{multi}(r, \theta) \in \mathbb{C}^{N_1 PL \times 1}$  and  $\mathbf{U}_n^{(multi)} \in \mathbb{C}^{N_1 PL \times N_1 (PL - K)}$  are joint steering vector and noise subspace of the system, respectively.

The joint steering vector  $\mathbf{a}_{multi}(r, \theta)$  can be expressed as:

$$\mathbf{a}_{multi}(r, \theta) = [\mathbf{a}_{-M, -M}(r, \theta); \dots; \mathbf{a}_{m_1, m_2}(r, \theta); \dots; \mathbf{a}_{M, M}(r, \theta)] \quad (3.28)$$

The joint noise subspace  $\mathbf{U}_n^{(multi)}$  is constructed as:

$$\mathbf{U}_n^{(multi)} = \begin{bmatrix} \mathbf{U}_n^{(-M, -M)} & \mathbf{0} & \dots & \dots & \mathbf{0} \\ \mathbf{0} & \ddots & \ddots & & \vdots \\ \vdots & \mathbf{0} & \mathbf{U}_n^{(m_1, m_2)} & \mathbf{0} & \vdots \\ \vdots & & \ddots & \ddots & \mathbf{0} \\ \mathbf{0} & \dots & \dots & \mathbf{0} & \mathbf{U}_n^{(M, M)} \end{bmatrix} \quad (3.29)$$

where  $\{m_1, m_2\} \in \{-M, \dots, M\}$ .

Simplifying (3.27), one can obtain

$$\begin{aligned} f_{multi}(r, \theta) &= \left( \sum_{m_1=-M}^M \sum_{m_2=-M}^M \mathbf{a}_{m_1, m_2}^H(r, \theta) \mathbf{U}_n^{(m_1, m_2)} (\mathbf{U}_n^{(m_1, m_2)})^H \mathbf{a}_{m_1, m_2}(r, \theta) \right)^{-1} \\ &= \left( \sum_{m_1=-M}^M \sum_{m_2=-M}^M f_{m_1, m_2}^{-1}(r, \theta) \right)^{-1} \end{aligned} \quad (3.30)$$

where  $f_{m_1, m_2}(r, \theta)$  is defined in (3.14).

### 3.3.2. Mono-static Configuration

The generalized 2D-MUSIC spatial spectrum function for integrating all virtual arrays in mono-static configuration has the same framework as the multi-static case, which can be written as

$$f_{mono}(r, \theta) = \frac{1}{\mathbf{a}_{mono}^H(r, \theta) \mathbf{U}_n^{(mono)} (\mathbf{U}_n^{(mono)})^H \mathbf{a}_{mono}(r, \theta)} \quad (3.31)$$

where  $N_2$  is the number of virtual arrays in mono-static configuration, and  $\mathbf{a}_{mono}(r, \theta) \in \mathbb{C}^{N_2 l_1 l_2 \times 1}$  and  $\mathbf{U}_n^{(mono)} \in \mathbb{C}^{N_2 l_1 l_2 \times N_2 (l_1 l_2 - K)}$  are joint steering vector and noise subspace of the system, respectively.

The joint steering vector  $\mathbf{a}_{mono}(r, \theta)$  can be expressed as:

$$\mathbf{a}_{mono}(r, \theta) = [\mathbf{a}_{-M}(r, \theta); \dots; \mathbf{a}_m(r, \theta); \dots; \mathbf{a}_M(r, \theta)] \quad (3.32)$$

The joint noise subspace  $\mathbf{U}_n^{(mono)}$  is constructed as:

$$\mathbf{U}_n^{(mono)} = \begin{bmatrix} \mathbf{U}_n^{(-M)} & \mathbf{0} & \dots & \dots & \mathbf{0} \\ \mathbf{0} & \ddots & \ddots & & \vdots \\ \vdots & \mathbf{0} & \mathbf{U}_n^{(m)} & \mathbf{0} & \vdots \\ \vdots & & \ddots & \ddots & \mathbf{0} \\ \mathbf{0} & \dots & \dots & \mathbf{0} & \mathbf{U}_n^{(M)} \end{bmatrix} \quad (3.33)$$

where  $m = -M, \dots, M$ .

Simplifying (3.31), one can get

$$\begin{aligned} f_{mono}(r, \theta) &= \left( \sum_{m=-M}^M \mathbf{a}_m(r, \theta)^H \mathbf{U}_n^{(m)} (\mathbf{U}_n^{(m)})^H \mathbf{a}_m(r, \theta) \right)^{-1} \\ &= \left( \sum_{m=-M}^M f_m^{-1}(r, \theta) \right)^{-1} \end{aligned} \quad (3.34)$$

where  $f_m(r, \theta)$  is defined in (3.26).

Note that when there is only a single MIMO, (3.34) is reduced to the traditional 2D-MUSIC algorithm.

### 3.3.3. Special Case: joint Multi-static and Mono-static Analysis

If the reference antenna of each virtual ULA locates at the middle point between the  $N_{Tx}^{th}$  transmitter and the  $1^{th}$  receiver, as shown in Figure 2.1, of each MIMO, the virtual ULAs and NLAs share the same bearing reference centers. Then it is possible to apply the analysis of mono-static configuration for virtual ULAs in the multi-static configuration to get better resolutions. More specifically, we will apply 2D-FBSS to virtual ULAs, but employ 1D-FBSS to virtual NLAs in the multi-static configuration. Consequently, the data fusion process can be divided into three steps:

1. Joint estimation results of all virtual NLAs.
2. Joint estimation results of all virtual ULAs.
3. Fuse these two partly fused results to obtain the final result.

In this case, the generalized 2D-MUSIC spatial spectrum function still shares the same framework as general multi-static/mono-static configuration, which can be written as

$$f_{joint}(r, \theta) = \frac{1}{\mathbf{a}_{joint}^H(r, \theta) \mathbf{U}_n^{(joint)} (\mathbf{U}_n^{(joint)})^H \mathbf{a}_{joint}(r, \theta)} \quad (3.35)$$

where

$$\mathbf{a}_{joint}(r, \theta) = [\mathbf{a}_{dual}(r, \theta); \mathbf{a}_{mono}(r, \theta)] \quad (3.36)$$

and

$$\mathbf{U}_n^{(joint)} = \begin{bmatrix} \mathbf{U}_n^{(dual)} & \mathbf{0} \\ \mathbf{0} & \mathbf{U}_n^{(mono)} \end{bmatrix} \quad (3.37)$$

$\mathbf{a}_{dual}(r, \theta)$  and  $\mathbf{U}_n^{dual}$  can be obtained from (3.28) and (3.29) with the extra condition that  $m_1 \neq m_2$ .  $\mathbf{a}_{mono}(r, \theta)$  and  $\mathbf{U}_n^{(mono)}$  can be directly got from (3.32) and (3.33).

Simplifying (3.35), one can have

$$f_{joint}(r, \theta) = \left( \sum_{m_1=-M}^M \sum_{\substack{m_2=-M \\ m_2 \neq m_1}}^M f_{m_1, m_2}^{-1}(r, \theta) + \sum_{m=-M}^M f_m^{-1}(r, \theta) \right)^{-1} \quad (3.38)$$

where  $f_{m_1, m_2}(r, \theta)$  and  $f_m(r, \theta)$  are defined in (3.14) and (3.26), respectively.

## 3.4. Simulations

### 3.4.1. Parameters

Table 3.1 lists key parameters of chirp signals for MATLAB simulations, Table 3.2 offers parameters of the radar system, and Table 3.3 contains parameters of each MIMO. We employ three identical coherent FMCW MIMOs in the system. Each MIMO has 2 transmitters and 4 receivers. The inter-element spacing of receivers is  $d_{Rx} = \lambda/2$ , and the inter-element spacing of transmitters is  $d_{Tx} = 2\lambda$ . Hence, the virtual antenna array of each MIMO is a ULA with 8 elements in the mono-static configuration, and the inter-element spacing is  $d = d_{Rx}$ .

Table 3.1: Parameters of chirp signals for MATLAB simulations

Parameter	Value
Center frequency ( $f_c$ )	76.5 GHz
Chirp valid sweep bandwidth ( $B$ )	600 MHz
Sweep duration ( $T_s$ )	60 $\mu$ s
The number of samples per chirp ( $N$ )	372
ADC sampling rate ( $f_s$ )	6.2 MHz

Table 3.2: Parameters of the radar system

Parameter	Value
$M$	1
The number of MIMOs ( $N_r = 2M + 1$ )	3
$\Delta$	256
Inter-MIMO spacing ( $d_s = \Delta \cdot d_{Rx}$ )	0.502 m

Table 3.3: Parameters of a single MIMO

Parameter	Value
The number of transmitters ( $N_{Tx}$ )	2
The number of receivers ( $N_{Rx}$ )	4
Inter-element spacing of transmitters ( $d_{Tx}$ )	0.0078 m
Inter-element spacing of receivers ( $d_{Rx}$ )	0.002 m
The number of elements per MIMO ( $P = N_{Tx}N_{Rx}$ )	8
$Q = (P - 2)/2$	3
Inter-element spacing for virtual ULAs ( $d$ )	0.002 m

### 3.4.2. MATLAB Simulations

Search steps are  $\Delta R = 0.02m$  and  $\Delta\theta = 0.02^\circ$  in range and azimuth dimensions, respectively. SNR is set to 15 dB in all simulations.

We place three point targets to analyze the performance of the generalized 2D-MUSIC algorithm, where two of them locates in the same range relative to the system while two of them locates in the same bearing direction relative to the system. Figure 3.3 displays pseudo spectrum of a single MIMO together with the mono-static and multi-static configurations of the radar system. 1D-FBSS is applied in Figure 3.3 (a), (b) and (c) along the time dimension. 2D-FBSS is employed in Figure 3.3 (d) and (e) along both time and spatial dimensions. Using parameters listed in Table 3.3, virtual NLAs and ULAs of the system share the same reference centers for calculating relative ranges and DOAs. Therefore, 2D-FBSS is used for virtual ULAs and 1D-FBSS is applied for virtual NLAs in Figure 3.3 (f). Since 1D-FBSS cannot completely achieve decorrelation of high correlated signals, bad estimation results of the multi-static configuration are discarded by checking the rank of signal subspace. In addition, the window size for 1D-FBSS and 2D-FBSS are  $[8 \times 100]$  and  $[5 \times 100]$ , respectively.

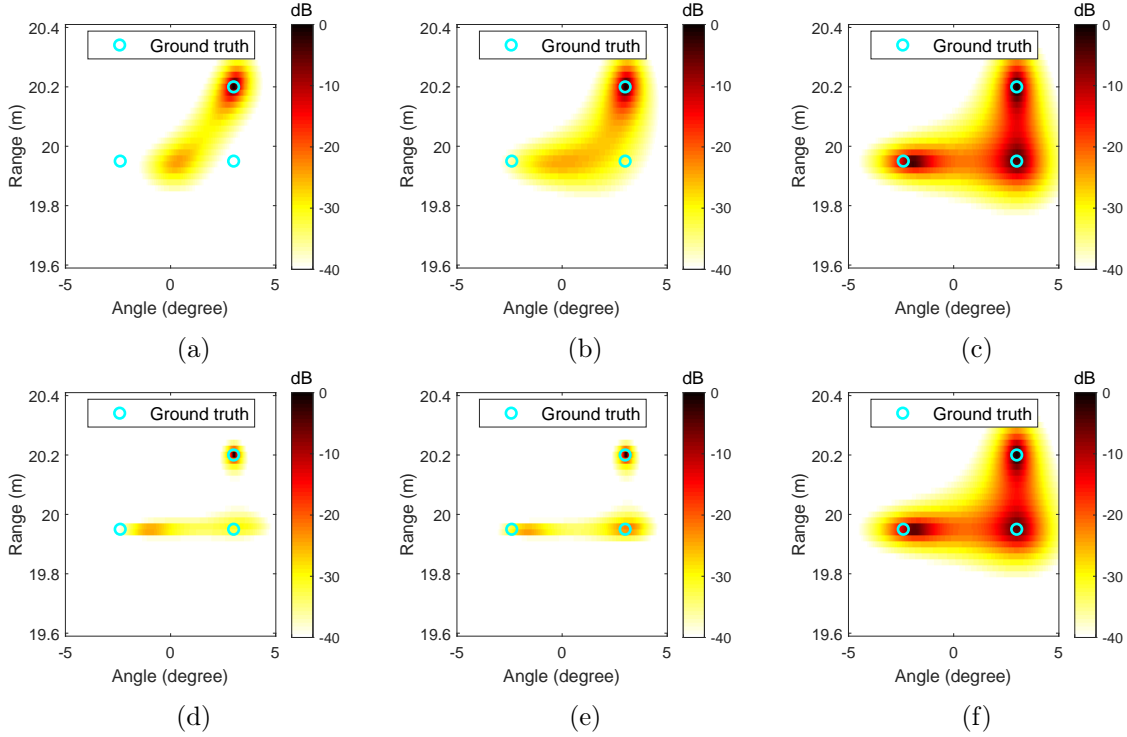


Figure 3.3: Pseudo spectrum of 3 point targets when SNR is 15dB. The first row employs 1D-FBSS: (a) a single MIMO; (b) the mono-static configuration of the radar system; (c) the multi-static configuration of the radar system. The second row uses 2D-FBSS for virtual ULAs and 1D-FBSS for virtual NLAs: (d) a single MIMO; (e) the mono-static configuration of the radar system; (f) the multi-static configuration of the radar system.

Comparing Figure 3.3 (a) with (b) and (c) can be found that azimuth ambiguity can be suppressed by jointly using multiple MIMOs, but only the multi-static configuration can achieve that with 1D-FBSS along the time dimension. Comparing Figure 3.3 (b) with (e) can be seen that apply 2D-FBSS along both time and spatial dimensions have better decorrelation performance than 1D-FBSS. Comparing Figure 3.3 (d) with (e), one can find that azimuth resolution can be improved in the mono-static configuration with 2D-FBSS. Furthermore, 2D-FBSS can improve resolutions compared with 1D-FBSS. However, the range resolution is only slightly improved in Figure 3.3 (f) compared with (c). The reason is that majority virtual arrays in the multi-static configuration are NLAs and the estimation results of all virtual arrays are jointed without weighting. Therefore, the improvement made by 2D-FBSS to virtual ULAs are suppressed.

Figure 3.4 displays the influence of the scanning window size of FBSS. For Figure 3.4(a), (b) and (c), 1D-FBSS is applied along the time dimension, where the window widths in the time dimension are 80, 150 and 200, respectively. By contrast, 2D-FBSS is used for Figure 3.4 (d), (e) and (f), where the window width is set to 100 in the time dimension while the window lengths in the spatial dimension are 4, 6 and 7, respectively.

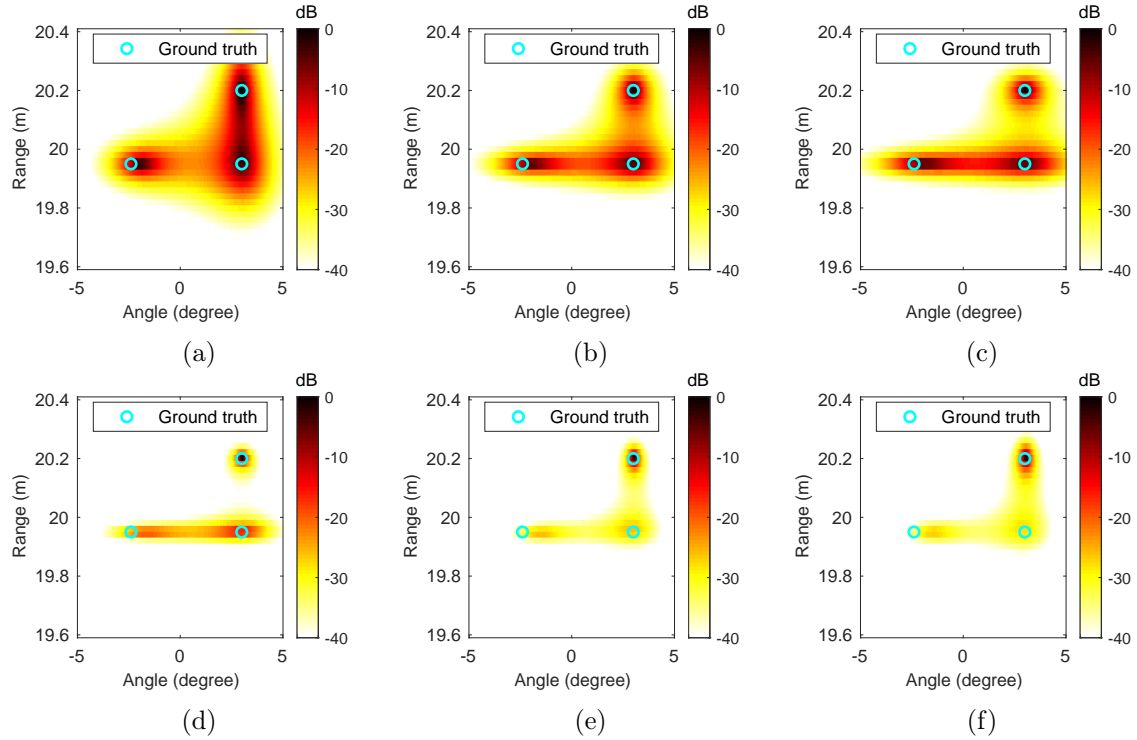


Figure 3.4: The first row contains pseudo spectrum of the multi-static configuration with 1D-FBSS, where window length is set to 8 in spatial dimension while window width is (a) 80, (b) 150, (c) 200 in time dimension. The second row shows estimation results of the mono-static configuration with 2D-FBSS where window width is set to 100 in time dimension but window length is (d) 4, (e) 6, (f) 7 in spatial dimension.

Slices of pseudo spectrum are presented to show the influence of the scanning window size of the FBSS techniques. Figure 3.5 displays slices of pseudo spectrum of the multi-static configuration with 1D-FBSS, where window width is fixed in the spatial dimension but varied in the time dimension. When the window width in the time dimension increases, range resolution increases while azimuth resolution slightly decreases.

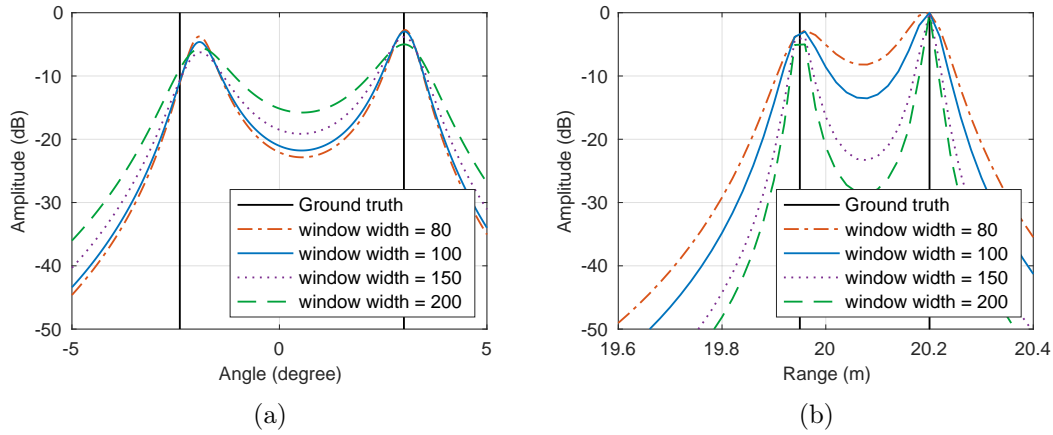


Figure 3.5: Slices of pseudo spectrum of the multi-static configuration with 1D-FBSS, where window length is 8 in spatial dimension but window width is 80, 100, 150, or 200 in time dimension.

Figure 3.6 shows slices of pseudo spectrum of the mono-static configuration with 2D-FBSS, where the size of the window changes only in the spatial dimension. In general, range resolution slightly decreases as the window length in the spatial dimension increases. The ability of decorrelation decreases when the window length in the spatial dimension goes close to the number of elements.

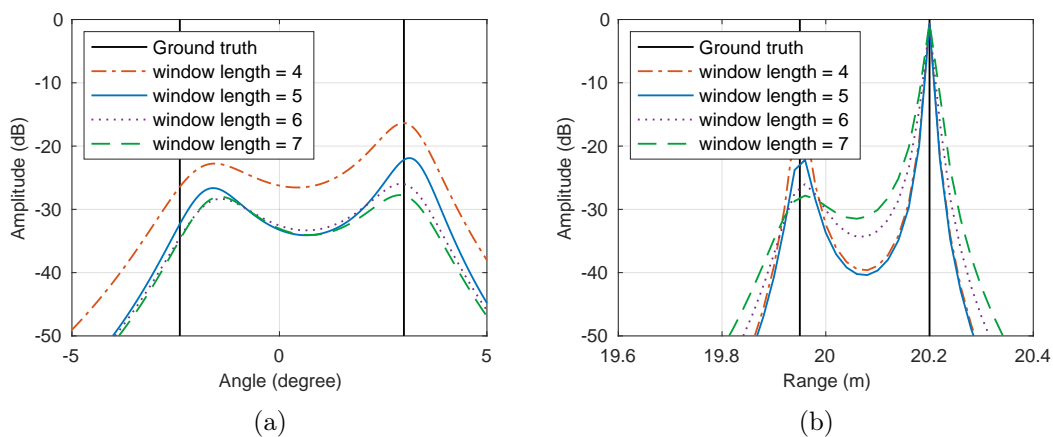


Figure 3.6: Slices of pseudo spectrum of the mono-static configuration with 2D-FBSS, where window width is 100 in time dimension but window length is 4, 5, 6 or 7 in spatial dimension.

According to the results from Figure 3.5 and Figure 3.6, the window size for 1D-FBSS and 2D-FBSS are set to be  $[8 \times 100]$  and  $[5 \times 100]$ , respectively, to balance azimuth and range resolutions in the following simulations.

Two point targets are placed in the same range relative to the radar system to analyze the azimuth resolution for mono-static and multi-static configurations of the system. The performance is compared with a single MIMO since our main aim is to improve the azimuth resolution by jointly using multiple MIMOs. 1D-FBSS is applied to the multi-static configuration of the system. 2D-FBSS is employed to the single MIMO and the mono-static configuration of the system. Figure 3.7 shows that azimuth resolution can be improved by utilizing multiple MIMOs. Figure 3.7 (b) indicates that the multi-static configuration of the system can provide better azimuth resolution compared with the mono-static configuration since it uses extra information of multi-static combinations.

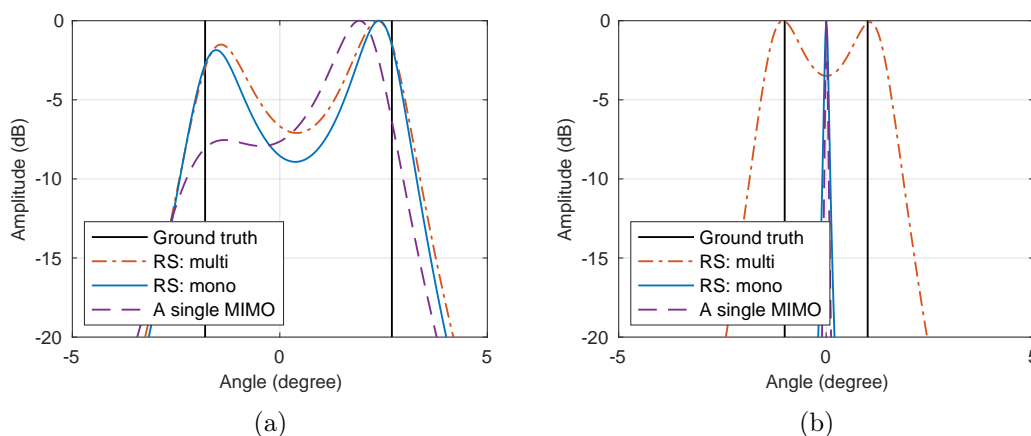


Figure 3.7: Slices of pseudo spectrum of a single MIMO together with multi-static and mono-static configurations of the radar system. Black lines represent ground truth of targets' locations. The orange dash-dot line represents slice of pseudo spectrum of the multi-static configuration of the radar system. The blue line represents slice of pseudo spectrum of the mono-static configuration of the radar system. The purple dashed line represents slice of pseudo spectrum of a single MIMO.

Then two point targets are placed in the same bearing direction relative to the radar system to analyze the down-range resolution. The relative distance between these two targets is  $0.12m$  and  $0.14m$  in Figure 3.8 (a) and (b), respectively.

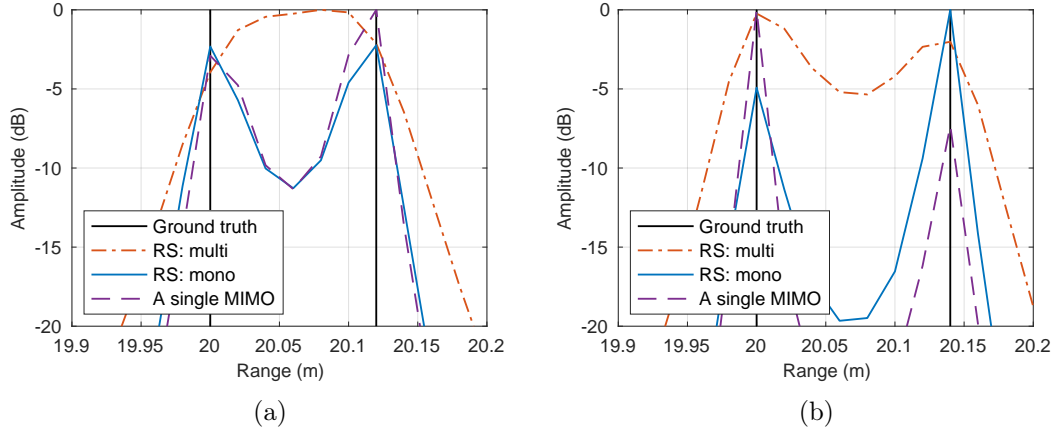


Figure 3.8: Slices of pseudo spectrum of a single MIMO together with multi-static and mono-static configurations of the radar system. Black lines represent ground truth of targets' locations. The orange dash-dot line represents slice of pseudo spectrum of the multi-static configuration of the radar system. The blue line represents slice of pseudo spectrum of the mono-static configuration of the radar system. The purple dashed line represents slice of pseudo spectrum of a single MIMO.

Using chirp information listed in Table 3.1, the Rayleigh range resolution is

$$\delta R = \frac{c}{2B} = 0.25m \quad (3.39)$$

Figure 3.8 (b) indicates that both the single MIMO and the radar system can achieve better down-range resolution compared with the Rayleigh range resolution. Figure 3.8(a) shows the down-range resolution of the multi-static configuration is the worst. One of the reasons is that the multi-static configuration applies 1D-FBSS while the others employ the 2D-FBSS. As observed from Figure 3.3, the 2D-FBSS can improve resolutions compared with the 1D-FBSS.

### 3.5. Conclusions

The generalized 2D-MUSIC algorithm is proposed in this chapter for 2D target localization. It can be used for both multi-static and mono-static configurations of a radar system. The same search grid is employed for all virtual arrays to maintain geometrical constraints of the system. 2D-MUSIC is applied to each virtual array individually, and then estimation results are fused via (3.30) or (3.34) for multi-static/mono-static configuration, respectively. Then targets' positions correspond to the local maxima of the resulting spectrum.

FBSS technique is applied to restore the rank of signal covariance matrix when the scattered signals from different targets are highly correlated or coherent. The main drawback of this technique is that it decreases the maximum number of detectable targets. Fortunately, a side benefit is that it reduces the computational load for determining subspaces by EVD/SVD. Moreover, the size of the scanning window influences the ability of resolutions. However, the optimal selection of window size is an remaining issue which needs further investigation.

Simulation results show that the azimuth resolution can be improved by jointly using multiple MIMOs. The multi-static configuration of the system can provide better azimuth resolution compared to the mono-static one since it uses extra information of multi-static combinations. The generalized 2D-MUSIC algorithm can provide super resolution for every configuration, but the down-range resolution of the multi-static configuration is worse than the mono-static configuration. A possible reason is that 2D-FBSS can improve resolutions compared with 1D-FBSS.

To save computational cost, we can first apply fast Fourier transform (FFT) along the time dimension to reduce the search scope of range, and then use the generalized 2D-MUSIC algorithm to estimate targets' positions. An iterative grid refinement (IGR) method [35] can be employed to minimize the influence of off-grid problems.

# 4

## An Augmented Lagrangian Method

This chapter offers an augmented Lagrangian method for 2D target localization. Due to time limitation, its application only in the mono-static configuration of the radar system is discussed. In principle, this method can be easily used for the multi-static configuration. Section 4.1 analyzes the signal model of the mono-static configuration based on a single MIMO. Section 4.2 extends the sparsity-based C-SALSA for the radar system. Compared with subspace-based algorithms, this method does not require the number of targets as prior knowledge. Section 4.3 validates this algorithm via MATLAB simulations. Conclusions of this chapter are drawn in Section 4.4.

### 4.1. Analysis of Signal Model

From (2.20), we can write time samples in a single sweep, for the  $m^{\text{th}}$  MIMO, into a data matrix  $\mathbf{X}_m \in \mathbb{C}^{P \times N}$ . Then stacking the data matrix into a vector  $\mathbf{x}_m$  column by column, we have

$$\begin{aligned}\mathbf{x}_m &= \sum_{k=1}^K \mathbf{b}_m(r_k, \theta_k) (\gamma_k e^{j\phi_k}) + \mathbf{w}_m \\ &= \mathbf{B}_m \mathbf{s} + \mathbf{w}_m\end{aligned}\tag{4.1}$$

where  $m = -M, \dots, M$ ,  $\mathbf{s} \in \mathbb{C}^{K \times 1}$  is a vector of the reflectivities of all targets, and  $\mathbf{w}_m \in \mathbb{C}^{NP \times 1}$  stacks the complex AWGN of the  $m^{\text{th}}$  MIMO in a column vector. The

matrix  $\mathbf{B}_m \in \mathbb{C}^{NP \times K}$  is called array manifold matrix, whose columns are steering vectors of all targets

$$\mathbf{B}_m = [\mathbf{b}_m(r_1, \theta_1), \dots, \mathbf{b}_m(r_K, \theta_K)] \quad (4.2)$$

The steering vector  $\mathbf{b}_m \in \mathbb{C}^{NP \times 1}$  of the  $k^{\text{th}}$  target relative to the  $m^{\text{th}}$  MIMO can be expressed as

$$\mathbf{b}_m(r_k, \theta_k) = \mathbf{b}_m^{(r)}(r_k^{(m)}) \otimes \mathbf{b}_m^{(\theta)}(\theta_k^{(m)}) \quad (4.3)$$

where  $(r_k, \theta_k)$  is the location of the  $k^{\text{th}}$  target relative to the reference MIMO.  $(r_k^{(m)}, \theta_k^{(m)})$  represents the position the  $k^{\text{th}}$  target relative to the  $m^{\text{th}}$  MIMO, which can be obtained from  $(r_k, \theta_k)$  through (2.5) and (2.6).  $\mathbf{b}_m^{(r)} \in \mathbb{C}^{N \times 1}$  and  $\mathbf{b}_m^{(\theta)} \in \mathbb{C}^{P \times 1}$  are the range and DOA steering vectors, for the  $k^{\text{th}}$  target relative to the  $m^{\text{th}}$  MIMO, respectively.

According to the signal model in (2.20), we can write the range and DOA steering vectors ( $\mathbf{b}_m^{(r)}$  and  $\mathbf{b}_m^{(\theta)}$ ) in (4.3) as

$$\mathbf{b}_m^{(r)}(r_k^{(m)}) = \exp \left\{ j2\pi \left[ -f_0 \frac{2r_k^{(m)}}{c} - \frac{1}{2}\mu \left( \frac{2r_k^{(m)}}{c} \right)^2 \right] \right\} \cdot \left[ 1, \dots, \exp \left( j2\pi\mu \frac{2r_k^{(m)}}{c} \frac{N-1}{f_s} \right) \right]^T \quad (4.4)$$

$$\mathbf{b}_m^{(\theta)}(\theta_k^{(m)}) = \left[ \exp \left( j2\pi f_0 \frac{(-Q-1)d \sin(\theta_k^{(m)})}{c} \right), \dots, \exp \left( j2\pi f_0 \frac{Qd \sin(\theta_k^{(m)})}{c} \right) \right]^T \quad (4.5)$$

The targets' locations can be parameterized by their range and DOA information relative to the reference MIMO of the system. Given knowledge of  $\mathbf{x}_m$  and the mapping from targets' locations to the manifold matrix  $\mathbf{B}_m$ , the objective is to find all targets' locations together with estimating the number of targets. Matrix  $\mathbf{B}_m$  is unknown since it depends on targets' locations.

## 4.2. Extended C-SALSA

To cast (4.1) as a sparse representation problem, we introduce an overcomplete representation  $\tilde{\mathbf{B}}_m$  relative to all possible targets' locations [35]. Then divide the area of interest into discrete set of potential targets' locations,  $\{\tilde{r}_1, \tilde{r}_2, \dots, \tilde{r}_{N_d}\}$  and  $\{\tilde{\theta}_1, \tilde{\theta}_2, \dots, \tilde{\theta}_{N_\theta}\}$ , where both  $N_d$  and  $N_\theta$  should be much greater than the number of targets  $K$  [25].

Therefore, for the  $m^{\text{th}}$  MIMO, we have

$$\tilde{\mathbf{B}}_m = \left[ \mathbf{b}_m(\tilde{r}_1, \tilde{\theta}_1), \dots, \mathbf{b}_m(\tilde{r}_1, \tilde{\theta}_{N_\theta}), \dots, \mathbf{b}_m(\tilde{r}_{N_d}, \tilde{\theta}_{N_\theta}) \right] \quad (4.6)$$

where  $m = -M, \dots, M$  represents the indices of the MIMOs.  $\tilde{\mathbf{B}}_m \in \mathbb{C}^{NP \times N_d N_\theta}$  is known and independent of true targets' positions [35].

Now the signal model, for a single sweep of the  $m^{\text{th}}$  MIMO, can be expressed as

$$\mathbf{x}_m = \tilde{\mathbf{B}}_m \tilde{\mathbf{s}} + \mathbf{w}_m \quad (4.7)$$

where  $\tilde{\mathbf{s}} \in \mathbb{C}^{N_d N_\theta \times 1}$  and the  $i^{\text{th}}$  element of  $\tilde{\mathbf{s}}$  is

$$s_i = \begin{cases} \gamma_k e^{j\phi_k}, & \text{if } (r_i, \theta_i) = (r_k, \theta_k); \\ 0, & \text{otherwise.} \end{cases} \quad (4.8)$$

where  $i = 1, \dots, N_r N_\theta$  and  $k = 1, \dots, K$ .

Consequently, we can transfer the problem from estimating unknown targets' locations to the problem of sparse spectrum estimation of  $\tilde{\mathbf{s}}$  thanks to the overcomplete representation of  $\tilde{\mathbf{B}}_m$  [35].

The simplest version of problem (4.7), without taking noise into account, can be solved through an optimization procedure

$$\begin{aligned} & \underset{\tilde{\mathbf{s}}}{\text{minimize}} && \|\tilde{\mathbf{s}}\|_0 \\ & \text{subject to} && \mathbf{x}_m = \tilde{\mathbf{B}}_m \tilde{\mathbf{s}} \end{aligned} \quad (4.9)$$

However, (4.9) is a non-convex problem and even intractable for medium-sized problems [35]. Many approximations have been discussed, such as  $l_1$  and  $l_p$  relaxations, where  $\|x\|_0$  is replaced by  $\|x\|_1$  [36]

$$\begin{aligned} & \underset{\tilde{\mathbf{s}}}{\text{minimize}} && \|\tilde{\mathbf{s}}\|_1 \\ & \text{subject to} && \mathbf{x}_m = \tilde{\mathbf{B}}_m \tilde{\mathbf{s}} \end{aligned} \quad (4.10)$$

or  $\|x\|_p$  with  $0 < p < 1$  [37]

$$\begin{aligned} & \underset{\tilde{\mathbf{s}}}{\text{minimize}} && \|\tilde{\mathbf{s}}\|_p \\ & \text{subject to} && \mathbf{x}_m = \tilde{\mathbf{B}}_m \tilde{\mathbf{s}} \end{aligned} \quad (4.11)$$

These two approximations can obtain exact solutions if  $\tilde{\mathbf{s}}$  is sparse enough relative to  $\tilde{\mathbf{B}}_m$

[38]. Moreover, [39] shows that sparse representations can be stable with sufficient sparsity and a favorable structure of the overcomplete dictionary.  $l_1$  relaxation is preferred since (4.10) is a convex optimization problem, while (4.11) is non-convex and hard to solve. In addition, (4.10) is in the framework of basis pursuit [24].

Now, by taking noise into account, (4.10) can be modified as

$$\begin{aligned} & \underset{\tilde{\mathbf{s}}}{\text{minimize}} && \|\tilde{\mathbf{s}}\|_1 \\ & \text{subject to} && \left\| \tilde{\mathbf{B}}_m \tilde{\mathbf{s}} - \mathbf{x}_m \right\|_2 \leq \epsilon_m \end{aligned} \quad (4.12)$$

where  $\epsilon_m \geq 0$  is a parameter which depends on standard noise deviation.

Then we can extend (4.12) for the radar system, which in total contains  $(2M + 1)$  MIMOs, as

$$\begin{aligned} & \underset{\tilde{\mathbf{s}}}{\text{minimize}} && \|\tilde{\mathbf{s}}\|_1 \\ & \text{subject to} && \left\{ \begin{array}{l} \left\| \tilde{\mathbf{B}}_{-M} \tilde{\mathbf{s}} - \mathbf{x}_{-M} \right\|_2 \leq \epsilon_{-M} \\ \vdots \\ \left\| \tilde{\mathbf{B}}_M \tilde{\mathbf{s}} - \mathbf{x}_M \right\|_2 \leq \epsilon_M \end{array} \right. \end{aligned} \quad (4.13)$$

(4.13) is a constrained sparse optimization problem, which can be solved by variable splitting and augmented Lagrangian (AL). Therefore, C-SALSA in [28] is extended to solve the target localization problem with multiple MIMOs.

Following [28], the constrained problem (4.13) can be transformed into an unconstrained one (4.15) by adding the indicator functions of feasible sets,

$$\left\{ \tilde{\mathbf{s}} : \sum_{m=-M}^M \left( \left\| \tilde{\mathbf{B}}_m \tilde{\mathbf{s}} - \mathbf{x}_m \right\|_2^2 \leq \epsilon_m \right) \right\} \quad (4.14)$$

to the objective function in (4.13),

$$\underset{\tilde{\mathbf{s}}}{\text{minimize}} \quad \lambda_1 \|\tilde{\mathbf{s}}\|_1 + \sum_{m=-M}^M \iota_{E(\epsilon_m, \mathbf{I}, \mathbf{x}_m)}(\tilde{\mathbf{B}}_m \tilde{\mathbf{s}}) \quad (4.15)$$

where  $\lambda_1 > 0$  controls the importance of sparsity, and  $\iota_{E(\epsilon_m, \mathbf{I}, \mathbf{x}_m)}(\tilde{\mathbf{B}}_m \tilde{\mathbf{s}})$  is the indicator function of the feasible set  $E(\epsilon_m, \mathbf{I}, \mathbf{x}_m)$ :

$$E(\epsilon_m, \mathbf{I}, \mathbf{x}_m) = \{ \tilde{\mathbf{s}} \in \mathbb{C}^{(N_d N_\theta \times 1)} : \|\mathbf{I} \tilde{\mathbf{s}} - \mathbf{x}_m\|_2 \leq \epsilon_m \} \quad (4.16)$$

$$\iota_Y(\mathbf{y}) = \begin{cases} 0, & \text{if } \mathbf{y} \in Y \\ +\infty, & \text{if } \mathbf{y} \notin Y \end{cases} \quad (4.17)$$

(4.15) can be rewritten as

$$\underset{\tilde{\mathbf{s}}}{\text{minimize}} \quad \sum_{i=0}^{2M+1} g_i(\mathbf{H}^{(i)}\tilde{\mathbf{s}}) \quad (4.18)$$

where

$$g_i = \begin{cases} \lambda_1 \|\cdot\|_1, & \text{for } i = 0; \\ \iota_{E(\epsilon_m, \mathbf{I}, \mathbf{x}_m)}, & \text{for } \begin{cases} i = 1, \dots, 2M+1 \\ m = i - (M+1) \end{cases} \end{cases} \quad (4.19)$$

$$\mathbf{H}^{(i)} = \begin{cases} \mathbf{I} & \text{for } i = 0; \\ \tilde{\mathbf{B}}_m & \text{for } \begin{cases} i = 1, \dots, 2M+1 \\ m = i - (M+1) \end{cases} \end{cases} \in \mathbb{C}^{a_i \times N_d N_\theta} \quad (4.20)$$

and

$$a_i = \begin{cases} N_d N_\theta & \text{for } i = 0; \\ NP & \text{for } i = 1, \dots, 2M+1. \end{cases} \quad (4.21)$$

We can further rewrite (4.18) as a constrained problem

$$\begin{aligned} & \underset{\mathbf{z}}{\text{minimize}} && f(\mathbf{z}) \\ & \text{subject to} && \mathbf{z} - \mathbf{G}\tilde{\mathbf{s}} = \mathbf{0} \end{aligned} \quad (4.22)$$

where

$$f(\mathbf{z}) = \sum_{i=0}^{2M+1} g_i(\mathbf{z}^{(i)}) = \sum_{i=0}^{2M+1} g_i(\mathbf{H}^{(i)}\tilde{\mathbf{s}}) \quad (4.23)$$

$$\mathbf{G} = \begin{bmatrix} \mathbf{H}^{(0)} \\ \vdots \\ \mathbf{H}^{(2M+1)} \end{bmatrix} \in \mathbb{C}^{a \times N_r N_\theta} \quad (4.24)$$

$$\mathbf{z} = \left[ (\mathbf{z}^{(0)})^T, \dots, (\mathbf{z}^{(2M+1)})^T \right]^T \in \mathbb{C}^{a \times 1} \quad (4.25)$$

and  $a = a_0 + \dots + a_{(2M+1)}$ . In addition, all objective functions in (4.19) are closed, proper and convex [28].

The AL for (4.22) is

$$\mathcal{L}_\rho(\tilde{\mathbf{s}}, \mathbf{z}, \mathbf{y}) = f(\mathbf{z}) + \mathbf{y}^H (\mathbf{z} - \mathbf{G}\tilde{\mathbf{s}}) + \frac{\rho}{2} \|\mathbf{G}\tilde{\mathbf{s}} - \mathbf{z}\|_2^2 \quad (4.26)$$

where  $\mathbf{y}$  is a vector Lagrange multiplier and  $\rho > 0$  is the AL penalty parameter.

By completing the squares, (4.26) can be written in a slightly different form

$$\mathcal{L}_\rho(\tilde{\mathbf{s}}, \mathbf{z}, \mathbf{d}) = f(\mathbf{z}) + \frac{\rho}{2} \|\mathbf{G}\tilde{\mathbf{s}} - \mathbf{z} - \mathbf{d}\|_2^2 - \frac{\rho}{2} \|\mathbf{d}\|_2^2 \quad (4.27)$$

where  $\mathbf{d} = (1/\rho)\mathbf{y}$  is the scaled dual variable.

We can express ADMM with

$$\mathbf{z}_k = \begin{bmatrix} \mathbf{z}_k^{(0)} \\ \vdots \\ \mathbf{z}_k^{(2M+1)} \end{bmatrix} \quad \text{and} \quad \mathbf{d}_k = \begin{bmatrix} \mathbf{d}_k^{(0)} \\ \vdots \\ \mathbf{d}_k^{(2M+1)} \end{bmatrix} \quad (4.28)$$

then using the scaled dual variable, we have

$$\tilde{\mathbf{s}}_{k+1} = \underset{\tilde{\mathbf{s}}}{\operatorname{argmin}} \frac{\rho}{2} \|\mathbf{G}\tilde{\mathbf{s}} - \mathbf{z}_k - \mathbf{d}_k\|_2^2 \quad (4.29)$$

The matrix  $\mathbf{G}$  has full column rank since  $\mathbf{H}^{(0)} = \mathbf{I}$ . Hence  $\tilde{\mathbf{s}}_{k+1}$  has a unique solution, and it can be further expressed as

$$\begin{aligned} \tilde{\mathbf{s}}_{k+1} &= (\mathbf{G}^H \mathbf{G})^{-1} \mathbf{G}^H (\mathbf{z}_k + \mathbf{d}_k) \\ &= \left[ \sum_{i=0}^{2M+1} (\mathbf{H}^{(i)})^H \mathbf{H}^{(i)} \right]^{-1} \sum_{i=0}^{2M+1} [(\mathbf{H}^{(i)})^H (\mathbf{z}_k^{(i)} + \mathbf{d}_k^{(i)})] \end{aligned} \quad (4.30)$$

where the second equality is obtained by using (4.24).

$$\mathbf{z}_{k+1} = \underset{\mathbf{z}}{\operatorname{argmin}} \left( f(\mathbf{z}) + \frac{\rho}{2} \|\mathbf{G}\tilde{\mathbf{s}}_{k+1} - \mathbf{z} - \mathbf{d}_k\|_2^2 \right) \quad (4.31)$$

$$\mathbf{d}_{k+1} = \mathbf{d}_k - (\mathbf{G}\tilde{\mathbf{s}}_{k+1} - \mathbf{z}_{k+1}) \quad (4.32)$$

Specifically, in (4.31), minimization for  $\mathbf{z}^{(0)}, \dots, \mathbf{z}^{(2M+1)}$  are decoupled, which means they can be updated separately,

$$\mathbf{z}_{k+1}^{(i)} = \underset{\mathbf{z}^{(i)}}{\operatorname{argmin}} \left( g_i(\mathbf{z}^{(i)}) + \frac{\rho}{2} \|\mathbf{z}^{(i)} - \mathbf{u}_k^{(i)}\|_2^2 \right) \quad (4.33)$$

where  $i = 0, \dots, 2M + 1$ , and

$$\mathbf{u}_k^{(i)} = \mathbf{H}^{(i)} \tilde{\mathbf{s}}_{k+1} - \mathbf{d}_k^{(i)} \quad (4.34)$$

The Moreau proximal map of  $g_0 = \lambda_1 \|\cdot\|_1$  is

$$\mathbf{\Psi}^{(0)}(\mathbf{u}^{(0)}) = \text{soft}(\mathbf{u}^{(0)}, \lambda_1/\rho) \quad (4.35)$$

where  $\text{soft}(\mathbf{u}^{(0)}, \lambda_1/\rho)$  is the element-wise application of soft-threshold function [40]

$$\text{soft}(\mathbf{u}^{(0)}, \lambda_1/\rho) = \text{sign}(\mathbf{u}^{(0)}) \cdot \max(0, |\mathbf{u}^{(0)}| - \lambda_1/\rho) \quad (4.36)$$

It is recommended to update the value of  $\lambda_1$  and  $\rho$  during iterations [41]. Moreover, the gradient of  $\lambda_1$  should be no greater than the change rate of  $\rho$  because the threshold value of soft-threshold function should not become larger during iterations.

The Moreau proximal map of  $g_i = \iota_{E(\epsilon_m, \mathbf{I}, \mathbf{x}_m)}$ , where  $i = 1, \dots, 2M + 1$  and  $m = i - (M + 1)$ , is independent of the AL penalty parameter and represents the orthogonal projection of  $\mathbf{u}^{(i)}$  into the closes  $\epsilon_m$ -radius ball centered at  $\mathbf{x}_m$  [28],

$$\mathbf{\Psi}^{(i)}(\mathbf{u}^{(i)}) = \begin{cases} \mathbf{u}^{(i)}, & \text{if } \|\mathbf{u}^{(i)} - \mathbf{x}_m\|_2 \leq \epsilon_m \\ \mathbf{x}_m + \epsilon_m \frac{\mathbf{u}^{(i)} - \mathbf{x}_m}{\|\mathbf{u}^{(i)} - \mathbf{x}_m\|_2}, & \text{if } \|\mathbf{u}^{(i)} - \mathbf{x}_m\|_2 > \epsilon_m \end{cases} \quad (4.37)$$

Furthermore,  $\mathbf{d}^{(0)}, \dots, \mathbf{d}^{(2M+1)}$  can also be updated separately,

$$\mathbf{d}_{k+1}^{(i)} = \mathbf{d}_k^{(i)} - \left( \mathbf{H}^{(i)} \tilde{\mathbf{s}}_{k+1} - \mathbf{z}_{k+1}^{(i)} \right) \quad (4.38)$$

In summary, the extended C-SALSA for the mono-static configuration of a radar system is presented in Algorithm 1.

---

**Algorithm 1** the extended C-SALSA for the mono-static configuration of a radar system

---

- 1: Set  $k = 0$ , choose  $\lambda_1 > 0$ ,  $\rho > 0$ ,  $\mathbf{z}_0^{(0)}, \dots, \mathbf{z}_0^{(2M+1)}, \mathbf{d}_0^{(0)}, \dots, \mathbf{d}_0^{(2M+1)}$
  - 2: **repeat**
  - 3:    $\mathbf{v}_k = \left[ \sum_{i=0}^{2M+1} \left( \mathbf{H}^{(i)} \right)^H \mathbf{H}^{(i)} \right]^{-1}$
  - 4:    $\mathbf{r}_k = \sum_{i=0}^{2M+1} \left[ \left( \mathbf{H}^{(i)} \right)^H \left( \mathbf{z}_k^{(i)} + \mathbf{d}_k^{(i)} \right) \right]$
  - 5:    $\tilde{\mathbf{s}}_{k+1} = \mathbf{v}_k \mathbf{r}_k$
  - 6:   **for**  $i = 0, \dots, 2M + 1$  **do**
  - 7:      $\mathbf{u}_k^{(i)} = \mathbf{H}^{(i)} \tilde{\mathbf{s}}_{k+1} - \mathbf{d}_k^{(i)}$
  - 8:      $\mathbf{z}_{k+1}^{(i)} = \Psi^{(i)} \left( \mathbf{u}_k^{(i)} \right)$
  - 9:      $\mathbf{d}_{k+1}^{(i)} = \mathbf{d}_k^{(i)} - \left( \mathbf{H}^{(i)} \tilde{\mathbf{s}}_{k+1} - \mathbf{z}_{k+1}^{(i)} \right)$
  - 10:   **end for**
  - 11:    $k \leftarrow k + 1$
  - 12: **until** some stopping criterion is satisfied.
-

### 4.3. Simulations

Numerical simulations are performed with the parameters of chirp signals and the radar system listed in Table 3.1 and Table 3.2, respectively. We use three identical coherent FMCW MIMOs in the radar system. Each MIMO has  $N_{Tx}$  transmitters and  $N_{Rx}$  receivers. The performance of the extended C-SALSA will be analyzed in Cartesian coordinate system. Search steps are  $\Delta x = 0.05m$  and  $\Delta y = 0.1m$  along the  $x$ - and  $y$ -axes, respectively. The SNR is set to be 20 dB in the following simulations.

Firstly, the performance of a single MIMO is discussed to validate the feasibility of C-SALSA. Figure 4.1 shows estimation results of two different MIMO configurations.

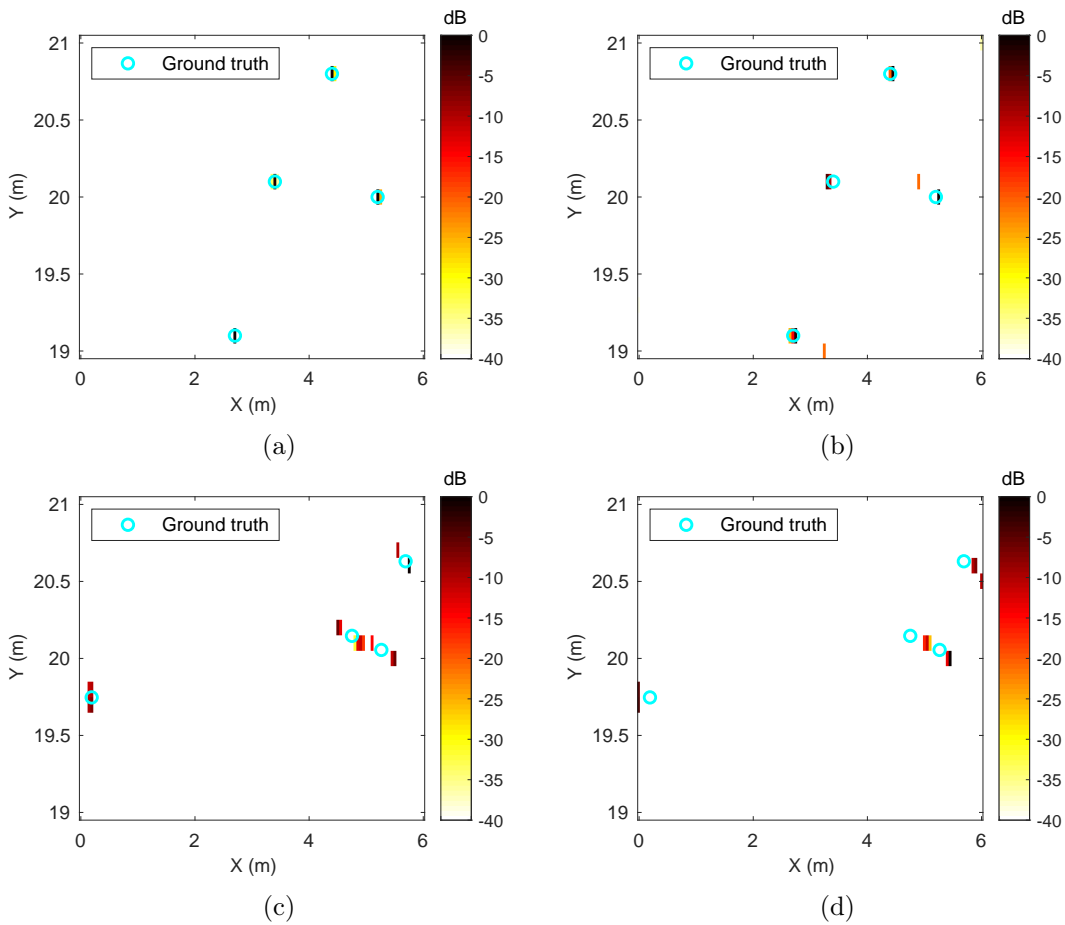


Figure 4.1: Estimation results of 4 on-grid targets by a single MIMO, (a) 5 transmitters and 6 receivers, (b) 2 transmitters and 4 receivers. Estimation results of 4 off-grid targets by a single MIMO, (c) 5 transmitters and 6 receivers, (d) 2 transmitters and 4 receivers.

Figure 4.1 (a) and (c) are estimation results of a single MIMO with 5 transmitters and 6 receivers while Figure 4.1 (b) and (d) are obtained with a single MIMO consisting of 2 transmitters and 4 receivers. Comparing Figure 4.1(a) with (b), one can see that

C-SALSA can provide accurate estimation for on-grid targets, but ghost targets appear with few sensors. However, the amplitude of ghost targets are more than 10 dB lower than real targets. Therefore, we can set a threshold to filter them out. The performance is more robust with large elements because the amount of information increases as the number of elements increases. From the perspective of information theory, more information about a certain observing domain can provide more robust result. Figure 4.1(c) and (d) shows that the off-grid problem exists in both MIMO settings which is caused by the inherent limitation of C-SALSA.

Then we will analyze the performance of a radar system to demonstrate the feasibility of the extended C-SALSA. Figure 4.2 and Figure 4.3 display estimation results of 4 on-grid or off-grid targets by a radar system which contains 3 identical MIMOs, respectively. In addition, each MIMO has 5 transmitters and 6 receivers.

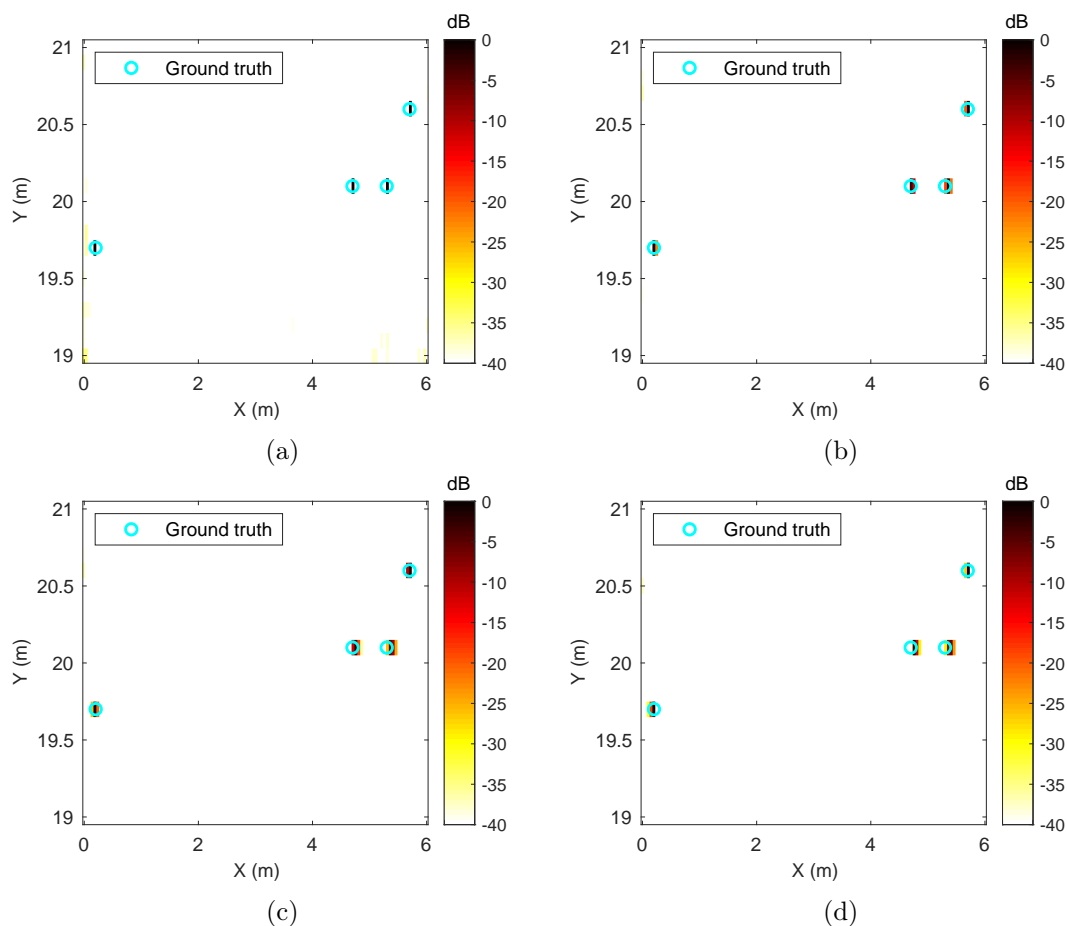


Figure 4.2: Estimation results of 4 on-grid targets where each MIMO has 5 transmitters and 6 receivers, (a) jointed 3 MIMOs, (b) the left MIMO, (c) the center MIMO, (d) the right MIMO.

Figure 4.2 (a) shows the estimation result by jointly using all MIMOs in the radar system, where all targets are precisely located without any ghost target. Meanwhile,

Figure 4.2 (b), (c) and (d) display the individual estimation results of each MIMO in the system. Comparing them with Figure 4.2 (a), it can be found that the estimation accuracy can be improved by jointly using multiple MIMOs.

By contrast, Figure 4.3 (a) shows the estimation result of the off-grid targets with jointly employing all MIMOs in the radar system while Figure 4.3 (b), (c) and (d) present the individual estimation results of each MIMO in the radar system. These figures indicate that jointly using multiple MIMOs cannot reduce the influence of off-grid problems.

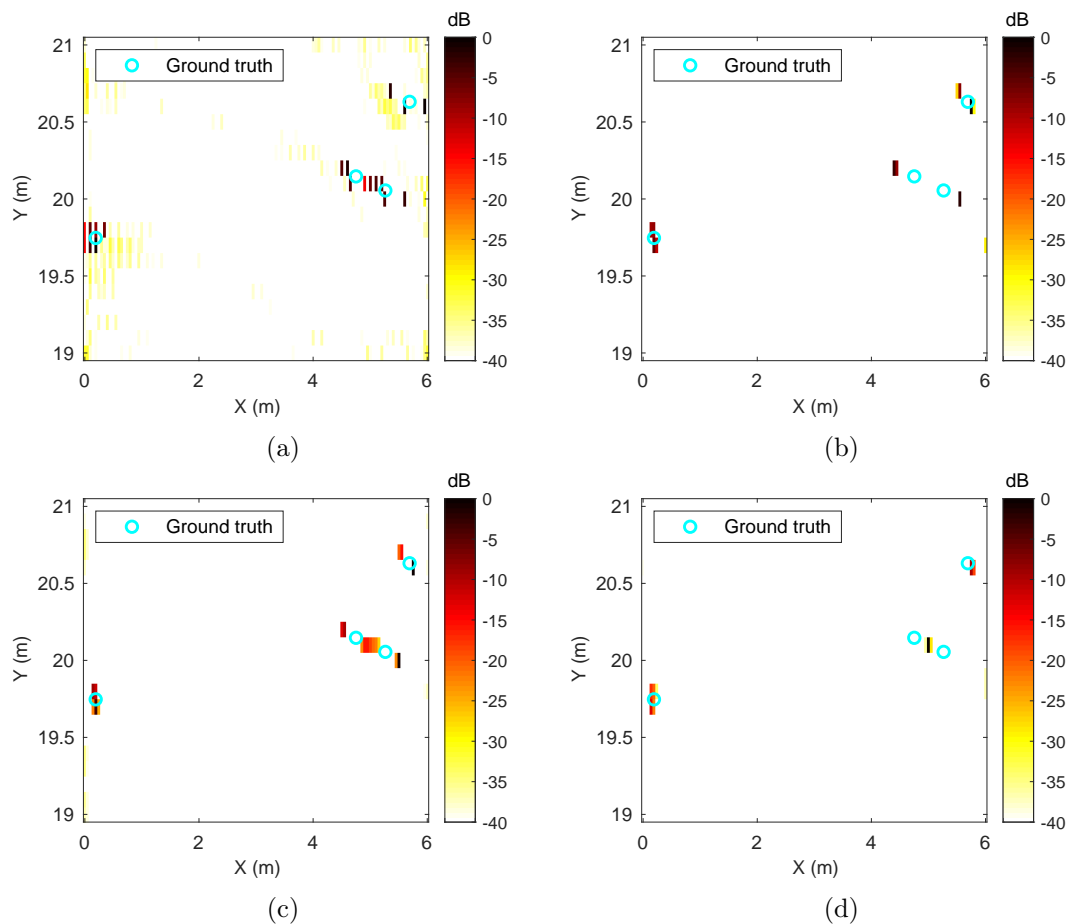


Figure 4.3: Estimation results of 4 off-grid targets where each MIMO has 5 transmitters and 6 receivers, (a) jointed 3 MIMOs, (b) the left MIMO, (c) the center MIMO, (d) the right MIMO.

To further demonstrate the performance of extended C-SALSA, one more numerical simulation is carried out with MIMO arrays consisting of two transmitters and four receivers. Similar to the previous simulation, a radar system with three MIMO arrays is considered. Figure 4.4 and Figure 4.5 display estimation results of 4 on-grid or off-grid targets.

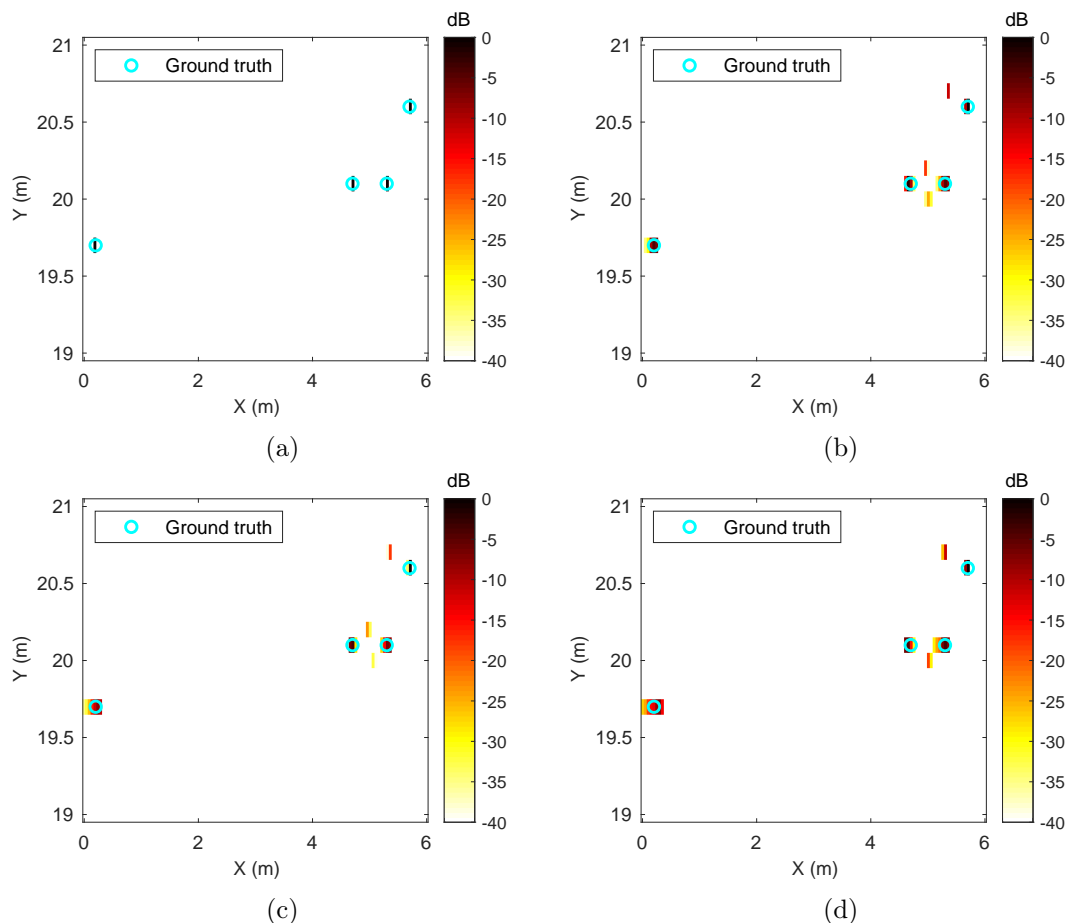


Figure 4.4: Estimation results of 4 on-grid targets where each MIMO has 2 transmitters and 4 receivers, (a) jointed 3 MIMOs, (b) the left MIMO, (c) the center MIMO, (d) the right MIMO.

Figure 4.4 (a) shows the estimation result by jointly using all MIMOs in the radar system, where all targets are accurately estimated without causing any ghost target. Figure 4.4 (b), (c) and (d) display the individual estimation result of each MIMO in the radar system. Ghost targets can be seen in each individual estimation result, but it is possible to filter them out by setting a threshold for detection. Comparing Figure 4.4 with Figure 4.2, ghost targets appear in the estimation result of a single MIMO with few sensors, but jointly utilizing multiple MIMOs can improve the robustness of the estimation.

Figure 4.5 (a) displays the estimation result of the off-grid targets by jointly exploiting all MIMOs in the radar system. Figure 4.5 (b), (c) and (d) show the individual estimation results of each MIMO in the radar system. These plots indicate that off-grid problems are unavoidable for this method. Moreover, comparing Figure 4.5 with Figure 4.3, increasing the number of sensors of each MIMO does not suppress the influence of off-grid problems.

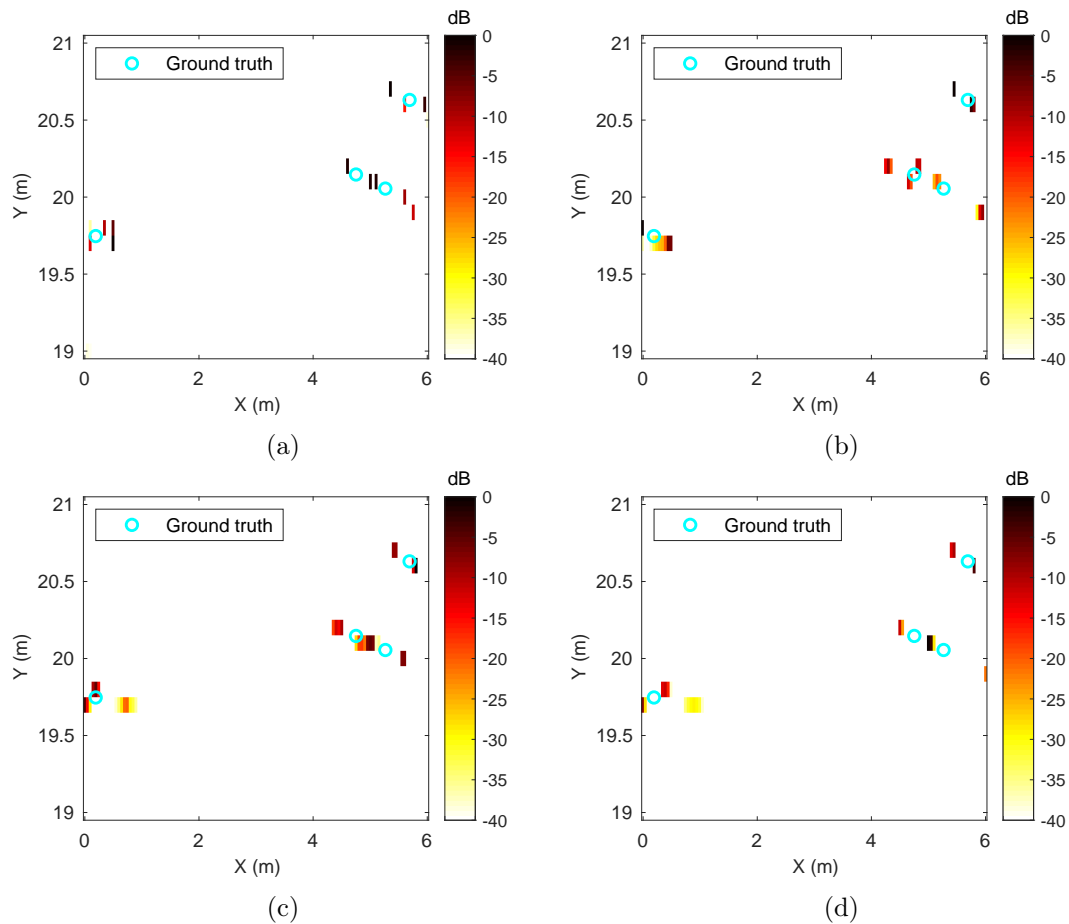


Figure 4.5: Estimation results of 4 off-grid targets where each MIMO has 2 transmitters and 4 receivers, (a) jointed 3 MIMOs, (b) the left MIMO, (c) the center MIMO, (d) the right MIMO.

Figure 4.6 shows the estimation results of the same dataset as Figure 3.3, which is plotted in Polar coordinate system to analyze the azimuth resolution. Figure 4.6 (a) presents the original pseudo spectrum from extended C-SALSA. Since the number of targets is unknown, a threshold is applied for detection. Figure 4.6 (b) displays the filtered pseudo spectrum.

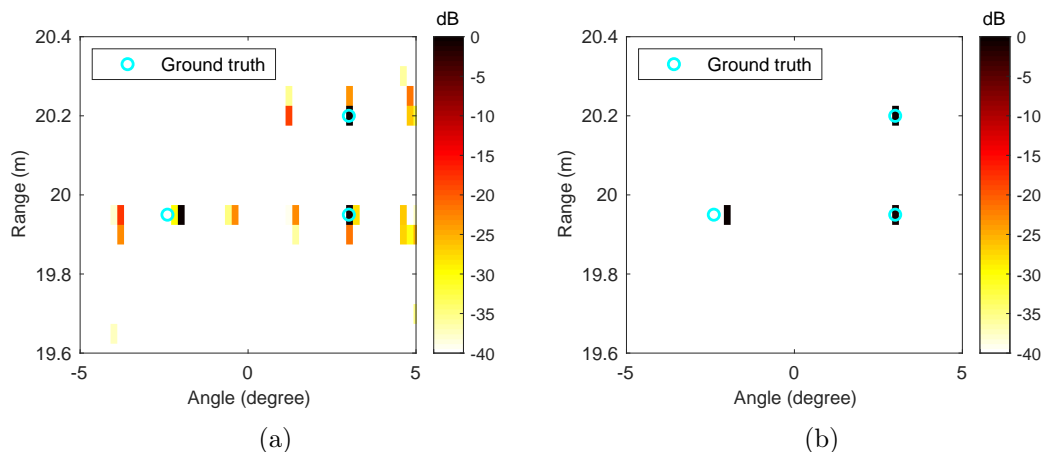


Figure 4.6: Estimation results of 3 point targets via extended C-SALSA with  $\text{SNR} = 15\text{dB}$ : (a) original pseudo spectrum, (b) filtered pseudo spectrum.

The extended C-SALSA is a data-based method, which means it is sensitive to noise. The optimization parameters is not easy to tune when  $\text{SNR}$  equals to 15 dB. Ghost targets appear corresponding to local maximas, but their amplitudes are more than 10 dB lower than that of real targets. Therefore, a threshold is set for detection in Figure 4.6 (b). Comparing Figure 4.6 (b) with Figure 3.3 (e), one can observe that extended C-SALSA have comparable performance with generalized 2D-MUSIC. Moreover, the down-range resolution obtained with the extended C-SALSA is limited by the size of grid.

## 4.4. Conclusions

The extended C-SALSA can find targets' locations together with estimating the number of targets by jointly using multiple MIMOs. This method is an ADMM technique utilizing variable splitting and AL to handle objective functions. Geometrical constraints are remained by applying the same overcomplete dictionary to all virtual arrays. Hence, the information acquired with all small MIMO arrays within the system is fused. However, this estimator suffers from off-grid problems and requires moderate  $\text{SNR}$ . Moreover, the performance of this method is sensitive to optimization parameters when the  $\text{SNR}$  is less than or equal to 15 dB.

# 5

## Performance Analysis

The performance of the proposed algorithms will be analyzed with the mono-static configuration of the system. Parameters of the spectra of a chirp signal for electromagnetic (EM) simulations are presented in section 5.1. The performance of the proposed signal models together with algorithms are analyzed in section 5.2 via MATLAB simulations. Subsection 5.2.1 compares Cramer-Rao Lower Bound (CRLB) for a single MIMO with multi-static and mono-static configurations of the radar system. Subsection 5.2.2 discusses the possible accuracy of the estimation results of the mono-static configuration using CRLB. Subsection 5.2.3 compares resolutions of the generalized 2D-MUSIC and extended C-SALSA. The performance of proposed algorithms are analyzed via EM simulations in section 5.3. Conclusion of this chapter is drawn in section 5.4.

### 5.1. Parameters

Table 5.1 offers key parameters of the chirp spectrum for EM simulations. When using MATLAB to analyze the performance of proposed algorithms, beat signals are utilized to save computational load in time domain. However, EM simulations are done in frequency domain, which means Nyquist criterion should be satisfied when we transfer the chirp spectrum into time domain. In order to reduce computational cost, the sweep duration is set to a quite small value for chirp spectrum.

Table 5.1: Parameters of chirp spectrum for EM simulations

Parameter	Value
Center frequency ( $f_c$ )	76.5GHz
Chirp valid sweep bandwidth ( $B$ )	1GHz
Frequency step ( $\Delta f$ )	2MHz
Sweep duration ( $T_s$ )	0.5 $\mu$ s
ADC sampling rate ( $f_s$ )	154GHz
Downsampling factor	100
The number of samples per chirp after downsampling ( $N$ )	770

## 5.2. MATLAB Simulations

### 5.2.1. Performance Analysis with CRLB

In order to specify a benchmark for performance analysis, CRLB for the general multi-static configuration of the radar system is derived in Appendix A [42]. The CRLB represents a lower bound of the root mean square error (RMSE) for any unbiased estimator [43]. Moreover, CRLB for the mono-static configuration of a system and even a single MIMO can be deduced from its deviation for the multi-static configuration.

Figure 5.1 displays CRLBs of DOA and range for a single MIMO together with multi-static and mono-static configurations of the radar system.

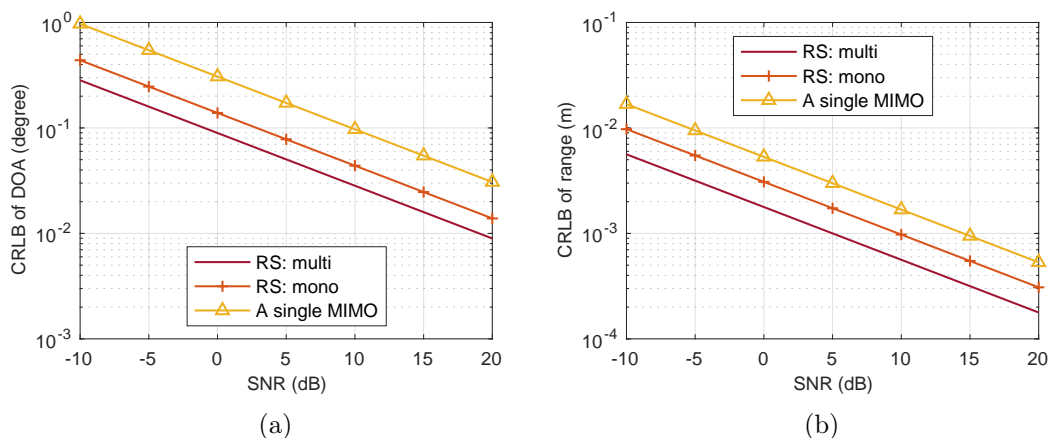


Figure 5.1: CRLB versus SNR of a single MIMO together with multi-static and mono-static configurations of the radar system: (a) DOA, (b) range. The yellow line with upward-pointing triangle represents CRLB of a single MIMO. The orange with plus sign represents CRLB of the mono-static configuration of the radar system. The red line represents CRLB of the multi-static configuration of the radar system.

Tables 3.1, 3.2 and 3.3 contain parameters of chirp signals, the radar system and MIMO, respectively. Since the performance of the generalized MUSIC algorithm will be

compared with the corresponding CRLB, the sampling frequency is reduced to  $0.7MHz$  to save computational cost. Moreover, the target position is  $(5^\circ, 5m)$  relative to the reference MIMO.

Figure 5.1 (a) and (b) indicate that the estimation performance can be improved by jointly using multiple MIMOs. Considering to achieve the same RMSEs of DOA/range, the mono-static configuration can improve estimation performance for SNR of DOA/range about 7 dB/5 dB compared with the performance of a single MIMO. Then the multi-static configuration can further improve estimation performance for SNR of DOA/range about 3.5 dB/5 dB compared with the performance of mono-static configuration.

The performance of generalized 2D-MUSIC estimator is analyzed for both multi-static and mono-static configurations through Monte Carlo simulations. The results are averaged over  $N_i = 400$  trials. Moreover, the performance of the system is compared with that of a single MIMO (here we use the  $0^{th}$  MIMO in Figure 2.1). The RMSE of range and DOA for each target are defined as

$$\sigma_r = \sqrt{\frac{1}{N_i} \sum_{n_i=1}^{N_i} (\hat{r}_{k,n_i} - r_k)^2} \quad \text{and} \quad \sigma_\theta = \sqrt{\frac{1}{N_i} \sum_{n_i=1}^{N_i} (\hat{\theta}_{k,n_i} - \theta_k)^2} \quad (5.1)$$

where  $N_i$  is the number of trials, and  $\hat{r}_{k,n_i}$  and  $\hat{\theta}_{k,n_i}$  represents the estimated range and DOA of the  $k^{th}$  target in the  $n_i^{th}$  Monte Carlo trial, respectively.

The extended C-SALSA is not suitable for drawing an extremely fine search grid within a quite small region, in which case the parameters for optimization process are hard to tune. That is why we do not compare RMSEs of extended C-SALSA with CRLB. Therefore, estimation error level of extended C-SALSA is determined by search step.

Figure 5.2 displays RMSEs of DOA and range for a single target by generalized 2D-MUSIC algorithm, where the RMSEs of both DOA and range are close to their CRLBs for each configuration.

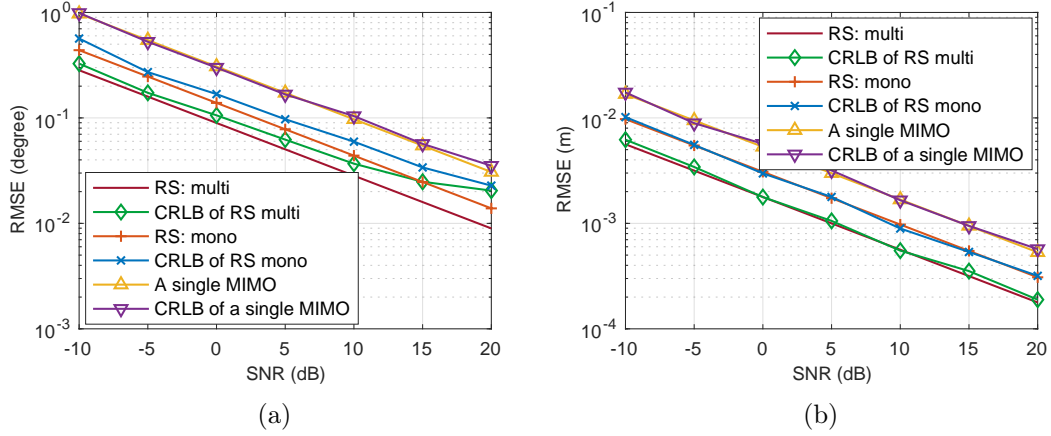


Figure 5.2: RMSE versus SNR for a single target by generalized 2D-MUSIC: (a) DOA, (b) range. The red line represents RMSE of the multi-static configuration of the radar system. The green line with diamond represents CRLB of the multi-static configuration. The orange line with plus sign represents RMSE of the mono-static configuration of the radar system. The blue line with cross represents CRLB of the mono-static configuration. The yellow line with upward-pointing triangle represents RMSE of a single MIMO. The purple line with downward-pointing triangle represents CRLB of a single MIMO.

### 5.2.2. Possible Accuracy Analysis via CRLB

Parameters listed in Tables 3.1, 3.2 and 3.3 is used to analyze the possible accuracy of the radar system. Only the mono-static configuration will be analyzed here, but the multi-static configuration can be discussed in the similar way. A point target is placed at  $(5^\circ, 20m)$  relative to the reference MIMO.

Figures 5.3, 5.4, 5.5 and 5.6 show CRLB of the DOA and range versus bandwidth, the inter-MIMO spacing, the number of elements per virtual array, and the number of MIMOs for the mono-static configuration of the system, respectively. When one parameter is changing, the other parameters are fixed as listed in Tables 3.1, 3.2 and 3.3. When signal bandwidth, the inter-MIMO spacing, the number of elements per virtual array, or the number of MIMOs increases, the CRLBs of both the DOA and range decrease.

Comparing Figures 5.3(a) with 5.4(a), 5.5(a) and 5.6(a), it can be seen that the CRLB of DOA is more sensitive to the inter-MIMO spacing. The correlation of received signals decreases as the inter-MIMO spacing increases; thus more independent information can be used to estimate the targets' positions. Comparing Figures 5.3(b) with 5.4(b), 5.5(b) and 5.6(b), one can find that the CRLB of range is more sensitive to the change of signal bandwidth. The Rayleigh range resolution is decided by the signal bandwidth. The estimation accuracy increases as the range resolution increases. When the number

of elements per MIMO or the number of MIMOs increases, samples in spatial dimension increases. That is to say, the amount of uncorrelated information increases, consequently, the estimation error decreases from the perspective of information theory. Moreover, the estimation of range and DOA is coupled when jointly using multiple MIMOs, which means their estimation accuracy is coupled as well. Therefore, CRLBs of DOA and range have the same trend when the parameters change.

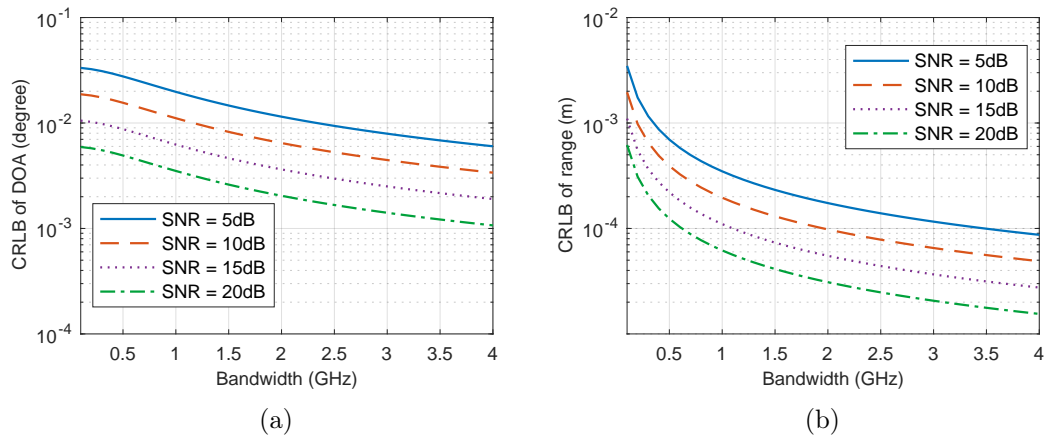


Figure 5.3: CRLB versus bandwidth for a single target: (a) DOA, (b) range.

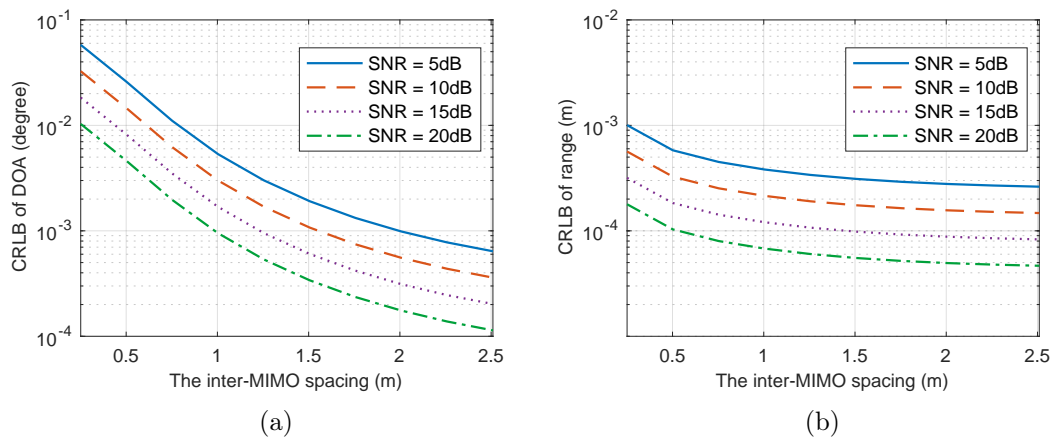


Figure 5.4: CRLB versus the inter-MIMO spacing for a single target: (a) DOA, (b) range.

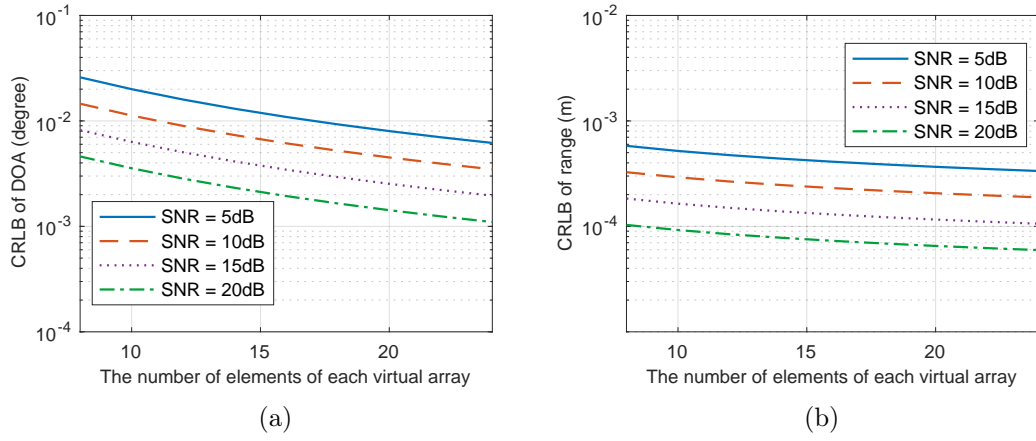


Figure 5.5: CRLB versus the number of elements per virtual array for a single target: (a) DOA, (b) range.

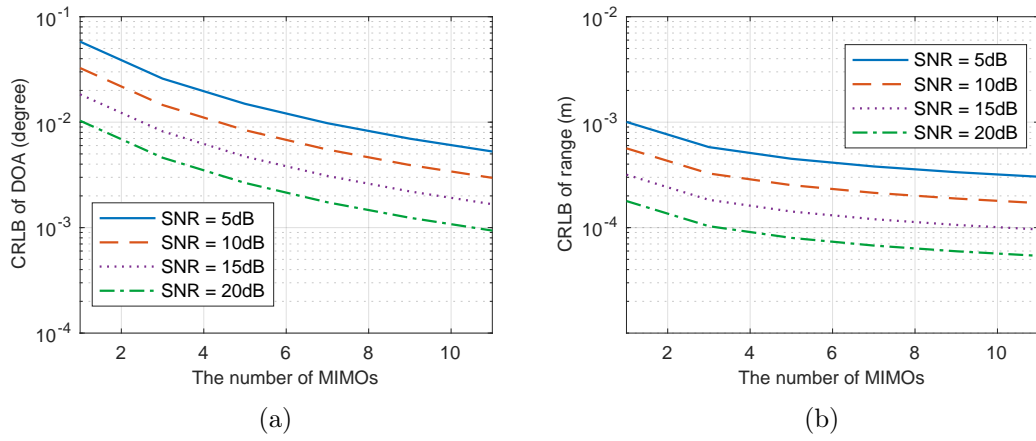


Figure 5.6: CRLB versus the number of MIMOs for a single target: (a) DOA, (b) range.

### 5.2.3. Comparing Resolutions of Proposed Algorithms

The same search grid is employed to compare the resolutions obtained with the generalized 2D-MUSIC algorithm and the extended C-SALSA. Search step in range and azimuth dimensions are  $\Delta R = 0.05m$  and  $\Delta DOA = 0.2^\circ$ , respectively. SNR is set to be 15 dB.

Figure 5.7 (a) displays the slice of the pseudo spectrum for two point targets whose ground truth positions are  $(1^\circ, 20m)$  and  $(3^\circ, 20m)$ . The extended C-SALSA can distinguish these two targets in the mono-static configuration of the system while the generalized 2D-MUSIC algorithm cannot.

Figure 5.7 (b) shows the slice of pseudo spectrum for two point targets whose ground truth positions are  $(-1^\circ, 20m)$  and  $(-1^\circ, 20.2m)$ . Both generalized 2D-MUSIC and extended C-SALSA can achieve better range resolution compared with the Rayleigh range resolution ( $\delta R = 0.25m$ ) defined by the signal bandwidth. Moreover, generalized

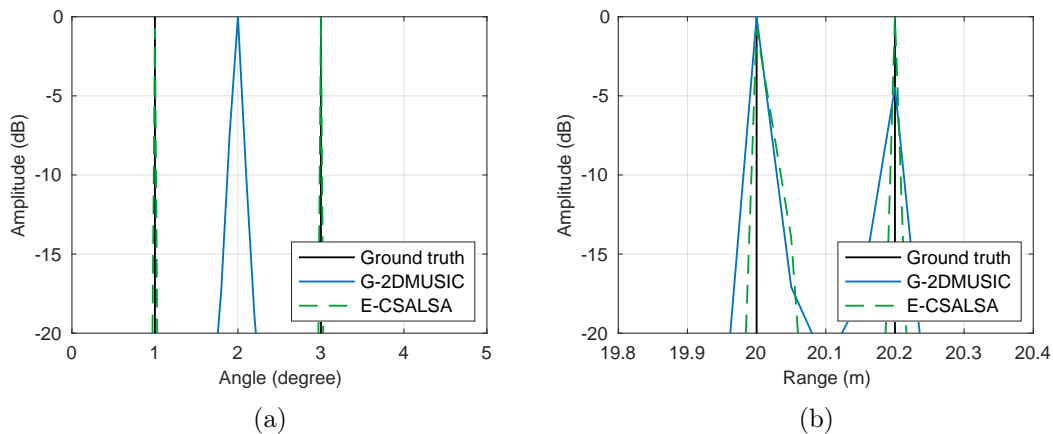


Figure 5.7: slices of pseudo spectrum of the generalized 2D-MUSIC and extended C-SALSA, where (a) two targets locate in the same range relative to the reference MIMO; (b) two targets locate in the same bearing direction relating to the reference MIMO. Black lines represent ground truth of target locations. The blue line represent slice of pseudo spectrum by the generalized 2D-MUSIC algorithm. The green dashed line represents slice of pseudo spectrum by the extended C-SALSA.

2D-MUSIC for the mono-static configuration can achieve range resolution equals to  $0.12m$  as shown in Figure 3.8 (a), but the performance of extended C-SALSA drops when targets are too close. As shown in Figure 5.7 (b), the range resolution of extended C-SALSA is about  $0.2m$ .

### 5.3. Electromagnetic Simulations

Electromagnetic (EM) simulations are initially done with step frequency signals, and then the simulation results are mixed with chirp spectrum to get the synthetic data for FMCW MIMOs. The expression of chirp spectrum is derived in Appendix B, which is used as the carrier signal in the frequency domain. Then we transfer the mixed signals into the time domain and follow (2.9) to obtain beat signals. The performance of proposed algorithms will be analyzed for both point targets and an extended target.

#### 5.3.1. Point targets

Figure 5.8 shows the simulation setup of 3 point targets together with the radar system. Three identical small spheres are placed at  $(2.5m, 19.5m)$ ,  $(3m, 20m)$  and  $(3.5m, 20.5m)$  respectively. Moreover, the circumference of the great circle is less than the wavelength of center frequency. The inter-MIMO spacing is  $0.5m$ .

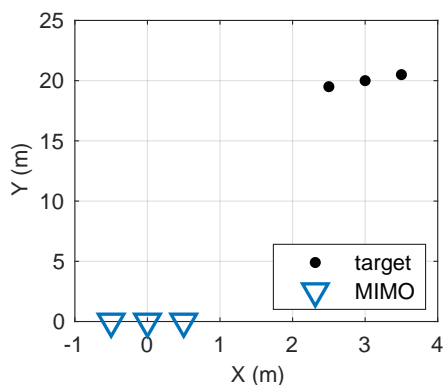


Figure 5.8: Ground truth of 3 point targets with the radar system

### Generalized 2D-MUSIC

Figure 5.9 displays the estimation results of generalized 2D-MUSIC estimator with a single MIMO and a radar system with mono-static and multi-static configurations. 1D-FBSS is applied along the time dimension for all configurations. The performance of mono-static and multi-static configurations of the system is acceptable, because their pseudo spectrum are summation of multiple virtual arrays without weighting.

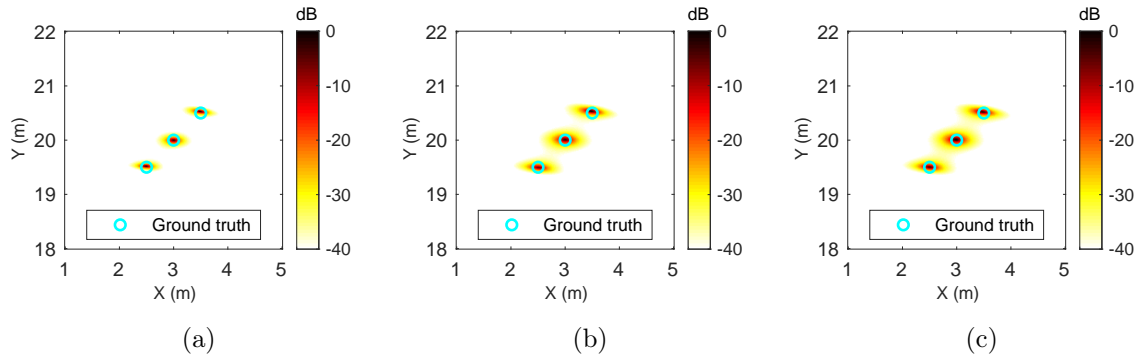


Figure 5.9: Estimation results of 3 point targets by the generalized 2D-MUSIC estimator: (a) a single MIMO, (b) the mono-static configuration of the system, (c) the multi-static configuration of the system.

### Extended C-SALSA

Figure 5.10 shows the estimation results of extended C-SALSA for the mono-static configuration of the system. Because this method does not require the number of targets as prior knowledge, a threshold is applied for detection. Figure 5.10 (b) presents the filtered pseudo spectrum.

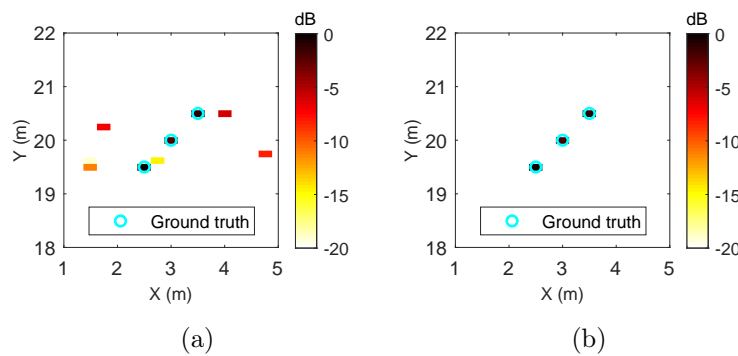


Figure 5.10: Estimation results of 3 point targets by the extended C-SALSA: (a) the original pseudo spectrum, (b) the filtered pseudo spectrum.

Figure 5.9 and Figure 5.10 indicate that both algorithms have the ability to estimate these three point targets.

### 5.3.2. Extended target

Figure 5.11 illustrates the ground truth of an extended target together with the radar system. The relative down-range distance between the car and radar system is  $20m$ . The inter-MIMO spacing is  $0.5m$ . Vertical and horizontal beamwidth of each antenna are  $20^\circ$  and  $120^\circ$  respectively. Two simulation scenarios will be considered: a full-scale car with/without ground. Multipath propagation exists when ground appears.

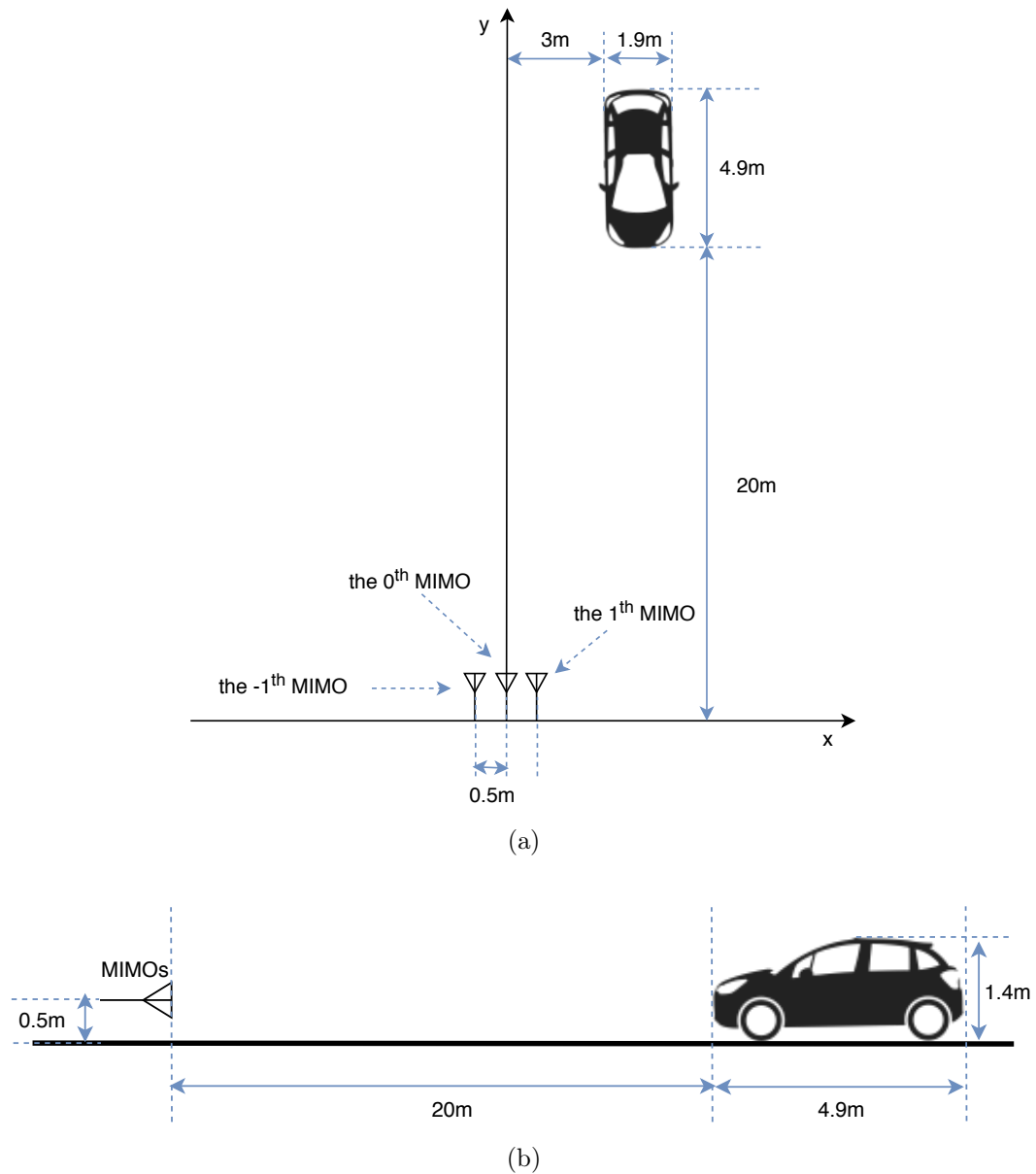


Figure 5.11: Ground truth of an extended target with the radar system: (a) top view, (b) right view.

## Generalized 2D-MUSIC Algorithm

Figure 5.12 displays the pseudo spectrum of the generalized 2D-MUSIC algorithm with a single MIMO and the radar system with mono-static and multi-static configurations when ground exists. In contrast, Figure 5.13 shows the corresponding pseudo spectrum without introducing ground in the simulation scenario. The extended target is 3D but estimation results are displayed in a 2D coordinate. Since the target is far away from the radar system, top view of the extended target can approximately describe the size of target indicated by the blue box in each plot. Moreover, individual estimation result of each virtual array for both multi-static and mono-static configurations are displayed in Appendix C. In addition, we set  $-25$  dB as the threshold for the normalized singular values to estimate the number of targets for each virtual array. Then the maximum value is selected as the estimated number of targets.

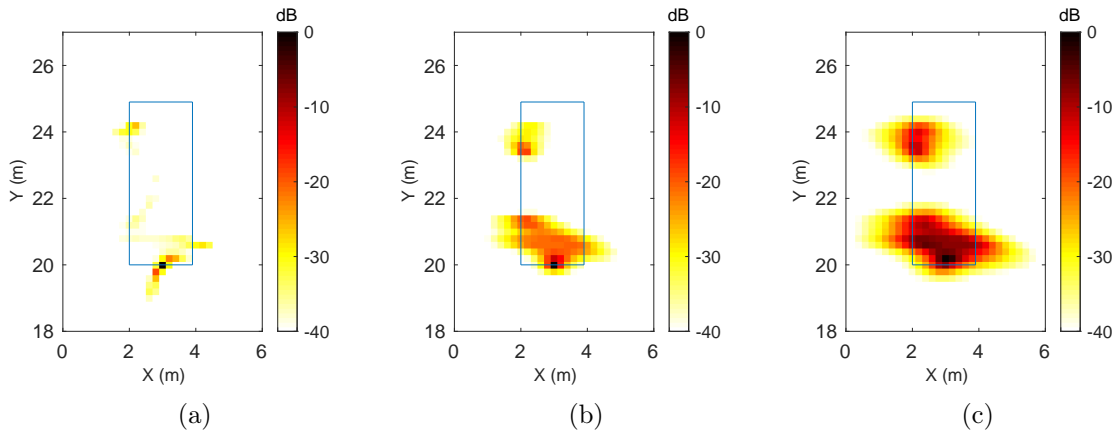


Figure 5.12: Estimation results of an extended target with ground via the generalized 2D-MUSIC algorithm: (a) a single MIMO, (b) the mono-static configuration of the system, (c) the multi-static of the system.

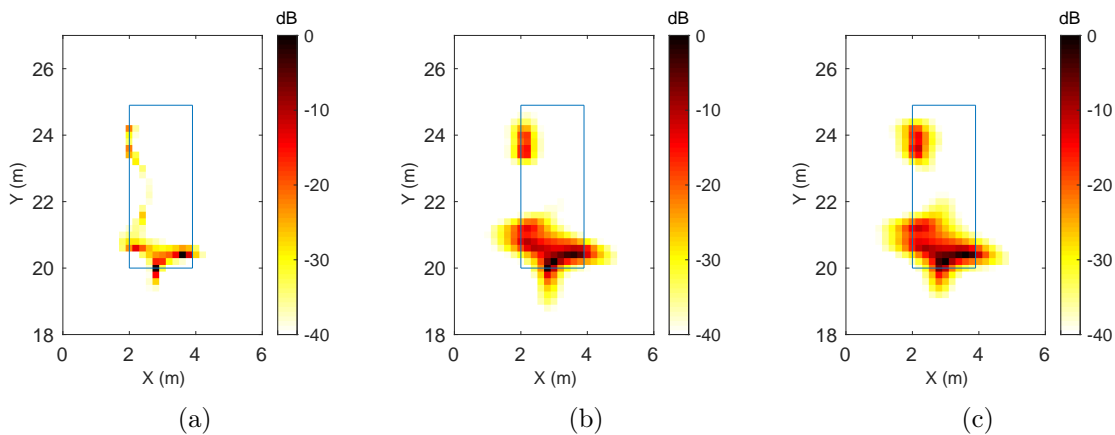


Figure 5.13: Estimation results of an extended target without ground via the generalized 2D-MUSIC algorithm: (a) a single MIMO, (b) the mono-static configuration of the system, (c) the multi-static of the system.

Strong reflection points are corresponding to the front side and wheels of the car. Both Figure 5.12 and Figure 5.13 indicate that more virtual arrays can observe more strong reflection points. Then the estimation result can better represent the target.

Actually, we cannot directly compare Figure 5.12 and Figure 5.13 to analyze the influence of ground in the simulation. Appendix C indicates that strong reflection points for each virtual array could be different. Even the low-rank approximation could be different for different virtual arrays. However, this project assumes every MIMO can observe the same targets, which means we have to provide all virtual arrays with the same model order to separate signal and noise subspaces. The performance of MUSIC-based algorithm could seriously drop if the model order is incorrectly estimated.

### Extended C-SALSA

Figure 5.14 displays the estimation results of mono-static configuration for the extended target with and without ground in the simulation scenarios. The region inside the blue box in each plot approximately indicates the size of the extended target from top view.

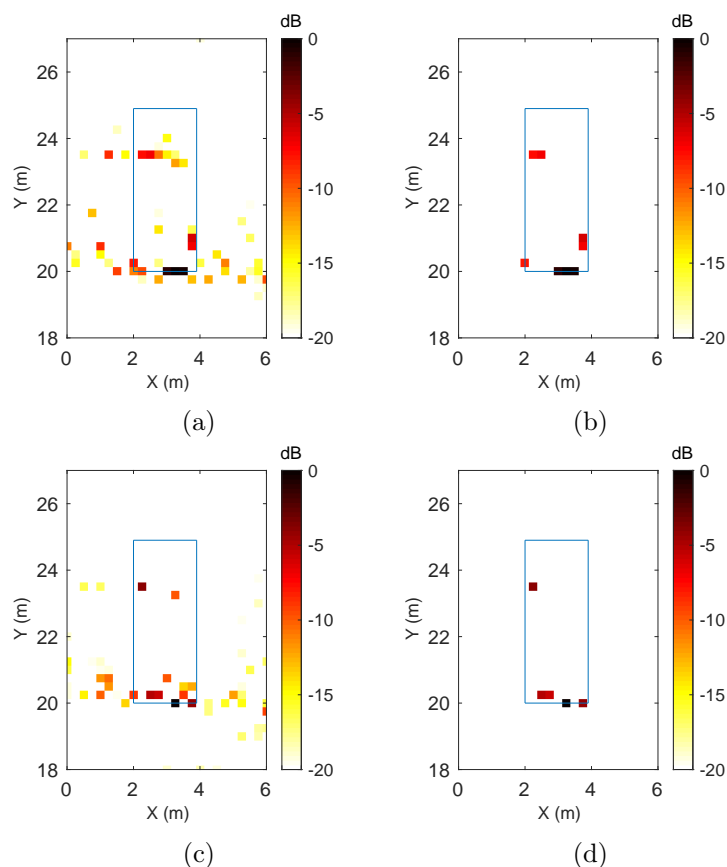


Figure 5.14: Estimation results of an extended target via the extended C-SALSA: (a) the original pseudo spectrum when ground exists, (b) the filtered pseudo spectrum when ground exists, (c) the original pseudo spectrum without ground, (d) the filtered pseudo spectrum without ground.

The objective function of extended C-SALSA requires that the objective vector of each virtual ULAs is the same, which is a quite strictly constraints. Appendix C shows that strong reflection points relative to each virtual array can be quite different. These different reflection points could be significantly suppressed by the extended C-SALSA.

## 5.4. Conclusions

CRLBs of the DOA and range in different configurations indicate that both azimuth and range resolutions can be improved by using multiple MIMOs. The multi-static configuration can achieve better azimuth resolution than that of the mono-static configuration since it employs extra information of multi-static combinations. The possible estimation accuracy of both DOA and range increase when the signal bandwidth, the inter-MIMO spacing, the number of elements per virtual array, or the number of MIMOs increases. The CRLB of range is more dependent on the signal bandwidth, while the CRLB of DOA is more sensitive to the change of the inter-MIMO spacing. Moreover, from the perspective of information theory, the estimation accuracy increases as the amount of uncorrelated information increases.

Both the generalized 2D-MUSIC algorithm and extended C-SALSA can provide better azimuth and range resolutions compared to the traditional Rayleigh resolutions. In mono-static configuration, azimuth resolution of the extended C-SALSA is better than the generalized 2D-MUSIC. However, the performance of extended C-SALSA drops if targets are too close. A possible reason is that the data-based method is less robust with few samples in spatial dimension, while MUSIC-based algorithm still can work thanks to the fact that it exploits the orthogonality between signal and noise subspaces. Moreover, the performance of extended C-SALSA can be more stable with more sensors in each MIMO.

Extended targets may have different strong reflection points relative to different virtual arrays in the system. However, both proposed algorithms assume that every MIMO can observe the same targets. Consequently, if a reflection point cannot be seen by all virtual arrays, it might be demonstrated as a weak target or totally missing in the estimation result. Moreover, both algorithms have limitations for extended targets, but the generalized 2D-MUSIC provides a better profile of the simulated vehicle in EM simulation results.



# 6

## Conclusions and Future Work

This chapter will summarize outcomes of this work and provide suggestions for further investigation. Section 6.1 summarizes achievements based on results and novelties, and Section 6.2 provides suggestions for future work.

### 6.1. Results and Novelties

This work addressed the low azimuth resolution problem of a single MIMO. In this thesis, we proposed a novel topology of array, which consists of multiple coherent FMCW MIMOs. These MIMOs are arranged along the azimuth dimension to improve azimuth resolution by extending the effective aperture size. Then signal models for multi-static and mono-static configurations of the radar system are formulated with FMCW waveform. To the best of our knowledge, target localization by jointly using multiple coherent MIMOs has not been reported yet. To this end, we have investigated and tested two algorithms to localize targets with super-high resolutions using multiple MIMOs. One is a subspace-based algorithm and the other one is a sparsity-based method.

The subspace-based algorithm is named as generalized 2D-MUSIC algorithm, which exploits the orthogonality of signal and noise subspaces. Geometrical constraints of the system are maintained by using the same search grid to all virtual arrays, consequently, data association is avoided. We are the first one to generalize 2D-MUSIC to multiple MIMOs. 2D-MUSIC is applied to each virtual array locally, and their estimation re-

sults are connected through the same search grid. The performance of this method is summarized as follows.

1. This algorithm is applicable for both multi-static and mono-static configurations of the radar system.
2. The estimation accuracy of this algorithm is close to CRLB with applying extremely fine search grid. In practice, the grid-based error can be suppressed by applying an iterative grid refinement method.
3. Azimuth resolution is improved by using multiple MIMOs. Moreover, azimuth resolution of the multi-static configuration is better than that of the mono-static configuration since the first one uses extra information of multi-static combinations.
4. This method has limitations for estimating extended targets, but it still provided a better profile of the simulated target compared with extended C-SALSA in EM simulation results.
5. This method suffers from high correlated signals, therefore, the FBSS technique is required to decorrelate back-scattered signals.
6. This method requires the number of targets as prior knowledge to separate signal and noise subspace. The performance could significantly drop if the model order is incorrectly estimated.

To avoid pre-estimating the number of targets, we proposed the extended C-SALSA to tackle localization problems. It is worth noting that we are the first to cast the target localization problem as a constrained sparse representation problem. Instead of estimating targets' locations, this method focuses on sparse spectrum estimation. Geometrical constraints of the system are remained by applying the same overcomplete dictionary to all virtual arrays, thus data association is avoided. The performance of this method is summarized as follows.

1. This method can estimate the number of point targets as a side benefit.
2. Compared with the generalized 2D-MUSIC algorithm, this method can achieve better azimuth resolution in the mono-static configuration of a radar system.
3. This method has limitations for estimating extended targets, because the objective function strictly requires that each MIMO should observe the same targets.

However, strong reflection points of the extended target to each MIMO could be different.

4. This method suffers from off-grid problems, is sensitive to optimization parameters, and requires moderate SNR.

## 6.2. Recommendations for Future Work

Based on this work, several recommendations for future work are provided as follows. The first two suggestions are from algorithms perspective, and the last one is from the system model perspective.

- The objective function of extended C-SALSA requires that the objective vector of each MIMO should be the same, which is a quite strict constraint. Future work can relax the objective function in (4.13) to a joint sparsity constraint using  $l_{2,1}$  norm, as

$$\begin{aligned} & \underset{\mathbf{S}}{\text{minimize}} && \|\mathbf{S}\|_{2,1} \\ & \text{subject to} && \left\{ \begin{array}{l} \|\tilde{\mathbf{B}}_{-M}\tilde{\mathbf{s}}_{-M} - \mathbf{x}_{-M}\|_2 \leq \epsilon_{-M} \\ \vdots \\ \|\tilde{\mathbf{B}}_M\tilde{\mathbf{s}}_M - \mathbf{x}_M\|_2 \leq \epsilon_M \\ \mathbf{S} = [\tilde{\mathbf{s}}_{-M}; \dots; \tilde{\mathbf{s}}_M] \end{array} \right. \end{aligned} \quad (6.1)$$

- The extended C-SALSA is a data-based sparse optimization method, which suffers from off-grid problems and is sensitive to noise. We recommend to use robust KronPCA proposed in [44] to achieve gridless 2D target localization.

Analyzing covariance matrices, we have

$$\begin{aligned} \mathbf{R}_m &= E[\mathbf{x}_m \mathbf{x}_m^H] \\ &= \mathbf{\Theta}_m + \mathbf{\Gamma}_m \end{aligned} \quad (6.2)$$

Then, the information of targets' positions can be estimated by combining low rank and sparsity as objective function. Since rank function is hard to solve, nuclear norm can be used to penalize low rank matrix approximation.  $l_1$  norm regularization function is applied to penalize sparsity. Moreover, the term  $\|\mathbf{R}_m - \mathbf{\Theta}_m - \mathbf{\Gamma}_m\|_F^2$  is introduced to relax the exact constraint of (6.2), where  $\|\cdot\|_F$  is the Frobenius norm. Then the optimization procedure is

$$\begin{aligned}
& \text{minimize} && \sum_{m=-M}^M (\|\mathbf{R}_m - \Theta_m - \Gamma_m\|_F^2 + \lambda_{\Theta_m} \|\mathcal{R}(\Theta_m)\|_* + \lambda_{\Gamma_m} \|\Gamma_m\|_1) \\
& \text{subject to} && \left\{ \begin{array}{l} \Theta_m = \sum_{k=1}^K \gamma_k^2 \cdot \mathbf{C}_m^{(k)} \otimes \mathbf{D}_m^{(k)} \\ \mathbf{C}_m^{(k)} = \mathbf{b}_m^{(r)}(r_k^{(m)}) \left( \mathbf{b}_m^{(r)}(r_k^{(m)}) \right)^H \\ \mathbf{D}_m^{(k)} = \mathbf{b}_m^{(\theta)}(\theta_k^{(m)}) \left( \mathbf{b}_m^{(\theta)}(\theta_k^{(m)}) \right)^H \\ r_k^{(m)} = f(r_k, \theta_k, m) \\ \theta_k^{(m)} = g(r_k, \theta_k, m) \\ \Gamma_m = \sigma_m^2 \mathbf{I} \end{array} \right.
\end{aligned} \tag{6.3}$$

where  $m$  and  $k$  represent the indices of the MIMOs and the targets, respectively.  $\gamma_k$  is the reflectivity's amplitude of the  $k^{\text{th}}$  target.  $(r_k, \theta_k)$  is the position of the  $k^{\text{th}}$  target relative to the reference MIMO of the system.  $\mathbf{b}_m^{(r)}(r_k^{(m)})$  and  $\mathbf{b}_m^{(\theta)}(\theta_k^{(m)})$  are the range and DOA steering vectors of the  $k^{\text{th}}$  target relative to the  $m^{\text{th}}$  MIMO which are defined in (4.4) and (4.5), respectively.  $\sigma_m^2$  is the noise variance of the  $m^{\text{th}}$  MIMO.  $\mathbf{C}_m^{(k)}$  and  $\mathbf{D}_m^{(k)}$  are two positive semi-definite Hermitian Toeplitz matrices, thus their Kronecker product  $\Theta_m \in \mathbb{C}^{NP \times NP}$  is a positive semi-definite Toeplitz-block-Toeplitz matrix [45].  $\|\mathcal{R}(\Theta_m)\|_*$  is the rearranged nuclear norm of  $\Theta_m$ , which is a low rank matrix, where  $\mathcal{R}(\cdot)$  is the invertible rearrangement operator [46].  $\Gamma_m \in \mathbb{C}^{NP \times NP}$  is a sparse matrix. The regularization parameters  $\lambda_{\Theta_m} > 0$  and  $\lambda_{\Gamma_m} > 0$  control the importance between low rank and sparsity, respectively, where increasing either increases the percentage of regularization. Moreover, the geometrical relationship between  $(r_k^{(m)}, \theta_k^{(m)})$  and  $(r_k, \theta_k)$  is formulated as follows.

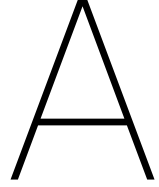
$$f(r_k, \theta_k, m) = \sqrt{r_k^2 + (md_s)^2 - 2r_k md_s \sin(\theta_k)} \tag{6.4}$$

$$g(r_k, \theta_k, m) = \arcsin \left( (r_k \sin(\theta_k) - md_s)(r_k^{(m)})^{-1} \right) \tag{6.5}$$

- The system model proposed in this project focuses on 2D target localization. Under the assumption that the radar system is well-synchronized, it is recommended to place MIMOs in different height, then elevation information can be obtained from the phase difference among MIMOs in multi-static combinations.

# Appendices





## Cramer-Rao Lower Bound for the Multi-static Configuration of the System

As shown in Figure 2.1, the system consists of  $(2M + 1)$  MIMOs in total. Suppose that a point target locates in the near-field of the system, but in the far-field of each MIMO. Then, we can assume that the DOD is approximately same as the DOA for the target relative to each MIMO. The middle point between the  $N_{Tx}^{th}$  transmitter and the  $1^{th}$  receiver is selected to calculate the range and DOD/DOA relative to each MIMO. Assume the target location is  $(r, \theta)$  relative to the reference MIMO of the radar system, then from (2.5) and (2.6), we can get its position relative to each MIMO as

$$r^{(m)} = \sqrt{r^2 + (md_s)^2 - 2rmd_s \sin \theta} \quad (\text{A.1})$$

$$\psi^{(m)} = \theta^{(m)} = \arcsin \left( \frac{r \sin \theta - md_s}{r^{(m)}} \right) \quad (\text{A.2})$$

where  $m = -M, \dots, M$ ,  $r^{(m)}$  is the relative distance between the target and the  $m^{th}$  MIMO,  $\psi^{(m)}$  and  $\theta^{(m)}$  are the DOD and DOA for the target relative to the  $m^{th}$  MIMO, respectively.  $d_s$  is the spacing between two adjacent MIMOs.

Assume signals are transmitted from the  $m_1^{th}$  MIMO, then the scattered signals, from the point target, are received by the  $m_2^{th}$  MIMO. From (2.15), the received signals after dechirp, in a sweep duration, can be written as

$$x_{m_1, m_2}[aN_{Rx} + b, n] = s_{m_1, m_2}[aN_{Rx} + b, n] + w_{m_1, m_2}[aN_{Rx} + b, n] \quad (\text{A.3})$$

where

$$\begin{aligned}
s_{m_1, m_2}[aN_{Rx} + b, n] &= \gamma e^{j\phi} \exp \left[ j2\pi \left( \mu \tau^{(m_1, m_2)} \frac{n}{f_s} - f_0 \tau^{(m_1, m_2)} \right. \right. \\
&\quad \left. \left. - \frac{1}{2} \mu (\tau^{(m_1, m_2)})^2 + f_0 \frac{ad_{Tx} \sin(\psi^{(m_1)})}{c} \right. \right. \\
&\quad \left. \left. + f_0 \frac{bd_{Rx} \sin(\theta^{(m_2)})}{c} \right) \right] \\
&= \gamma \exp \left[ j \left( \phi - 2\pi f_0 \tau^{(m_1, m_2)} - \pi \mu (\tau^{(m_1, m_2)})^2 \right) \right. \\
&\quad \left. + j2\pi \left( \mu \tau^{(m_1, m_2)} \frac{n}{f_s} + f_0 \frac{ad_{Tx} \sin(\psi^{(m_1)})}{c} \right. \right. \\
&\quad \left. \left. + f_0 \frac{bd_{Rx} \sin(\theta^{(m_2)})}{c} \right) \right] \tag{A.4} \\
&= \gamma \exp \left[ j\Phi_{m_1, m_1} + j2\pi \left( \mu \tau^{(m_1, m_2)} \frac{n}{f_s} \right. \right. \\
&\quad \left. \left. + f_0 \frac{ad_{Tx} \sin(\psi^{(m_1)})}{c} + f_0 \frac{bd_{Rx} \sin(\theta^{(m_2)})}{c} \right) \right]
\end{aligned}$$

$\gamma e^{j\phi}$  represents the reflectivity of the target.  $\mu$  is the rate of frequency change,  $\mu = B/T_s$ ,  $B$  is sweep bandwidth,  $T_s$  is sweep duration.  $\tau^{(m_1, m_2)}$  represents the time delay corresponding to the path from the  $m_1^{th}$  MIMO to the  $m_2^{th}$  MIMO through the point target.  $f_s$  is ADC sampling rate,  $f_0$  is initial frequency,  $d_{Tx}$  and  $d_{Rx}$  are the inter-element spacing of transmitters and receivers, respectively.  $N_{Tx}$  and  $N_{Rx}$  represent the number of transmitters and receivers, respectively.  $c$  is the speed of light,  $\{m_1, m_2\} \in \{-M, \dots, M\}$ ,  $a = -(N_{Tx} - 1), \dots, 0$ ,  $b = 0, \dots, N_{Rx} - 1$ ,  $n = 0, 1, \dots, N - 1$ , and

$$\tau^{(m_1, m_2)} = \frac{r^{(m_1)} + r^{(m_2)}}{c} \tag{A.5}$$

$$r^{(m_1)} = \sqrt{r^2 + (m_1 d_s)^2 - 2r m_1 d_s \sin \theta} \tag{A.6}$$

$$r^{(m_2)} = \sqrt{r^2 + (m_2 d_s)^2 - 2r m_2 d_s \sin \theta} \tag{A.7}$$

$$\sin(\psi^{(m_1)}) = \sin(\theta^{(m_1)}) = \frac{r \sin \theta - m_1 d_s}{r^{(m_1)}} \tag{A.8}$$

$$\sin(\psi^{(m_2)}) = \sin(\theta^{(m_2)}) = \frac{r \sin \theta - m_2 d_s}{r^{(m_2)}} \tag{A.9}$$

$$\Phi_{m_1, m_2} = \phi - 2\pi f_0 \tau^{(m_1, m_2)} - \pi \mu (\tau^{(m_1, m_2)})^2 \tag{A.10}$$

Collect all received signals together, we have

$$\begin{bmatrix} x_{-M,-M}[aN_{Rx} + b, n] \\ \vdots \\ x_{m_1, m_2}[aN_{Rx} + b, n] \\ \vdots \\ x_{M,M}[aN_{Rx} + b, n] \end{bmatrix} = \begin{bmatrix} s_{-M,-M}[aN_{Rx} + b, n] \\ \vdots \\ s_{m_1, m_2}[aN_{Rx} + b, n] \\ \vdots \\ s_{M,M}[aN_{Rx} + b, n] \end{bmatrix} + \begin{bmatrix} w_{-M,-M}[aN_{Rx} + b, n] \\ \vdots \\ w_{m_1, m_2}[aN_{Rx} + b, n] \\ \vdots \\ w_{M,M}[aN_{Rx} + b, n] \end{bmatrix} \quad (\text{A.11})$$

Therefore, we can express the noisy discretized received signal of the radar system as

$$x[aN_{Rx} + b + l, n] = s[aN_{Rx} + b + l, n] + w[aN_{Rx} + b + l, n] \quad (\text{A.12})$$

where  $l = (m_1 + M)(2M + 1)P + (m_2 + M)P$ ,  $PN_{Tx}N_{Rx}$  represents the total number of channels of each virtual array, and  $w[aN_{Rx} + b + l, n] \sim \mathcal{CN}(0, \sigma^2)$  is complex AWGN.

The signal to noise ratio (SNR) is defined as

$$\text{SNR} = \frac{\gamma^2}{\sigma^2} \quad (\text{A.13})$$

The likelihood function [43] of the noisy received signal is

$$\begin{aligned} p(\mathbf{x}; \boldsymbol{\Omega}) = \exp \left[ -\frac{1}{\sigma^2} \sum_{n=0}^{N-1} \sum_{a=1-N_{Tx}}^0 \sum_{b=0}^{N_{Rx}-1} \sum_{m_1=-M}^M \sum_{m_2=-M}^M w_{m_1, m_2}[aN_{Rx} + b, n] \right. \\ \left. \cdot w_{m_1, m_2}^*[aN_{Rx} + b, n] \right] \cdot \frac{1}{(\pi\sigma^2)^{(2M+1)^2NP}} \end{aligned} \quad (\text{A.14})$$

where

$$\boldsymbol{\Omega} = [\Omega_1, \Omega_2, \Omega_3, \Omega_4]^T = [\gamma, \Phi_{m_1, m_2}, r, \theta]^T \quad (\text{A.15})$$

$$w_{m_1, m_2}[aN_{Rx} + b, n] = x_{m_1, m_2}[aN_{Rx} + b, n] - s_{m_1, m_2}[aN_{Rx} + b, n] \quad (\text{A.16})$$

Then the log-likelihood function is

$$\begin{aligned} \ln p(\mathbf{x}; \boldsymbol{\Omega}) = -\ln (\pi\sigma^2)^{(2M+1)^2NP} \\ -\frac{1}{\sigma^2} \sum_{n=0}^{N-1} \sum_{a=1-N_{Tx}}^0 \sum_{b=0}^{N_{Rx}-1} \sum_{m_1=-M}^M \sum_{m_2=-M}^M w_{m_1, m_2}[aN_{Rx} + b, n] \\ \cdot w_{m_1, m_2}^*[aN_{Rx} + b, n] \end{aligned} \quad (\text{A.17})$$

The first derivative of the log-likelihood function with respect to  $\Omega_i$  produces

$$\begin{aligned} \frac{\partial \ln p(\mathbf{x}; \boldsymbol{\Omega})}{\partial \Omega_i} &= \frac{1}{\sigma^2} \sum_{n=0}^{N-1} \sum_{a=1-N_{Tx}}^0 \sum_{b=0}^{N_{Rx}-1} \sum_{m_1=-M}^M \sum_{m_2=-M}^M \left[ \frac{\partial s_{m_1, m_2}[aN_{Rx} + b, n]}{\partial \Omega_i} \right. \\ &\quad \cdot w_{m_1, m_2}^*[aN_{Rx} + b, n] + w_{m_1, m_2}[aN_{Rx} + b, n] \\ &\quad \left. \cdot \frac{\partial s_{m_1, m_2}^*[aN_{Rx} + b, n]}{\partial \Omega_i} \right] \end{aligned} \quad (\text{A.18})$$

and the second derivative with respect to  $\Omega_j$  is

$$\begin{aligned} \frac{\partial^2 \ln p(\mathbf{x}; \boldsymbol{\Omega})}{\partial \Omega_i \partial \Omega_j} &= \frac{1}{\sigma^2} \sum_{n=0}^{N-1} \sum_{a=1-N_{Tx}}^0 \sum_{b=0}^{N_{Rx}-1} \sum_{m_1=-M}^M \sum_{m_2=-M}^M \left[ \frac{\partial^2 s_{m_1, m_2}[aN_{Rx} + b, n]}{\partial \Omega_i \partial \Omega_j} \right. \\ &\quad \cdot w_{m_1, m_2}^*[aN_{Rx} + b, n] - \frac{\partial s_{m_1, m_2}[aN_{Rx} + b, n]}{\partial \Omega_i} \\ &\quad \cdot \frac{\partial s_{m_1, m_2}^*[aN_{Rx} + b, n]}{\partial \Omega_j} - \frac{\partial s_{m_1, m_2}[aN_{Rx} + b, n]}{\partial \Omega_j} \\ &\quad \cdot \frac{\partial s_{m_1, m_2}^*[aN_{Rx} + b, n]}{\partial \Omega_i} + w_{m_1, m_2}[aN_{Rx} + b, n] \\ &\quad \left. \cdot \frac{\partial^2 s_{m_1, m_2}^*[aN_{Rx} + b, n]}{\partial \Omega_i \partial \Omega_j} \right] \end{aligned} \quad (\text{A.19})$$

The Fisher information matrix,  $\mathbf{I}(\boldsymbol{\Omega})$ , is [42]

$$\begin{aligned} [\mathbf{I}(\boldsymbol{\Omega})]_{i,j} &= - E \left[ \frac{\partial^2 \ln p(\mathbf{x}; \boldsymbol{\Omega})}{\partial \Omega_i \partial \Omega_j} \right] \\ &= \frac{1}{\sigma^2} \sum_{n=0}^{N-1} \sum_{a=1-N_{Tx}}^0 \sum_{b=0}^{N_{Rx}-1} \sum_{m_1=-M}^M \sum_{m_2=-M}^M \left[ \frac{\partial s_{m_1, m_2}[aN_{Rx} + b, n]}{\partial \Omega_i} \right. \\ &\quad \cdot \frac{\partial s_{m_1, m_2}^*[aN_{Rx} + b, n]}{\partial \Omega_j} + \frac{\partial s_{m_1, m_2}[aN_{Rx} + b, n]}{\partial \Omega_j} \\ &\quad \left. \cdot \frac{\partial s_{m_1, m_2}^*[aN_{Rx} + b, n]}{\partial \Omega_i} \right] \\ &= \frac{2}{\sigma^2} \sum_{n=0}^{N-1} \sum_{a=1-N_{Tx}}^0 \sum_{b=0}^{N_{Rx}-1} \sum_{m_1=-M}^M \sum_{m_2=-M}^M \left[ \frac{\partial u_{m_1, m_2}[aN_{Rx} + b, n]}{\partial \Omega_i} \right. \\ &\quad \cdot \frac{\partial u_{m_1, m_2}[aN_{Rx} + b, n]}{\partial \Omega_j} + \frac{\partial v_{m_1, m_2}[aN_{Rx} + b, n]}{\partial \Omega_i} \\ &\quad \left. \cdot \frac{\partial v_{m_1, m_2}[aN_{Rx} + b, n]}{\partial \Omega_j} \right] \end{aligned} \quad (\text{A.20})$$

where

$$u_{m_1, m_2}[aN_{Rx} + b, n] = \text{Re}\{s_{m_1, m_2}[aN_{Rx} + b, n]\} \quad (\text{A.21})$$

$$v_{m_1, m_2}[aN_{Rx} + b, n] = \text{Im}\{s_{m_1, m_2}[aN_{Rx} + b, n]\} \quad (\text{A.22})$$

Assume

$$h_{m_1, m_2}[aN_{Rx} + b, n] = \Phi_{m_1, m_2} + 2\pi \left( \mu \tau^{(m_1, m_2)} \frac{n}{f_s} + f_0 \frac{ad_{Tx} \sin(\psi^{(m_1)})}{c} + f_0 \frac{bd_{Rx} \sin(\theta^{(m_2)})}{c} \right) \quad (\text{A.23})$$

then we have

$$u_{m_1, m_2}[aN_{Rx} + b, n] = \gamma \cos(h_{m_1, m_2}[aN_{Rx} + b, n]) \quad (\text{A.24})$$

$$v_{m_1, m_2}[aN_{Rx} + b, n] = \gamma \sin(h_{m_1, m_2}[aN_{Rx} + b, n]) \quad (\text{A.25})$$

$$\frac{\partial u_{m_1, m_2}[aN_{Rx} + b, n]}{\partial \Omega_1} = \cos(h_{m_1, m_2}[aN_{Rx} + b, n]) \quad (\text{A.26})$$

$$\frac{\partial u_{m_1, m_2}[aN_{Rx} + b, n]}{\partial \Omega_2} = -\gamma \sin(h_{m_1, m_2}[aN_{Rx} + b, n]) \quad (\text{A.27})$$

$$\begin{aligned} \frac{\partial u_{m_1, m_2}[aN_{Rx} + b, n]}{\partial \Omega_3} = & -2\pi\gamma \left( \frac{\mu}{c} \frac{n}{f_s} (\xi_1 + \xi_5) + \frac{f_0}{c} d_{Tx} \xi_2 a \right. \\ & \left. + \frac{f_0}{c} d_{Rx} \xi_6 b \right) \sin(h_{m_1, m_2}[aN_{Rx} + b, n]) \end{aligned} \quad (\text{A.28})$$

$$\begin{aligned} \frac{\partial u_{m_1, m_2}[aN_{Rx} + b, n]}{\partial \Omega_4} = & -2\pi\gamma \left( \frac{\mu}{c} \frac{n}{f_s} (\xi_3 + \xi_7) + \frac{f_0}{c} d_{Tx} \xi_4 a \right. \\ & \left. + \frac{f_0}{c} d_{Rx} \xi_8 b \right) \sin(h_{m_1, m_2}[aN_{Rx} + b, n]) \end{aligned} \quad (\text{A.29})$$

$$\frac{\partial v_{m_1, m_2}[aN_{Rx} + b, n]}{\partial \Omega_1} = \sin(h_{m_1, m_2}[aN_{Rx} + b, n]) \quad (\text{A.30})$$

$$\frac{\partial v_{m_1, m_2}[aN_{Rx} + b, n]}{\partial \Omega_2} = \gamma \cos(h_{m_1, m_2}[aN_{Rx} + b, n]) \quad (\text{A.31})$$

$$\begin{aligned} \frac{\partial v_{m_1, m_2}[aN_{Rx} + b, n]}{\partial \Omega_3} = & 2\pi\gamma \left( \frac{\mu}{c} \frac{n}{f_s} (\xi_1 + \xi_5) + \frac{f_0}{c} d_{Tx} \xi_2 a \right. \\ & \left. + \frac{f_0}{c} d_{Rx} \xi_6 b \right) \cos(h_{m_1, m_2}[aN_{Rx} + b, n]) \end{aligned} \quad (\text{A.32})$$

$$\begin{aligned} \frac{\partial v_{m_1, m_2}[aN_{Rx} + b, n]}{\partial \Omega_4} = & 2\pi\gamma \left( \frac{\mu}{c} \frac{n}{f_s} (\xi_3 + \xi_7) + \frac{f_0}{c} d_{Tx} \xi_4 a \right. \\ & \left. + \frac{f_0}{c} d_{Rx} \xi_8 b \right) \cos(h_{m_1, m_2}[aN_{Rx} + b, n]) \end{aligned} \quad (\text{A.33})$$

where

$$\xi_1 = \frac{r - m_1 d_s \sin \theta}{r^{(m_1)}} \quad (\text{A.34})$$

$$\xi_2 = \frac{r^{(m_1)} \sin \theta - (r \sin \theta - m_1 d_s) \xi_1}{(r^{(m_1)})^2} \quad (\text{A.35})$$

$$\xi_3 = -\frac{r m_1 d_s \cos \theta}{r^{(m_1)}} \quad (\text{A.36})$$

$$\xi_4 = \frac{r^{(m_1)} r \cos \theta - (r \sin \theta - m_1 d_s) \xi_3}{(r^{(m_1)})^2} \quad (\text{A.37})$$

$$\xi_5 = \frac{r - m_2 d_s \sin \theta}{r^{(m_2)}} \quad (\text{A.38})$$

$$\xi_6 = \frac{r^{(m_2)} \sin \theta - (r \sin \theta - m_2 d_s) \xi_5}{(r^{(m_2)})^2} \quad (\text{A.39})$$

$$\xi_7 = -\frac{r m_2 d_s \cos \theta}{r^{(m_2)}} \quad (\text{A.40})$$

$$\xi_8 = \frac{r^{(m_2)} r \cos \theta - (r \sin \theta - m_2 d_s) \xi_7}{(r^{(m_2)})^2} \quad (\text{A.41})$$

Therefore,

$$\mathbf{I}(\boldsymbol{\Omega}) = \frac{2}{\sigma^2} \sum_{n=0}^{N-1} \sum_{a=1-N_{Tx}}^0 \sum_{b=0}^{N_{Rx}-1} \sum_{m_1=-M}^M \sum_{m_2=-M}^M \begin{bmatrix} i_{1,1} & 0 & 0 & 0 \\ 0 & i_{2,2} & i_{2,3} & i_{2,4} \\ 0 & i_{3,2} & i_{3,3} & i_{3,4} \\ 0 & i_{4,2} & i_{4,3} & i_{4,4} \end{bmatrix} \quad (\text{A.42})$$

where

$$i_{1,1} = 1 \quad (\text{A.43})$$

$$i_{2,2} = \gamma^2 \quad (\text{A.44})$$

$$i_{2,3} = i_{3,2} = 2\pi\gamma^2 \left( \frac{\mu}{c} \frac{1}{f_s} (\xi_1 + \xi_5) n + \frac{f_0}{c} d_{Tx} \xi_2 a + \frac{f_0}{c} d_{Rx} \xi_6 b \right) \quad (\text{A.45})$$

$$i_{2,4} = i_{4,2} = 2\pi\gamma^2 \left( \frac{\mu}{c} \frac{1}{f_s} (\xi_3 + \xi_7) n + \frac{f_0}{c} d_{Tx} \xi_4 a + \frac{f_0}{c} d_{Rx} \xi_8 b \right) \quad (\text{A.46})$$

$$\begin{aligned}
i_{3,3} = & (2\pi\gamma)^2 \left\{ \left[ \frac{\mu}{c} \frac{1}{f_s} (\xi_1 + \xi_5) \right]^2 n^2 + \left( \frac{f_0}{c} d_{Tx} \xi_2 \right)^2 a^2 \right. \\
& + \left( \frac{f_0}{c} d_{Rx} \xi_6 \right)^2 b^2 + 2 \left( \frac{f_0}{c} \right)^2 d_{Tx} d_{Rx} \xi_2 \xi_6 ab \\
& \left. + 2 \frac{\mu}{c} \frac{1}{f_s} \frac{f_0}{c} (\xi_1 + \xi_5) (d_{Tx} \xi_2 a + d_{Rx} \xi_6 b) n \right\} \quad (A.47)
\end{aligned}$$

$$\begin{aligned}
i_{3,4} = i_{4,3} = & (2\pi\gamma)^2 \left\{ \left( \frac{\mu}{c} \frac{1}{f_s} \right)^2 (\xi_1 + \xi_5) (\xi_3 + \xi_7) n^2 + \frac{\mu}{c} \frac{1}{f_s} \frac{f_0}{c} d_{Tx} [(\xi_1 + \xi_5) \xi_4 \right. \\
& + (\xi_3 + \xi_7) \xi_2] an + \frac{\mu}{c} \frac{1}{f_s} \frac{f_0}{c} d_{Rx} [(\xi_1 + \xi_5) \xi_8 + (\xi_3 + \xi_7) \xi_6] bn \\
& \left. + \left( \frac{f_0}{c} \right)^2 [d_{Tx}^2 \xi_2 \xi_4 a^2 + d_{Rx}^2 \xi_6 \xi_8 b^2 + d_{Tx} d_{Rx} (\xi_2 \xi_8 + \xi_4 \xi_6) ab] \right\} \quad (A.48)
\end{aligned}$$

$$\begin{aligned}
i_{4,4} = & (2\pi\gamma)^2 \left\{ \left[ \frac{\mu}{c} \frac{1}{f_s} (\xi_3 + \xi_7) \right]^2 n^2 + \left( \frac{f_0}{c} d_{Tx} \xi_4 \right)^2 a^2 \right. \\
& + \left( \frac{f_0}{c} d_{Rx} \xi_8 \right)^2 b^2 + 2 \left( \frac{f_0}{c} \right)^2 d_{Tx} d_{Rx} \xi_4 \xi_8 ab \\
& \left. + 2 \frac{\mu}{c} \frac{1}{f_s} \frac{f_0}{c} (\xi_3 + \xi_7) (d_{Tx} \xi_4 a + d_{Rx} \xi_8 b) n \right\} \quad (A.49)
\end{aligned}$$

Then we can get the CRLB of range and DOA as

$$\sigma_{CRLB}^{(r)} = \sqrt{[\mathbf{I}^{-1}(\boldsymbol{\Omega})]_{3,3}} \quad \text{and} \quad \sigma_{CRLB}^{(\theta)} = \sqrt{[\mathbf{I}^{-1}(\boldsymbol{\Omega})]_{4,4}} \quad (A.50)$$

where the unit of  $\sigma_{CRLB}^{(\theta)}$  is radian.



# B

## Chirp Spectrum

For simplicity, assume  $A_0 = 1$  and  $\phi_0 = 0$  in (2.7), then we can write the LFM signal in time domain as:

$$\begin{aligned} s_{Tx}(t) &= \exp \left[ j2\pi \left( f_0 - \frac{1}{2} \frac{B}{T_s} t \right) t \right] \quad 0 \leq t < T_s \\ &= \exp \left[ j \left( \omega_0 t - \frac{1}{2} \frac{\Delta\Omega}{T_s} t^2 \right) \right] \end{aligned} \quad (\text{B.1})$$

where  $f_0$  is initial frequency,  $B$  is sweep bandwidth,  $T_s$  is sweep duration,  $0 \leq t < T_s$ ,  $\omega_0 = 2\pi f_0$  and  $\Delta\Omega = 2\pi B$ .

The spectrum of this signal can be calculated as

$$\begin{aligned} S(\omega) &= \int_0^{T_s} \exp \left[ j \left( \omega_0 t - \frac{\Delta\Omega}{2T_s} t^2 \right) \right] \exp(-j\omega t) dt \\ &= \int_0^{T_s} \exp \left[ j \left( (\omega_0 - \omega) t - \frac{\Delta\Omega}{2T_s} t^2 \right) \right] dt \end{aligned} \quad (\text{B.2})$$

Completing the square of the above equation, we have

$$\begin{aligned}
S(\omega) &= \int_0^{T_s} \exp \left[ j \left( -\frac{\Delta\Omega}{2T_s} \left( t - \frac{(\omega_0 - \omega)T_s}{\Delta\Omega} \right)^2 + \frac{(\omega_0 - \omega)^2 T_s}{2 \cdot \Delta\Omega} \right) \right] dt \\
&= \exp \left[ j \left( (\omega_0 - \omega)^2 \frac{T_s}{2 \cdot \Delta\Omega} \right) \right] \int_0^{T_s} \exp \left[ -j \frac{\Delta\Omega}{2T_s} \left( t - \frac{(\omega_0 - \omega)T_s}{\Delta\Omega} \right)^2 \right] dt \\
&= \sqrt{\frac{2T_s}{\Delta\Omega}} \exp \left[ j \left( (\omega_0 - \omega)^2 \frac{T_s}{2 \cdot \Delta\Omega} \right) \right] \int_{y_0}^{y_1} \exp(-jy^2) dy \\
&= \sqrt{\frac{2T_s}{\Delta\Omega}} \exp \left[ j \left( (\omega_0 - \omega)^2 \frac{T_s}{2 \cdot \Delta\Omega} \right) \right] \cdot G(\omega)
\end{aligned} \tag{B.3}$$

where

$$y = \sqrt{\frac{\Delta\Omega}{2T_s}} \left( t - \frac{(\omega_0 - \omega)T_s}{\Delta\Omega} \right) \tag{B.4}$$

$$G(\omega) = \int_{y_0}^{y_1} \exp(-jy^2) dy \tag{B.5}$$

$$y_0 = -\sqrt{\frac{T_s}{2 \cdot \Delta\Omega}} (\omega_0 - \omega) \tag{B.6}$$

$$y_1 = \sqrt{\frac{T_s}{2 \cdot \Delta\Omega}} (\Delta\Omega - (\omega_0 - \omega)) \tag{B.7}$$

Applying *Euler's formula* to  $G(\omega)$ , then

$$\begin{aligned}
G(\omega) &= \int_{y_0}^{y_1} \cos(y^2) dy - j \int_{y_0}^{y_1} \sin(y^2) dy \\
&= \int_{y_0}^{y_1} \cos \left[ \frac{\pi}{2} \left( \sqrt{\frac{2}{\pi}} \cdot y \right)^2 \right] dy - j \int_{y_0}^{y_1} \sin \left[ \frac{\pi}{2} \left( \sqrt{\frac{2}{\pi}} \cdot y \right)^2 \right] dy \\
&= \sqrt{\frac{\pi}{2}} \left[ \int_{z_0}^{z_1} \cos \left( \frac{\pi}{2} z^2 \right) dz - j \int_{z_0}^{z_1} \sin \left( \frac{\pi}{2} z^2 \right) dz \right]
\end{aligned} \tag{B.8}$$

where

$$z = \sqrt{\frac{2}{\pi}} \cdot y \tag{B.9}$$

$$z_0 = -\frac{(\omega_0 - \omega)}{\sqrt{\frac{\pi \cdot \Delta\Omega}{T_s}}} \tag{B.10}$$

$$z_1 = \frac{\Delta\Omega - (\omega_0 - \omega)}{\sqrt{\frac{\pi \cdot \Delta\Omega}{T_s}}} \tag{B.11}$$

Using the *Fresnel integrals*  $C(Z)$  and  $S(Z)$ ,

$$C(Z) = \int_0^Z \cos\left(\frac{\pi}{2}z^2\right) dz \quad (\text{B.12})$$

$$S(Z) = \int_0^Z \sin\left(\frac{\pi}{2}z^2\right) dz \quad (\text{B.13})$$

the expression of  $G(\omega)$  can be written as:

$$G(\omega) = \sqrt{\frac{\pi}{2}} [C(-z_0) - jS(-z_0) + C(z_1) - jS(z_1)] \quad (\text{B.14})$$

Therefore, the expression of chirp spectrum can be written as:

$$S(\omega) = \sqrt{\frac{\pi T_s}{\Delta\Omega}} \exp\left[j\left((\omega_0 - \omega)^2 \frac{T_s}{2 \cdot \Delta\Omega}\right)\right] \cdot [C(-z_0) - jS(-z_0) + C(z_1) - jS(z_1)] \quad (\text{B.15})$$



# C

## Generalized 2D-MUSIC Results of an Extended Target via EM Simulations

Ground truth of the extended target is shown in Figure 5.11. Actually, the extended target may have different strong reflection points for different virtual arrays. Therefore, individual estimation results of all virtual arrays for both multi-static and mono-static configurations are displayed in this Appendix. Section C.1 and Section C.2 show estimation results by using multi-static/mono-static configuration of the radar system, respectively. For the extended target, 1D-FBSS is employed for both multi-static and mono-static configurations along fast-time dimension. Moreover, the region inside the blue box in each plot approximately indicates size of the extended target from top view.

## C.1. Estimation Results of Multi-static Configuration

Figure C.1 and Figure C.2 display the estimation result of the extended target with/without ground from each virtual array in the multi-static configuration, respectively.

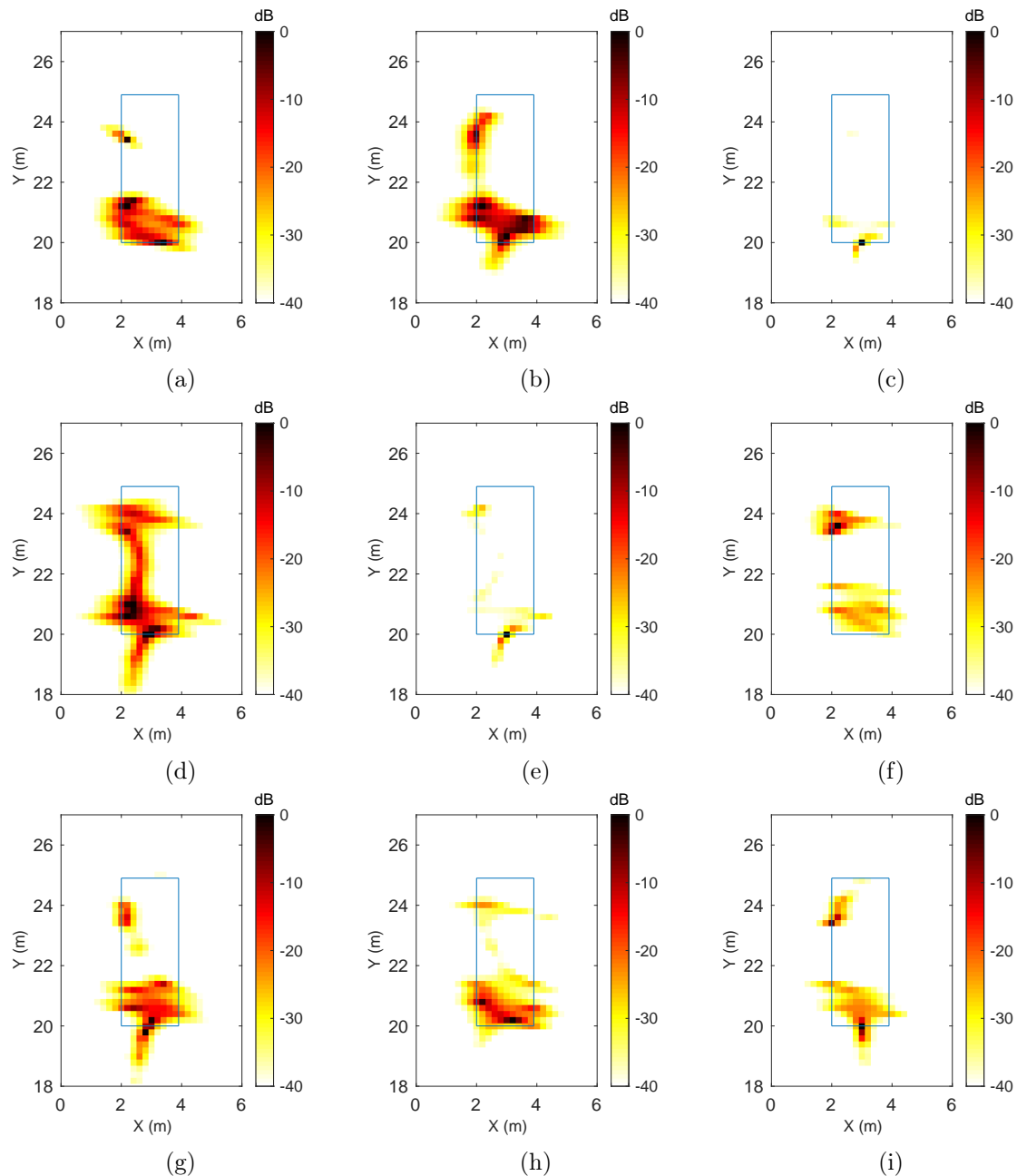


Figure C.1: Estimation result of an extended target with ground by generalized 2D-MUSIC estimator of the multi-static configuration, when signals are transmitted from the  $-1^{th}$  MIMO, and scattered signals are received by: (a) the  $-1^{th}$  MIMO, (b) the  $0^{th}$  MIMO, (c) the  $1^{th}$  MIMO; when signals are transmitted from the  $0^{th}$  MIMO, and scattered signals are received by: (d) the  $-1^{th}$  MIMO, (e) the  $0^{th}$  MIMO, (f) the  $1^{th}$  MIMO; when signals are transmitted from the  $1^{th}$  MIMO, and scattered signals are received by: (g) the  $-1^{th}$  MIMO, (h) the  $0^{th}$  MIMO, (i) the  $1^{th}$  MIMO.

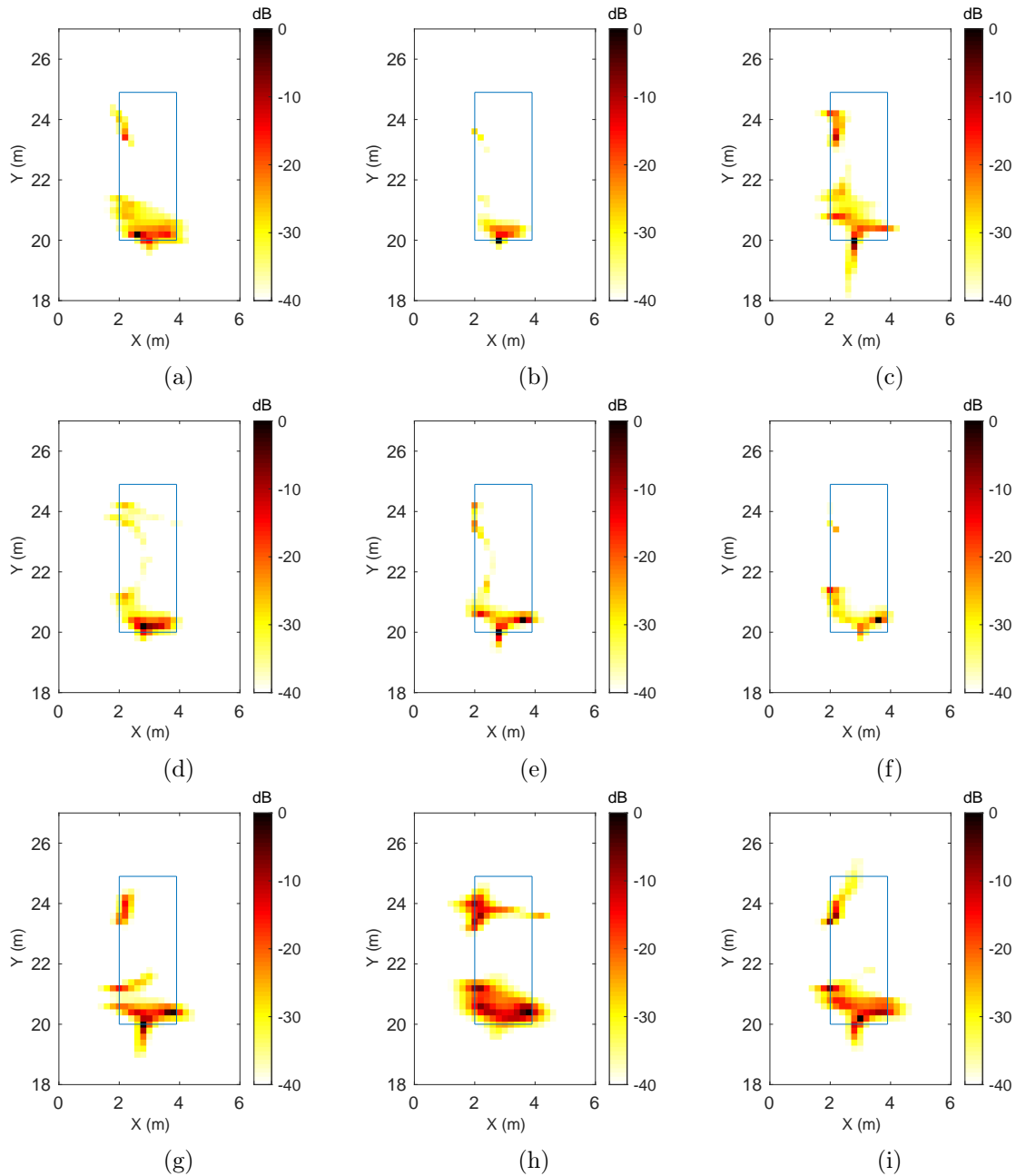


Figure C.2: Estimation result of an extended target without ground by generalized 2D-MUSIC estimator of the multi-static configuration, when signals are transmitted from the  $-1^{th}$  MIMO, and scattered signals are received by: (a) the  $-1^{th}$  MIMO, (b) the  $0^{th}$  MIMO, (c) the  $1^{th}$  MIMO; when signals are transmitted from the  $0^{th}$  MIMO, and scattered signals are received by: (d) the  $-1^{th}$  MIMO, (e) the  $0^{th}$  MIMO, (f) the  $1^{th}$  MIMO; when signals are transmitted from the  $1^{th}$  MIMO, and scattered signals are received by: (g) the  $-1^{th}$  MIMO, (h) the  $0^{th}$  MIMO, (i) the  $1^{th}$  MIMO.

## C.2. Estimation Results of Mono-static Configuration

Figure C.3 and Figure C.4 display the estimation result of the extended target with/without ground from each virtual array in the mono-static configuration, respectively.

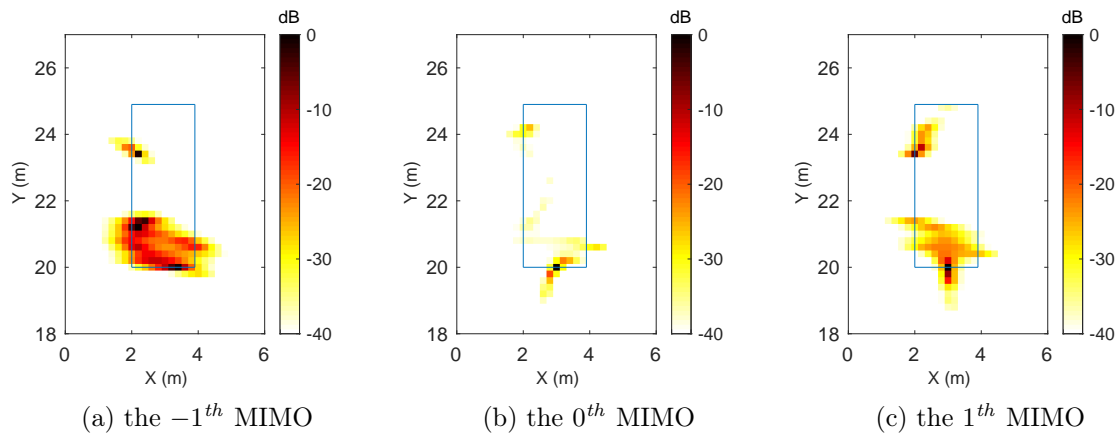


Figure C.3: Estimation result of an extended target with ground by generalized 2D-MUSIC estimator of the mono-static configuration: (a) the  $-1^{th}$  MIMO, (b) the  $0^{th}$  MIMO, (c) the  $1^{th}$  MIMO.

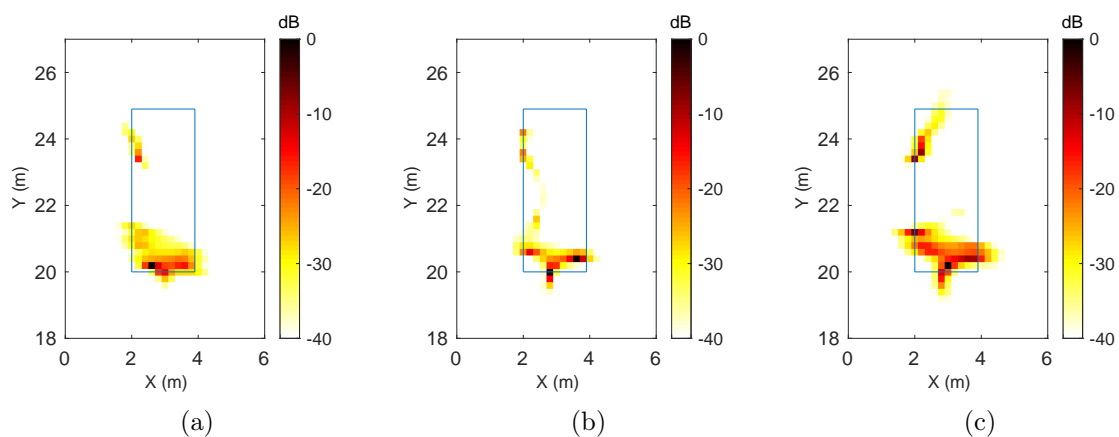


Figure C.4: Estimation result of an extended target without ground by generalized 2D-MUSIC estimator of the mono-static configuration: (a) the  $-1^{th}$  MIMO, (b) the  $0^{th}$  MIMO, (c) the  $1^{th}$  MIMO.

## Bibliography

- [1] I. Shapir, I. Bilik, and G. Barkan, “Doppler ambiguity resolving in tdma automotive mimo radar via digital multiple prf,” in *2018 IEEE Radar Conference (Radar-Conf18)*, April 2018, pp. 0175–0180.
- [2] D. Oh and J. Lee, “Low-complexity range-azimuth fmcw radar sensor using joint angle and delay estimation without svd and evd,” *IEEE Sensors Journal*, vol. 15, no. 9, pp. 4799–4811, Sep. 2015.
- [3] U. Chipengo, P. M. Krenz, and S. Carpenter, “From antenna design to high fidelity, full physics automotive radar sensor corner case simulation,” *Modelling and Simulation in Engineering*, vol. 2018, pp. 1–19, 12 2018.
- [4] H. Krim and M. Viberg, “Two decades of array signal processing research: the parametric approach,” *IEEE Signal Processing Magazine*, vol. 13, no. 4, pp. 67–94, July 1996.
- [5] J. Li and P. Stoica, *MIMO Radar Signal Processing*, ser. Wiley - IEEE. Wiley, 2008. [Online]. Available: <https://books.google.nl/books?id=g6uLLWb-TqYC>
- [6] A. G. Stove, “Linear fmcw radar techniques,” *IEE Proceedings F - Radar and Signal Processing*, vol. 139, no. 5, pp. 343–350, Oct 1992.
- [7] S. Xu, J. Wang, and A. Yarovoy, “Super resolution doa for fmcw automotive radar imaging,” in *2018 IEEE Conference on Antenna Measurements Applications (CAMA)*, Sep. 2018, pp. 1–4.
- [8] F. Belfiori, W. v. Rossum, and P. Hoogeboom, “Coherent music technique for range/angle information retrieval: application to a frequency-modulated continuous wave mimo radar,” *IET Radar, Sonar Navigation*, vol. 8, no. 2, pp. 75–83, February 2014.
- [9] F. Belfiori, W. van Rossum, and P. Hoogeboom, “Application of 2d music algorithm to range-azimuth fmcw radar data,” in *2012 9th European Radar Conference*, Oct 2012, pp. 242–245.

- [10] —, “2d-music technique applied to a coherent fmcw mimo radar,” in *IET International Conference on Radar Systems (Radar 2012)*, Oct 2012, pp. 1–6.
- [11] R. Schmidt, “Multiple emitter location and signal parameter estimation,” 1979.
- [12] S. U. Pillai and B. H. Kwon, “Forward/backward spatial smoothing techniques for coherent signal identification,” *IEEE Transactions on Acoustics, Speech, and Signal Processing*, vol. 37, no. 1, pp. 8–15, Jan 1989.
- [13] S. Kim, Y. Ju, and J. Lee, “A low-complexity joint toas and aoas parameter estimator using dimension reduction for fmcw radar systems,” *Elektronika ir Elektrotechnika*, vol. 24, 08 2018.
- [14] D. G. Oh, Y. H. Ju, and J. H. Lee, “Subspace-based auto-paired range and doa estimation of dual-channel fmcw radar without joint diagonalisation,” *Electronics Letters*, vol. 50, no. 18, pp. 1320–1322, August 2014.
- [15] D. Oh, Y. Ju, H. Nam, and J. Lee, “Dual smoothing doa estimation of two-channel fmcw radar,” *IEEE Transactions on Aerospace and Electronic Systems*, vol. 52, no. 2, pp. 904–917, April 2016.
- [16] S. Kim, D. Oh, and J. Lee, “Joint dft-esprit estimation for toa and doa in vehicle fmcw radars,” *IEEE Antennas and Wireless Propagation Letters*, vol. 14, pp. 1710–1713, 2015.
- [17] M. Wax and T. Kailath, “Decentralized processing in sensor arrays,” *IEEE Transactions on Acoustics, Speech, and Signal Processing*, vol. 33, no. 5, pp. 1123–1129, October 1985.
- [18] D. W. Rieken and D. R. Fuhrmann, “Generalizing music and mvdr for multiple noncoherent arrays,” *IEEE Transactions on Signal Processing*, vol. 52, no. 9, pp. 2396–2406, Sep. 2004.
- [19] F. Wen, Q. Wan, R. Fan, and H. Wei, “Improved music algorithm for multiple noncoherent subarrays,” *IEEE Signal Processing Letters*, vol. 21, no. 5, pp. 527–530, May 2014.
- [20] A. J. Weiss, “Direct position determination of narrowband radio frequency transmitters,” *IEEE Signal Processing Letters*, vol. 11, no. 5, pp. 513–516, May 2004.
- [21] A. Amar and A. J. Weiss, “Direct position determination of multiple radio signals,” in *2004 IEEE International Conference on Acoustics, Speech, and Signal Processing*, vol. 2, May 2004, pp. ii–81.

- [22] T. Tirer and A. J. Weiss, “High resolution direct position determination of radio frequency sources,” *IEEE Signal Processing Letters*, vol. 23, no. 2, pp. 192–196, Feb 2016.
- [23] G. Wang, C. Gao, S. G. Razul, and C. M. S. See, “A new direct position determination algorithm using multiple arrays,” in *2018 IEEE 23rd International Conference on Digital Signal Processing (DSP)*, Nov 2018, pp. 1–5.
- [24] S. Boyd, N. Parikh, E. Chu, B. Peleato, and J. Eckstein, “Distributed optimization and statistical learning via the alternating direction method of multipliers,” *Foundations and Trends in Machine Learning*, vol. 3, pp. 1–122, 01 2011.
- [25] Q. Wang, Z. Zhao, and Z. Chen, “Fast compressive sensing doa estimation via admm solver,” in *2017 IEEE International Conference on Information and Automation (ICIA)*, July 2017, pp. 53–57.
- [26] M. V. Afonso, J. M. Bioucas-Dias, and M. A. T. Figueiredo, “Fast image recovery using variable splitting and constrained optimization,” *IEEE Transactions on Image Processing*, vol. 19, no. 9, pp. 2345–2356, Sep. 2010.
- [27] M. A. T. Figueiredo, J. M. Bioucas-Dias, and M. V. Afonso, “Fast frame-based image deconvolution using variable splitting and constrained optimization,” in *2009 IEEE/SP 15th Workshop on Statistical Signal Processing*, Aug 2009, pp. 109–112.
- [28] M. V. Afonso, J. M. Bioucas-Dias, and M. A. T. Figueiredo, “An augmented lagrangian approach to the constrained optimization formulation of imaging inverse problems,” *IEEE Transactions on Image Processing*, vol. 20, no. 3, pp. 681–695, March 2011.
- [29] W. Zhi and M. Y. Chia, “Near-field source localization via symmetric subarrays,” *IEEE Signal Processing Letters*, vol. 14, no. 6, pp. 409–412, June 2007.
- [30] H. He, Y. Wang, and J. Saillard, “Near-field source localization by using focusing technique,” *EURASIP Journal on Advances in Signal Processing*, vol. 2008, no. 1, p. 461517, Nov 2008. [Online]. Available: <https://doi.org/10.1155/2008/461517>
- [31] M. Chen, X. Mao, and L. Xin, “Underdetermined passive localization of emitters based on multi-dimensional spectrum estimation techniques,” *IET Radar, Sonar & Navigation*, vol. 11, 07 2017.
- [32] Y. Gürçan and A. Yarovoy, “Super-resolution algorithm for joint range-azimuth-doppler estimation in automotive radars,” in *2017 European Radar Conference (EU-RAD)*, Oct 2017, pp. 73–76.

- [33] G. O. Manokhin, Z. T. Erdyneev, A. A. Geltser, and E. A. Monastyrrev, “Music-based algorithm for range-azimuth fmcw radar data processing without estimating number of targets,” in *2015 IEEE 15th Mediterranean Microwave Symposium (MMS)*, Nov 2015, pp. 1–4.
- [34] X. Zhang, L. Xu, L. Xu, and D. Xu, “Direction of departure (dod) and direction of arrival (doa) estimation in mimo radar with reduced-dimension music,” *IEEE Communications Letters*, vol. 14, no. 12, pp. 1161–1163, December 2010.
- [35] D. Malioutov, M. Cetin, and A. S. Willsky, “A sparse signal reconstruction perspective for source localization with sensor arrays,” *IEEE Transactions on Signal Processing*, vol. 53, no. 8, pp. 3010–3022, Aug 2005.
- [36] S. Chen, D. Donoho, and M. Saunders, “Atomic decomposition by basis pursuit,” *SIAM Journal on Scientific Computing*, vol. 20, no. 1, pp. 33–61, 1998. [Online]. Available: <https://doi.org/10.1137/S1064827596304010>
- [37] D. L. Donoho, “Compressed sensing,” *IEEE Transactions on Information Theory*, vol. 52, no. 4, pp. 1289–1306, April 2006.
- [38] D. M. Malioutov, M. Cetin, and A. S. Willsky, “Optimal sparse representations in general overcomplete bases,” in *2004 IEEE International Conference on Acoustics, Speech, and Signal Processing*, vol. 2, May 2004, pp. ii–793.
- [39] D. L. Donoho, M. Elad, and V. N. Temlyakov, “Stable recovery of sparse overcomplete representations in the presence of noise,” *IEEE Transactions on Information Theory*, vol. 52, no. 1, pp. 6–18, Jan 2006.
- [40] H. E. Güven, A. Güngör, and M. Çetin, “An augmented lagrangian method for complex-valued compressed sar imaging,” *IEEE Transactions on Computational Imaging*, vol. 2, no. 3, pp. 235–250, Sep. 2016.
- [41] J. Nocedal and S. Wright, *Numerical Optimization*, ser. Springer Series in Operations Research and Financial Engineering. Springer New York, 2006. [Online]. Available: <https://books.google.nl/books?id=VbHYoSyelFcC>
- [42] J. Kim, J. Chun, and S. Song, “Joint Range and Angle Estimation for FMCW MIMO Radar and Its Application,” *arXiv e-prints*, Nov. 2018.
- [43] S. M. Kay, *Fundamentals of Statistical Signal Processing: Estimation Theory*. Upper Saddle River, NJ, USA: Prentice-Hall, Inc., 1993.

- 
- [44] K. Greenewald and A. O. Hero, “Robust kronecker product pca for spatio-temporal covariance estimation,” *IEEE Transactions on Signal Processing*, vol. 63, no. 23, pp. 6368–6378, Dec 2015.
- [45] C. F. Loan, “The ubiquitous kronecker product,” *Journal of Computational and Applied Mathematics*, vol. 123, no. 1, pp. 85 – 100, 2000, numerical Analysis 2000. Vol. III: Linear Algebra. [Online]. Available: <http://www.sciencedirect.com/science/article/pii/S0377042700003939>
- [46] C. F. Van Loan and N. Pitsianis, *Approximation with Kronecker Products*. Dordrecht: Springer Netherlands, 1993, pp. 293–314. [Online]. Available: [https://doi.org/10.1007/978-94-015-8196-7\\_17](https://doi.org/10.1007/978-94-015-8196-7_17)